NATIONAL UNIVERSITY OF SINGAPORE

AN EXPERIMENTAL AND NUMERICAL STUDY ON CAVITATION BUBBLE DYNAMICS AND ITS BIOMEDICAL APPLICATIONS

by

GOH BING HUI TERENCE
B.Eng.(Hons.), NUS

A THESIS SUBMITTED FOR THE
DEGREE OF DOCTOR OF PHILOSOPHY

in the
NUS GRADUATE SCHOOL FOR INTEGRATIVE SCIENCES AND ENGINEERING

2014

Declaration of Authorship

I, GOH Bing Hui Terence, declare that this thesis titled, 'An experimental and numerical study on cavitation bubble dynamics and its biomedical applications' and the work presented in it are my own. I confirm that:

- This thesis is my original work and it has been written by me in its entirety. I have duly acknowledged all the sources of information which have been used in the thesis.
- This thesis has also not been submitted for any degree in any university previously.

Signed: 

Date: 12 February 2015

Abstract

A thorough understanding of cavitation bubble dynamics is critical to mitigate cavitation damage or develop practical applications. An important field of study is the interaction of a single cavitation bubble with neighbouring structure(s). A cavitation bubble collapse near a finite elastic beam, or a rigid wall with an attached hemispherical bubble, are experimentally investigated. A novel low-voltage spark discharge method is also developed, which is capable of generating consistent-sized cavitation bubbles. Numerical simulations using a boundary-element model based on the potential flow theory are conducted to complement these experiments, and also study the interactions between a cavitation bubble and a nearby quiescent air bubble. Lastly, a cavitation bubble interaction with a nearby elastic cell, as well as the mechanisms behind the ultrasound-targeted microbubble disruption of bacterial biofilm are studied. Results identify the interactions between a cavitation bubble and elastic surfaces (beam and sphere), of which the degree of response of these surfaces are found to be dependent to the parameters of the problem such as the dimensionless stand-off distance H'. An air bubble attached to a rigid surface is also found to be capable of negating direct damage due to the cavitation bubble collapse jet. The results also suggest prospective use of cavitation for drug delivery, cell identification, and non-invasive treatment of bacterial biofilm on medical implants by identifying the mechanisms of ultrasound-targeted microbubble disruption of bacterial biofilm.

Acknowledgements

I wish to express my gratitude towards my Main Supervisor, Prof. Khoo Boo Cheong, for his guidance and unwavering support throughout my candidature. I also wish to thank my Co-Supervisor, Dr. Evert Klaseboer, for his patient training and provision of prompt and invaluable assistance. I have learnt much from Dr. Siew Wan Ohl, who has provided me with project opportunities and advice. I also wish to thank the Chair of my Thesis Advisory Committee, Assoc. Prof. Martin Buist for his insights and advice. I appreciate the support from all laboratory members of Fluid Mechanics Lab 1, Impact Mechanics Lab, Dynamics Lab 1 & 2, Design Lab, Control & Mechatronics Lab, of the National University of Singapore; in particular Mr. Oh Yide Andre, Dr. Karri Badarinath, Mr. Yap Chin Seng, Mr. Tan Kim Wah and Mr. Low Chee Wah.

During my candidature, I have spent a year and a half attached to the University of Dundee. I wish to express my gratitude to Dr. Paul Campbell for his guidance and making this attachment possible and fruitful. Prof. Irwin McLean, Prof. Tracy Palmer, Dr. Holger Kneuper, Dr. Charles Main, Dr. Paul Prentice, Dr. Hans Rolfnes, Dr. Pamela Robertson, Dr. Sam Swift, Dr. Adam Ostrowski, Mr. Craig McDonald, Dr. Gary Callon and Mr. Adrian Walker are among many who have offered me much support and guidance. I cannot thank my colleague and friend Dr. Michael Conneely enough for spending the long hours with me both in lab and outside of it.

I wish to acknowledge the financial support and learning opportunities the NUS Graduate School for Integrative Sciences has provided me with. I would finally like to thank all my friends and family, especially my fiancée Angel Xu, for their faith in me and sharing the ups and downs of this learning journey of mine.

Contents

List of Tables

List of Figures

Abbreviations

BEM	**B**oundary **E**lement **M**ethod
CCD	**C**harge-**C**oupled **D**evice
EPS	**E**xtracellular **P**olymeric **S**ubstance
DAQ	**D**ata **A**c**Q**uisition
fps	**f**rames **p**er **s**econd
HIFU	**H**igh-**I**ntensity **F**ocused **U**ltrasound
IR	**I**nfra-**R**ed
LG	**L**aguerre-**G**aussian
MOSFET	**M**etal-**O**xide **F**ield-**E**ffect **T**ransistor
ND	**N**eutral **D**ensity
PVC	**P**oly**V**inyl **C**hloride
SAP	**S**uper **A**bsorbent **P**olymer
SLM	**S**patial **L**ight **M**odulator
UCA	**U**ltrasound **C**ontrast **A**gent
UTMD	**U**ltrasound-**T**argeted **M**icrobubble **D**isruption

Symbols

Roman Letters

A	cross-sectional area	m^2
D	initial distance between bubbles	m
D'	dimensionless initial distance between bubbles	
E	Young's modulus	Pa
$E_{R_{max}}$	potential energy at maximum bubble radius	J
E_T	spark-discharge energy in discharge circuit	J
f	theoretical resonance frequency of a bubble	Hz (s^{-1})
F_s	surface tension	$N.m^{-1}$
g	gravitational acceleration	$m.s^{-2}$
G	shear modulus	Pa
H	initial stand-off distance	m
H'	dimensionless initial stand-off distance	
l	length of wire	m
L	initial length of fine electrode wire	m
L_c	length scale	m
N	number of nodes	
p	pressure	Pa
p_a	total pressure in air bubble	Pa
p_b	total pressure in cavitation bubble	Pa
p_g	gas pressure in bubble	Pa
p_v	vapour pressure	Pa
p_∞	reference pressure	Pa
P^-	peak-negative-pressure	Pa

R	bubble radius	m
R_a	initial air bubble radius	m
$R_a{}'$	bubble size ratio	
R_e	equilibrium air bubble radius	m
R_s	initial radius of elastic sphere	m
$R_s{}'$	normalized initial radius of elastic sphere	m
R_{max}	maximum bubble radius	m
$\dot{R_{max}}$	mean maximum bubble radius	m
t	time	s
t_c	time scale	s
t^*	dimensionless time	
T	oscillation time of cavitation bubble	s
T'	dimensionless oscillation time of cavitation bubble	
T_a	theoretical period of oscillation of a bubble	s
u	velocity	$\mathrm{m.s^{-1}}$
u_j	liquid jet velocity	$\mathrm{m.s^{-1}}$
U_∞	reference velocity	$\mathrm{m.s^{-1}}$
v	velocity	$\mathrm{m.s^{-1}}$
v_n	normal velocity	$\mathrm{m.s^{-1}}$
V	volume of bubble	$\mathrm{m^3}$
$V(t)$	time-dependent capacitor voltage	V
z	vertical deflection of rubber beam	m
Z	resistance	Ω
Z_a	additional resistance	Ω
Z_A	increased discharge circuit resistance	Ω
Z_w	initial resistance of an electrode	Ω
$Z_{w,l}$	initial resistance of an electrode with fine wire length l	Ω
$Z_T(t)$	time-dependent discharge circuit resistance	Ω

Greek Letters

γ	ratio of specific heats of fluid	
γ_1	ratio of specific heats of air	
γ_2	adiabatic index for cavitation bubble	
μ	dynamic viscosity	kg.(m.s)^{-1}
ω	resistivity	Ω.m
ϕ	velocity potential	
ρ	density	kg.m^{-3}
σ	standard deviation	%

Subscripts

on any variable, Q:

Q_0	initial value
Q_1	cavitation bubble value
Q_2	air bubble value
Q_b	value within cavitation bubble
Q_c	scale parameter
Q_{down}	downward deflection
Q_{max}	maximum value
Q_R	value at surface of bubble
Q_{up}	upward deflection

Superscripts

on any variable, Q:

Q^*	dimensionless parameter
$\dot{Q}$	mean value
$\vec{Q}$	vector quantity
Q'	dimensionless parameter

Chapter 1

Introduction

1.1 Short background on cavitation bubble dynamics

Cavitation refers to the process in which a liquid is ruptured into vapour cavities due to a rapid decrease in liquid pressure, below that of the saturated vapour pressure. For any real-life application, cavitation typically initiates from weakness sites in a liquid, which are called nucleation sites. These nucleation sites can come in the form of microscopic voids present in a liquid, crevices at fluid boundaries, or even micro-meter sized bubbles (microbubbles) (Harvey et al., 1944). Cavitation bubbles will then develop or grow from these nucleation sites.

To understand the dynamics of cavitation bubbles, lets first consider a single spherical bubble in a theoretically infinite liquid medium. Figure 1.1 shows a schematic of a spherical bubble of radius R, in a liquid medium with ambient pressure p_∞, which is assumed to be a known parameter or input that accounts for the growth and collapse of the bubble. The pressure within the bubble is represented as p_b. p and u refers to the pressure and radial outward velocity at any arbitrary point in the liquid, denoted by the

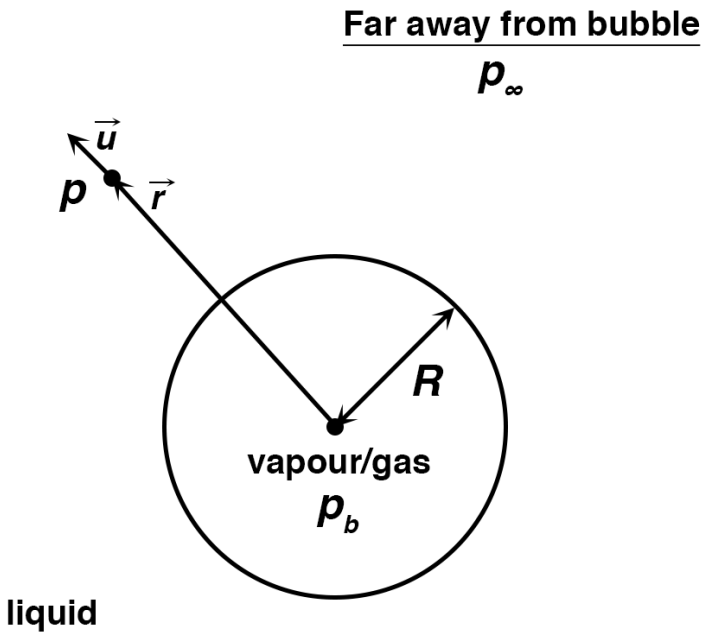

FIGURE 1.1: Schematic of a spherical gas bubble in an infinite liquid.

position vector $\vec{r}$. For simplicity, several assumptions are made. Firstly, the ambient temperature is assumed as a constant and temperature effects are not considered. Secondly, the contents within the bubble are assumed to be homogeneous and parameters such as p_b are uniform. Thirdly, the liquid is assumed to be incompressible, hence giving constant and uniform liquid density ρ and dynamic viscosity μ.

For a Newtonian fluid, the Navier-Stokes equation in the r-direction is given as:

$$-\frac{1}{\rho}\frac{\delta p}{\delta r} = \frac{\delta u}{\delta t} + u\frac{\delta u}{\delta r} - \frac{\mu}{\rho}[\frac{1}{r^2}\frac{\delta}{\delta r}(r^2\frac{\delta u}{\delta r}) - \frac{2u}{r^2}]. \tag{1.1}$$

From the conservation of mass and in the case of zero mass transport across the bubble boundary, we get the following expression:

$$u = \frac{F}{r^2} = \frac{R^2}{r^2}\frac{dR}{dt}, \tag{1.2}$$

assuming that the density of liquid is much greater than the density of the gas, and F is some function of time t.

Similarly, assuming no mass transfer across the bubble boundary, we have the following expression for the pressure at the bubble surface ($r = R$):

$$p_R = p_b - \frac{4\mu}{R}\frac{dR}{dt} - \frac{2F_s}{R}, \tag{1.3}$$

where F_s is the surface tension.

Substituting Equations 1.2 & 1.3 into an integral of Equation 1.1 from $r = R$ to $r = \infty$, and applying appropriate boundary and dynamic conditions, we obtain:

$$\frac{p_R - p_\infty}{\rho} = R\frac{d^2R}{dt^2} + \frac{3}{2}(\frac{dR}{dt})^2 + \frac{4\mu}{\rho R}\frac{dR}{dt} + \frac{2F_s}{\rho R}. \tag{1.4}$$

This ordinary differential equation is known as the Rayleigh-Plesset equation. Rayleigh (1917) first derived the equation neglecting surface tension and viscosity in 1917 and Plesset (1949) first demonstrated applicability of this equation to cavitation bubbles in 1949 by considering the influence of fluid viscosity and surface tension effects. It governs the dynamics of a spherical bubble in an infinite fluid.

Consider a case in which it is inertial driven (ignore viscous and thermal effects), and assuming the pressure within the bubble to be uniform and adiabatic, such that $p_b = p_{b,0}(\frac{R_0}{R})^{3\gamma}$, where γ is the ratio of specific heats of the gas. A typical behaviour of a bubble encountering a region with a single low pressure pulse is presented in Figure 1.2. The bubble has an initial radius R_0 and is introduced with a decrease in ambient liquid pressure P_∞ up to a minimum of -1.2 times of initial ambient liquid pressure $P_{\infty,0}$ at dimensionless time $t^* = 250$. P_∞ then reverts back to $P_{\infty,0}$ at $t^* = 500$. Figure 1.2 shows

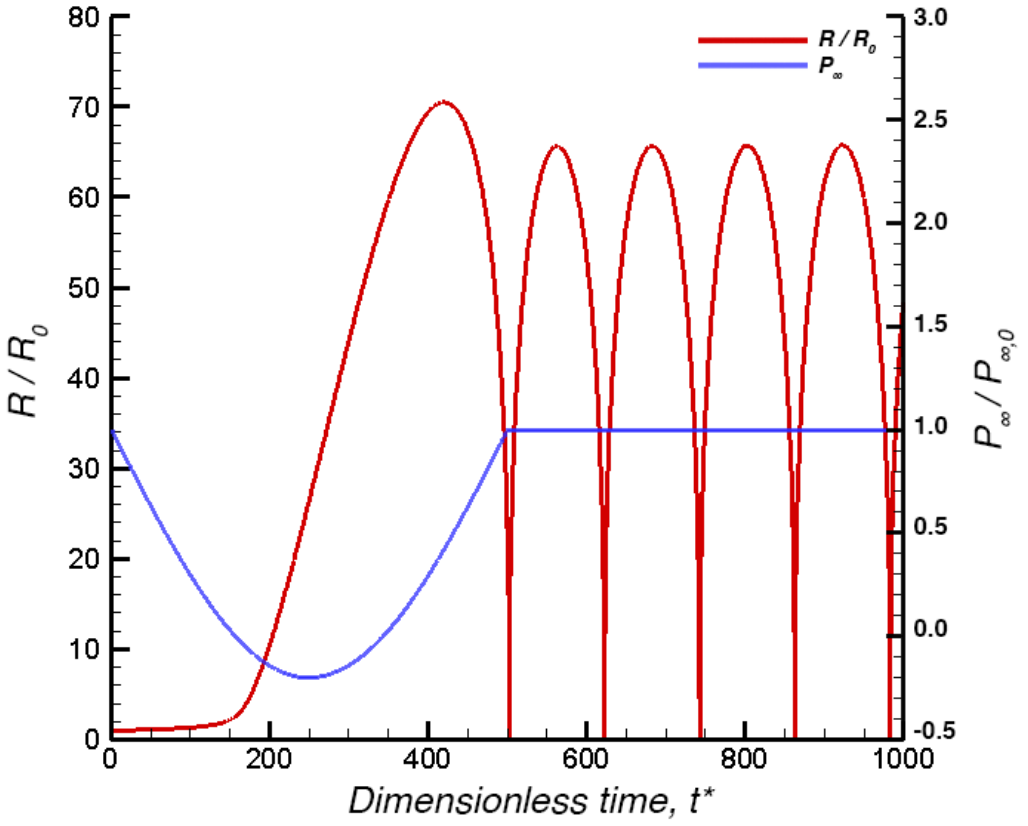

FIGURE 1.2: Rayleigh-Plesset solution of a spherical bubble entering a region with a low pressure pulse. The graph shows the bubble radius ratio R/R_0 vs. dimensionless time t, superimposed with a ambient liquid pressure ratio $P_\infty/P_{\infty,0}$ against t^*.

a graph of its radius ratio R/R_0 against t^* and the pressure ratio $P_\infty/P_{\infty,0}$ against t^* also superimposed. The bubble grows steadily to a maximum R of around 70 R_0 after passing the minimum pressure region. After the bubble attains its first maximum volume, it is predicted to collapse catastrophically at $t^* = 500$, following by successive rebounds and collapses. The oscillation cycles after the first will continue without attenuation as we did not consider dissipation mechanisms in this example.

A typical theoretical formulation of a spherical cavitation bubble growth and collapse in a infinite liquid have been shown. However, a cavitation bubble created near to a surface is a particular important subject due to the tendency for material damages resulting from high velocities, pressures and temperatures from the bubble collapse (Brennen,

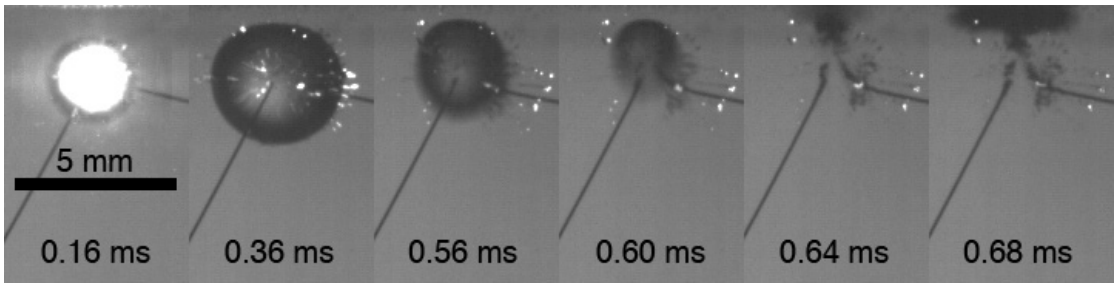

FIGURE 1.3: Growth and collapse of a spark-discharge cavitation bubble near to a rigid plate above the bubble (top border). The spark discharge between two crossing electrodes submerged underwater creates an oscillating cavitation bubble that first expands asymmetrically and reaches a maximum radius of $R = 2.07$ mm at $t = 0.36$ ms. It then collapses with a liquid that impinges onto the rigid plate. A 5mm scale bar is shown in the first frame, and respective timings at the bottom of each frame.

1995). Figure 1.3 shows the case of a spark-discharge cavitation bubble near to a rigid boundary. The first frame shows an expanding non-equilibrium bubble created by a low-voltage spark discharge method. With a rigid surface in proximity (upper border of image frames), the bubble expansion is no longer spherical. This can be seen at $t = 0.36$ ms, where the bubble reaches its maximum radius of 2.07 mm, with a compressed upper portion that is closer to the rigid plate above. The bubble surface away from the wall has less deviation from the spherical shape, and as a result, accelerates inwards more rapidly that the opposite surface. This causes the development of a high-speed microjet that penetrates the bubble upon collapse, as seen from $t = 0.60$ ms to 0.68 ms. This presence of a collapsing liquid jet was first suggested by Kornfeld and Suvorov (1944), but verified experimentally by Naude and Ellis (1961) and Benjamin and Ellis (1966).

This collapsing cavitation bubble liquid jet near to a rigid surface is of special interest to the studies of cavitation damage. The most prominent example of cavitation would be on the destruction of propeller blades of fast moving boats. It was first noticed on the screw propeller blades of steam boats in the early 20th century, which was in some cases so detrimental that it would render the propeller unfit for work after only several hours of operation. Parsons (1906) was one of the first to account for cavitation

activity on ship propellers at high rotational speeds. Due to the rapid fluid velocity around rotating propeller blades, low fluid pressure arise due to the Bernoulli principle, and that causes the formation of non-equilibrium or cavitation bubbles. As the bubbles are created very near to the rigid surface of the propeller blades, they expand and collapse asymmetrically. This creates a tendency for the cavitation bubble to collapse rapidly with a liquid jet towards the rigid blade surface as previously discussed. This liquid jet is capable of reaching very high velocities which develops into the formation of pits, and erodes away the propeller blade material. It is now generally accepted that cavitation damage of material is caused by localized stresses and disturbances due to these impinging liquid jets onto the bubble surface, as well as shockwaves emitted from the cavitation bubble collapse.

Cavitation bubbles are also found in nature. Snapping shrimps baffled marine biologists with their ability to crack tough shells of crustaceans using rapid strikes of their arms onto their prey. It was only verified using high-speed imaging and hydrophone measurements that the strikes on the shells of the preys of the snapping shrimps has velocities so high that it creates localized cavitation bubbles (Versluis et al., 2000). These bubbles collapse rapidly, reaching very high temperatures and the repeated collapsing liquid jets and high pressure waves create enough stress to crack the shell surface. Cavitation bubbles are notorious for its damaging properties, but at the same time they can be utilized for a myriad of applications. In the biomedical field, lithotripsy is a common procedure used to non-invasively break up kidney stones so they can be passed out from the human body. The primary mechanisms behind lithotripsy is to generate cavitation bubbles near the kidney stones using shock wave or laser pulses, that in turn fragments kidney stones into smaller pieces. When properly harnessed, the understanding of many physical phenomena can develop into many applications that are beneficial to mankind.

1.2 Brief literature review

Studies in cavitation bubble dynamics can involve many methods, disciplines, and can be applied in an extensive range of areas and industries. The focus of this thesis is on the experimental and numerical investigations of cavitation bubble dynamics and its applications to the biomedical industry. A brief review of notable works in the literature on cavitation bubble dynamics will first be presented, separated into the following three main categories: experimental investigations (Section 1.2.1), numerical simulations (Section 1.2.2), and biomedical applications (Section 1.2.3).

1.2.1 Experimental investigation on cavitation bubble dynamics

As mentioned earlier, the study of cavitation bubble dynamics was first motivated by damages on fast-moving ship propeller blades. The first few pioneering experimental studies on cavitation bubble damage were conducted in the 1960s by Naude and Ellis (1961) and Benjamin and Ellis (1966), primarily involving high-speed image sequences to capture the growth and collapse of spark-discharge cavitation bubbles generated very near to a rigid surface. This phenomenon of a single cavitation bubble collapse near a rigid surface was studied in greater detail since then. The studies involve different experimental setups to generate the cavitation bubble(s), which comprise of pulsed-laser (Lauterborn and Bolle, 1975; Vogel et al., 1988; Ohl et al., 1995, 1998; Chen, 2004; Aglyamov et al., 2008; Dijkink and Ohl, 2008; Yang et al., 2013), electrical spark-discharge (Burtsev and Shamko, 1977; Shima and Tomita, 1981; Tomita and Shima, 1986; Soh, 1990; Guo et al., 2013), and piezo-electric methods (Ohl et al., 1999; Zhong et al., 1999; Xi and Zhong, 2000; Wolfrum et al., 2003; Tzanakis et al., 2014). As the time frame for cavitation bubble oscillations is typically very small, a high-speed

imaging setup is almost necessary for the visual studies of cavitation bubble dynamics in these cases. The results from these studies are consistent, in that there is a tendency for the cavitation bubble to collapse with an impinging liquid jet towards the rigid surface. The formation of these jets is believed to contribute to material damage and the dimensionless stand-off distance H' is found to be an important parameter that influences the magnitude of this damage. H' is defined as the ratio of the initial distance between the centre of the cavitation bubble and the rigid wall (or stand-off distance) H and the maximum cavitation bubble radius R_{max}. The bubble dynamics is noticed to differ for experiments at different H' (Ohl et al., 1995; Yang et al., 2013). Guo et al. (2013) studied the effect of a spark generated cavitation bubble near a barnacle and reported higher jet velocities and greater impact pressures for cases conducted with relatively smaller H'. This observation coincides with theoretical predictions, which are discussed in the next Section 1.2.2.

An asymmetrical cavitation bubble collapse does not always create a liquid jet directed towards a neighbouring surface. For instance, when a cavitation bubble is created near to a free surface, there is now a tendency for the bubble to collapse with a liquid jet directed away from the free surface. This observation cavitation bubble collapse near a free surface has been studied in detail by Cole (1948), Holt (1977), Blake and Gibson (1981), Tomita et al. (1991), and Robinson et al. (2001). The dynamics of the bubble and the free surface are captured by high-speed cameras in these experiments. The expanding bubble under a free surface tends to induce a free surface spike or jet upwards, while forming a liquid jet penetrating the bubble in the opposite direction.

Apart from a rigid boundary and a free surface, there are also many reports of cavitation bubble(s) near to surfaces of different material properties. One type of surface that is of particular interest to researchers is an elastic boundary. Gibson and Blake (1982)

and Blake and Gibson (1987) conducted some of the earliest work on cavitation bubble growth and collapse near an elastic boundary. High-speed photography was used to capture the response of the bubble near to a rubber coated surface and they reported cases of bubble collapse with a jet away from the surface, or even cases in which the bubble splits into two. This interesting interaction pattern is also seen in experiments conducted by Shima et al. (1989), Shaw et al. (1999), and Tomita and Kodama (2003). Brujan et al. (2001a,b), and Turangan et al. (2006) presented results on a cavitation bubble created near an elastic membrane and reported that dynamics of the bubble are strongly dependent on the elasticity of the boundary and the dimensionless stand-off distance H'.

In practical applications, cavitation bubbles do not tend to exist in isolation. As a result, the interaction of a cavitation with neighbouring bubbles becomes of interest to researchers. Experimental observations of two cavitation bubbles near to each other were first conducted by Timm and Hammit (1971), Lauterborn (1982), and Lauterborn and Hentschel (1985). They observe that the size difference in the bubbles cause different jet directions and bubble behaviour. Subsequently, Tomita et al. (1990) noticed that the bubble-bubble interaction is influenced not only by the relative sizes of bubbles but also by the initial distance between them. Garbin et al. (2007) utilized holographic optical traps to study the forces between two oscillating microbubbles near to each other. Fong et al. (2009) and Chew et al. (2011) then studied the interaction of two similar or differently sized cavitation bubbles, with phase differences and noticed that the response of the bubbles are largely dependent on their oscillatory phase difference. It was discovered that bubbles that expand and collapse in-phase tend to collapse with liquid jets toward each other, while out-of-phase bubbles tend to jet away from each other. As the relative oscillation times of the bubbles essentially contribute to phase similarity

or difference, this observation is synchronous with previous observations. There are also many detailed studies on multiple bubble systems in proximity to neighbouring surface(s) (Tomita et al., 1990; Blake et al., 1993; Kodama and Tomita, 2000; Bremond et al., 2006b,a; Ohl, 2010; Xu et al., 2010; Yuan et al., 2011; Aghdam et al., 2012). It is found that there are competing influences between a cavitation bubble and the additional surfaces (including bubbles) that it is near to. Hence by understanding the responses of a cavitation bubble to a neighbouring surface, it possible to design a system in which a desired bubble response can be arranged by careful selection and placement of boundaries and materials. This could be beneficial in negating cavitation damage or utilize the effects of cavitation for different applications.

1.2.2 Numerical simulations of cavitation bubble dynamics

Apart from experimental observations, the current understanding of cavitation bubble dynamics is also largely contributed by theoretical analysis and numerical studies. Plesset (1949) first applied the Rayleigh-Plesset equation (see Section 1.1) for the study of cavitation bubbles, and since then many numerical works have emerged. One of the earlier numerical studies of a cavitation bubble collapse near a rigid boundary is also conducted by Plesset and Chapman (1971). They are able to predict the bubble shape during collapse and the resulting jet velocities of around 100 $\mathrm{m.s^{-1}}$, which led them to determine a relationship between the liquid jet impact and cavitation damage. The theoretical shapes of the cavitation bubble collapse are verified experimentally by Lauterborn and Bolle (1975) with very good agreement. Prosperetti (1982), Cerone and Blake (1984), Blake et al. (1986), Zhang et al. (1993), and Klaseboer et al. (2005a) performed some other notable numerical studies of a cavitation bubble collapse near a rigid boundary. These works reinforces the understanding of this phenomenon, shedding

more insights into the pressures generated on the rigid surface and bubble dynamics and jet velocities involved.

Earlier numerical works on cavitation bubble collapse near a free surface include those by Holt (1977), Chahine (1977), and Blake and Gibson (1981). These works have been succeeded by a series of papers by Cerone and Blake (1984), Blake and Gibson (1987), Wang et al. (1996a), Tong (1997), Robinson et al. (2001), Wang et al. (2003), Pearson (2004), and Klaseboer et al. (2005b) etc., in which the bubble dynamics or in some cases the formation of toroidal bubbles were explored in greater detail. In addition to numerical simulations of cavitation bubbles near to a rigid boundary or a free surface, there is also interest in the numerical simulations of cavitation near elastic surfaces. This include works of Duncan and Zhang (1991), Duncan et al. (1996), Klaseboer and Khoo (2004a), Klaseboer and Khoo (2004b), and Turangan et al. (2006). The elastic surface or interface has been modelled as a spring-backed membrane (Duncan and Zhang, 1991), finite-element model of an elastic surface (Duncan et al., 1996), or as a fluid-fluid interface (Klaseboer and Khoo, 2004a,b; Turangan et al., 2006). Most of these works also include comparisons with physical experiments for validation.

There are a number of notable numerical works on multiple cavitation bubble interactions in the literature. For the case of interaction between two cavitation bubbles, Pelekasis and Tsamopoulos (1993a,b) provided a quantitative and detailed study of the forces between two oscillating bubbles in close proximity to one another. Rungsiyaphornrat et al. (2003) modelled the coalescence of two cavitation bubbles underwater. Kurihara et al. (2011) modelled two shape oscillating bubbles in a viscous fluid, showing the prediction of liquid jets and also suggesting that bubble-bubble interactions act to enhance surface mode instability. Fong et al. (2009) and Chew et al. (2011) provided numerical

simulations in addition of their experiments on two similar or differently sized cavitation bubbles, focusing on phase differences. Finally, Blake et al. (1993), Bremond et al. (2006b), and Bremond et al. (2006a) also performed numerical simulations in support of their experiments of multiple cavitation bubbles near to other boundaries.

1.2.3 Cavitation bubble dynamics in biomedical applications

Cavitation bubbles play an important role in many biomedical applications. A prolific example would be shock wave lithotripsy. It is a procedure that uses shock waves to break up kidney stones, and was first introduced by Chaussy et al. (1980). It has evolved to become the most common treatment for kidney stones presently (Chaussy and Fuchs, 1989; Pearle et al., 2005). During treatment, focused shock waves are applied to renal stones until the stones are fragmented small enough to be passed out of the patient's body. Cavitation is believed to play an integral role in the destruction of renal stones (Coleman et al., 1987; Crum, 1988; Pishchalnikov et al., 2003). As previously discussed, when a cavitation bubble is created near to the renal stones, there is a tendency for the bubble to collapse with a high speed jet towards the rigid surface. After multiple pulses of shock waves, high stress generated on the renal stones becomes sufficient to cause them to disintegrate.

There has been an emergence of development of techniques or treatments using cavitation for biomedical applications in recent years. Ultrasound contrast agent (UCA) microbubbles are used in many of these imaging techniques and therapeutic applications(Stride and Saffari, 2003a; Qin et al., 2009). These bubbles are typically administered in the blood stream as they provide superior backscattering of the ultrasound waves during ultrasound imaging. These bubbles expand and contract in response to the ultrasound

waves, and depending on the applied ultrasound frequency and amplitude, these bubbles could undergo stable (small amplitude) or inertial (transient collapse) cavitation (Chomas et al., 2001; Stride and Saffari, 2003b). Apart from medical imaging, these microbubbles are excellent candidates for therapeutic procedures among which targeted drug delivery is an exceptionally promising area (Sivakumar et al., 2014; Razavi et al., 2014). Microbubbles act as nuclei for cavitation in which concentrated pressure waves are deployed to permeabilize cell-membranes and disrupt drug-carrying vesicles (Pitt et al., 2004; Husseini et al., 2005). These bubbles can be coated with ligands for them to bind to specific cell types, as reported in recent review articles by Alzaraa et al. (2012) and Unger et al. (2014).

Another promising area of application is the use of cavitation UCA microbubbles to treat bacterial biofilm infections. Bacteria biofilm refers to an aggregate of bacteria cells adhering to each other on a surface. The biofilm structure protects the cells against anti-microbial killing and host responses. This makes bacterial biofilm infections difficult to diagnose and eradicate, especially on medical implants such as prosthetic joints (Trampuz et al., 2003; Trampuz and Zimmerli, 2005). Current treatment methods of prosthetic joint infections often involve multiple operations with increased recurrence rates and complications, and greater costs (Hebert et al., 1996; Matthews et al., 2009). Several reports have shown prospects that using ultrasound or microbubbles with ultrasound enhances efficacy of anti-microbial drugs against biofilm infections or physically disrupt bacterial biofilms (Pitt et al., 1994; Bigelow et al., 2009; He et al., 2011; Xu et al., 2012; Yu et al., 2012; Dong et al., 2013). Among them, He et al. (2011) and Dong et al. (2013) used ultrasound-targeted microbubble destruction and reported increased effect of antimicrobial agents against *Staphylococcus epidermidis* biofilms (which are commonly associated with medical device infections). It is likely that cavitation plays

an important role in this phenomenon, and could contribute to increased permeability of cellular membranes like that in the methods for drug delivery. However the exact mechanisms of this prospective treatment option is not yet understood. Treating Chronic Rhinosinuitis (which may be caused by bacterial biofilm around nasal passages) (Bartley and Young, 2009; Hall-Stoodley and Stoodley, 2009) and oral biofilms (Parini and Pitt, 2006; Nishikawa et al., 2010) with cavitation technologies are other promising areas of biofilm infections as the difficulty in treatment resides in bypassing biofilm structural integrity.

1.3 Scope and objectives of thesis

Currently, there exist many problems that would benefit from a thorough understanding of cavitation bubble dynamics. These problems range from age old issues such as cavitation pitting onto rigid surfaces, to collateral damage on biological tissues in the human body. Biomedicine is one emerging field in which the knowledge of cavitation bubbles near to structures can contribute to the development of many non-invasive treatment options for diseases and infections. Therefore, the objective of this thesis is to provide an understanding of the dynamics of cavitation bubbles in proximity to different surfaces, and also evaluate the prospects of using cavitation to solve current problems such as cavitation damage onto rigid surfaces and persistent bacterial biofilm infections in medical devices.

This is achieved through a series of systematic studies conducted using experimental (Chapter 2) and numerical techniques (Chapter 3), to study the phenomenon of a single cavitation bubble interaction with neighbouring surface(s). Section 2.1 first investigates

the interaction of a cavitation bubble collapse near a finite elastic beam. Different interaction patterns between the bubble and the elastic beam are seen at different dimensionless stand-off distances H'. The cavitation bubble dynamics and jetting characteristics are then investigated when it is created near a solid wall with an attached air bubble in Section 2.2. This study was conducted with motivations to negate solid surface damage by lining the surface with air bubble(s). The above experimental studies are conducted using a low-voltage spark discharge method. Section 2.3 elaborates on a novel modification to the current low-voltage spark-discharge setup, in order to generate consistent sized cavitation bubbles.

For numerical simulations of cavitation bubble interactions in Chapter 3, an introduction to the basics of the numerical model used in the present thesis is first stated. Section 3.1 presents some background on the axi-symmetrical boundary element model used for cavitation bubble dynamics studies. Section 3.2 studies the interaction of a quiescent air bubble next to an oscillating bubble. A liquid jet can be predicted on the air bubble and its dependency on the key parameters of this study will also be discussed. Section 3.3 is an extension of Section 2.2, in which numerical simulations are conducted to enhance the understanding of the physics and interaction between a cavitation bubble and a wall-attached quiescent hemi-spherical air bubble.

Finally, two studies that focus on prospective biomedical applications of cavitation bubbles are presented in Chapter 4. Section 4.1 studies the effect of a cavitation bubble near to an elastic sphere of varying elasticity. This study has relevance to the interaction of a cavitation bubble with a cell in suspension and could inspire areas in drug delivery or cellular diagnosis. Section 4.2 investigates ultrasound-targeted microbubble disruption of bacterial biofilms of which the exact mechanisms of this phenomenon was not fully understood. With the use of high-speed imaging and holographic optical trapping

techniques, the dynamics of a single cavitation bubble beside a bacterial biofilm can be studied. The understanding of the physical mechanisms behind the biofilm eradication process allows the identification of key parameters towards the development and enhancement of treatment methods for biofilm on medical implants. The concluding Chapter 5 then summarizes the reported studies and explores opportunities for future work.

Chapter 2

Experimental Investigation of Cavitation Bubble Dynamics

In this chapter, three projects involving the experimental investigation of cavitation bubble dynamics and phenomena will be presented. It is disclosed in Section 1 that the mitigation of surface damage from cavitation is one of the main motivations towards the study of cavitation bubble dynamics. Further, it is also discussed that elastic surfaces may alter the dynamics of a neighbouring cavitation bubble. The experimental study in Section 2.1 deals with the problem of a cavitation bubble near a finite elastic beam and the bubble's influence on the beam at different stand-off distances is investigated. Bubbles do not typically exist by themselves and it was hypothesized that attaching an air bubble onto a surface may have damage mitigation effects from a neighbouring cavitation bubble. Section 2.2 was conducted to study the dynamics of a cavitation bubble near to a rigid wall with an attached hemispherical air bubble. These two projects involve the use of a low-voltage spark-discharge method to create the cavitation bubble. However, as with other spark-discharge (low- or high-voltage), it was difficult to create

consistently sized cavitation bubbles. The last Section 2.3 describes a novel low-voltage spark-discharge method that is able to repeatedly obtain consistent maximum cavitation bubble radius to aid in experimental investigations of cavitation bubble dynamics by enhancing repeatability and minimizes experimental disturbances. It was used in another study, which will be presented in Section 4.2. Parts of the results in these sections 2.1, 2.2, & 2.3 were published in Gong et al. (2012), Goh et al. (2014b), and Goh et al. (2013) respectively.

2.1 Interaction of a spark-generated bubble with a rubber beam

The behaviour of an oscillating bubble is known to be greatly dependent on the characteristics of a boundary that it is near to. For instance, if the neighbouring boundary is rigid, the bubble has a tendency to move towards it; conversely, if it is a free surface, the bubble tends to migrate away from it. The behaviour of an oscillating bubble near to a flexible surface is in-between the two limiting cases mentioned above and is more complex in nature. This interaction between an oscillating bubble and a flexible boundary is important as it is commonly found in nature, marine industrial applications, and medical treatments (Lauterborn and Kurz, 2010). Some of the earliest theoretical and experimental studies on the interaction between an oscillating bubble and an elastic boundary were conducted by Gibson and Blake (1982) and Blake and Gibson (1987). They found that the response of a cavitation bubble is greatly dependent on the flexibility of the neighbouring boundary and it would split into smaller bubbles before collapsing with jets when near an elastic surface. Shima et al. (1989) experimentally

observed varying migratory behaviours during an oscillating bubble collapse near a compliant surface, which has also been modelled as a membrane with a spring foundation (Duncan and Zhang, 1991) or using a finite element representation (Duncan et al., 1996). A good qualitative agreement is present between the experiment and the simulations. Other studies include laser-induced cavitation bubble(s) near a flexible membrane (Shaw et al., 1999), composite surface (Tomita and Kodama, 2003), elastic boundary (Brujan et al., 2001a,b), and a flat free surface (Blake and Gibson, 1981). Ohl et al. (2009) and Ohl et al. (2010) conducted low-voltage spark-discharge bubble experiments and simulations to study the dynamics of oscillating bubbles near to a thick layer of biomaterials of different elasticity. However, the interaction between a bubble and a finite elastic beam has not been investigated. The study of this interaction is important as it not only fills the gap of knowledge in the state of the art regarding cavitation interaction with elastic members, it also supports the development of cavitation based methods for use on elastic or visco-elastic biological materials (e.g. biofilms). In this section, the interaction of a spark-generated bubble near to an elastic beam using a high-speed imaging setup is studied. The two key parameters in this problem are the elasticity of the membrane and the initial distance between the bubble and the beam (normalized by the maximum bubble radius).

2.1.1 Experimental Setup

The experimental setup comprising of an electrical circuit for spark bubble generation, a Perspex tank of dimensions 25 cm x 25 cm x 25 cm filled with tap water to a height of 24 cm, a Perspex fixture to hold a rubber beam down at both ends, and a high-speed imaging system is shown in Figure 2.1. The electrical circuit adopts a low-voltage spark-discharge method that is similar to the ones used in several other cavitation bubble

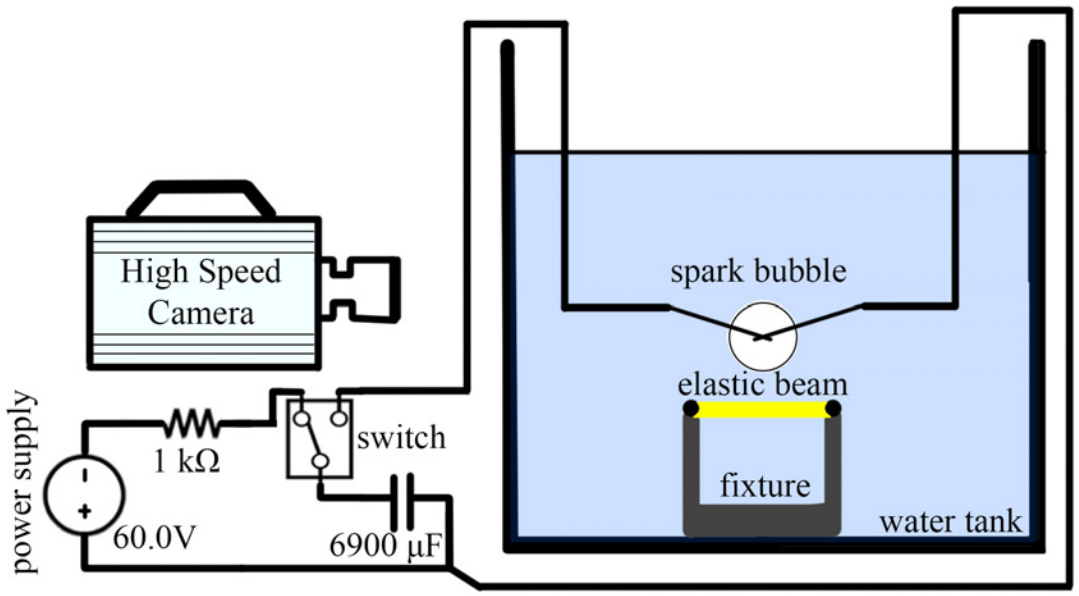

FIGURE 2.1: Experimental setup, comprising of a power supply where a 6900 μF capacitor is charged to 60.0 V through a 1kΩ resistor. The discharge circuit is connected to two submerged crossing electrodes and activated with a switch to create a spark bubble. This bubble is created above a Perspex fixture secured to the bottom of the water tank and fixing a rubber beam at its ends. The whole process is captured by a high-speed camera system.

investigations (Turangan et al., 2006; Ohl et al., 2010; Buogo and Cannelli, 2002; Lew et al., 2007; Fong et al., 2009; Pain et al., 2012). It basically consists of a charging circuit and a discharge circuit separated by a mechanical switch. The charging circuit is made up of two capacitors (a 2200 μF, 63 V capacitor and a 4700 μF, 63 V capacitor in parallel) with a total capacitance of 6900 μF, which are charged by DC power supply through a 1 kΩ resistor to 60.0 V. The discharge circuit comprises of a pair of 0.1 mm diameter copper wire electrodes submerged underwater and placed in contact with each other. When the capacitors are charged to 60.0 V, the mechanical switch is pressed to engage the discharge circuit and a spark is created at the electrodes' contact point. This spark develops into an oscillating vapour bubble of a maximum radius (taken as the horizontal radius, which is half the distance between the left-most and right-most points of the bubble in this case) of around 5 mm in a violent process that causes the thin electrodes to break. As the diameter of the electrodes used is much smaller than

the maximum bubble radius ($\approx$ 2 %), they are assumed to have a negligible effect on the dynamics of the system (Lew et al., 2007; Fong et al., 2009). The electrodes' contact point is adjusted to be at a varying height H above the centroid of a silicone rubber strip, which is used as an elastic beam. The rubber strip has a density of 1170 kg/m^3, tensile strength of 8.34 GPa (corresponding Young's modulus of elasticity $E = 2.38$ GPa), and is supported in a Perspex fixture. The fixture is made up of two 100 mm (length) x 10 mm x 10 mm (square cross-section) beams erected 50 mm apart and fixed down to the base of the Perspex (see Fig. 1). Both ends of the elastic beam are placed flat on top of the fixture and then secured using a countersunk stainless steel screw and washer on each side. The portion of the rubber beam between the two supports has a dimension of Length 50 mm x Width 10 mm x Thickness 1.5 mm. The top surface of the rubber beam is 120 mm above the floor of the tank initially, and H goes up to 20 mm for this study.

A Photron Fastcam-APX RS high-speed camera is used at 20 kfps, a shutter speed of 1/40,000 s, 512 x 256 pixels at a resolution of around 9 pixels/mm to capture the dynamics of the generated oscillating bubble and the corresponding response of the beam. All the experiments are conducted under atmospheric pressure and at room temperature (24 °C). Viscosity and surface tension effects are assumed negligible in this study due to the relative large size of the bubbles (unlike microbubbles (Versluis et al., 2010)), and the Weber number (which represents the ratio of inertia forces to surface tension forces) for a millimetre-sized oscillating bubble in water is in the order of 10^3 (Rungsiyaphornrat et al., 2003; Zhang and Zhang, 2005) respectively. This is discussed in more detail in Chapter 3.1.1.

2.1.2 Results

As mentioned in the introduction, the elasticity of the membrane and the dimensionless stand-off distance of the bubble are the two main parameters in this study. As a rubber beam of fixed dimensions and properties is chosen, we can study the effect of the dimensionless stand-off distance, represented by $H' = H/R_{max}$ (where R_{max} is the maximum oscillating bubble radius). This problem is studied by selecting four distinct H' of 3.18, 1.38, 0.97 and 0.56, which can be referred to as large, moderate, small, or very small dimensionless stand-off distance. The maximum upwards and downwards deflection of the center of the rubber beam is measured by comparing the centroid of the beam at any given time against the initial position of the centroid of the beam; they are then defined as $z_{max,up}$ and $z_{max,down}$ respectively.

2.1.2.1 Bubble collapse at large *H'*

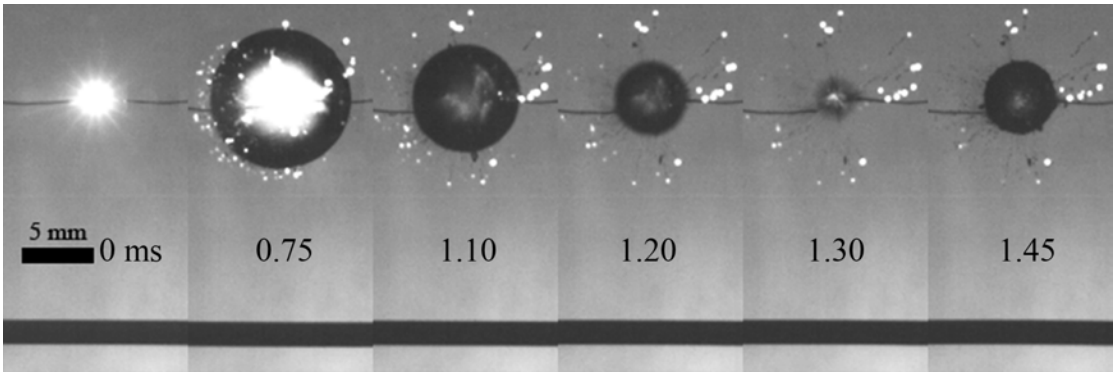

FIGURE 2.2: Oscillation of the spark bubble, which is initiated very far ($H' = 3.18$) given in the first frame. The dark horizontal strip at the bottom of the frames is the rubber beam. The times for each frame are 0.00, 0.75, 1.10, 1.20, 1.30, 1.45 ms from the first spark observed (which is taken to be time= 0.00 ms then). The bubble grows from 0.00 ms to its maximum size of $R_{max} = 4.64$ mm at 0.75 ms. It is observed that the bubble collapses spherically (frames 2 to 5) and then rebounds (frame 6). The rubber beam below hardly moves.

Figure 2.2 shows the collapse of a spark-generated bubble initiated very far away from the rubber beam ($H' = 3.18$). The timing of the frames shown are $t = 0.00$, 0.75,

1.10, 1.20, 1.30, and 1.40 ms from the first spark observed (taken to be $t = 0.00$ ms). The bubble grows from 0.0 ms to its maximum radius of $R_{max} = 4.64$ mm at $t = 0.75$ ms. At the maximum bubble radius, the center of the beam displaces downwards with a maximum measured vertical deflection of $z_{max,down} = 0.171$ mm. The bubble then collapses spherically from $t = 0.75$ ms to 1.30 ms, before re-expanding as shown at $t =$ 1.45 ms. The collapse of the bubble causes the beam center to deflect upwards by 0.171 mm and returning to its initial position, hence $z_{max,up} \approx 0.00$ mm.

2.1.2.2 Bubble collapse at moderate *H'*

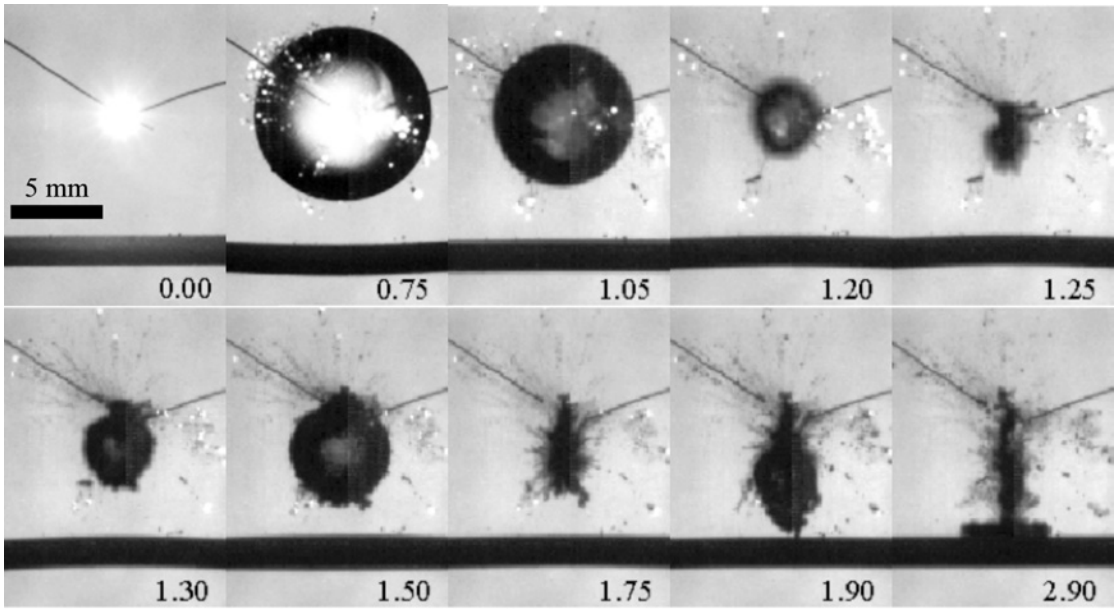

FIGURE 2.3: Collapse phase of the spark bubble at $H' = 1.38$.The times for each frame (in ms) are as indicated. The bubble grows from 0.00 ms to its maximum size of R_{max} = 4.76 mm at 0.75 ms. Thereafter, the bubble contracts with a jet towards the beam as it collapses, and the beam moves slightly towards the bubble. The bubble collapses at $t = 1.25$ ms and expands again as seen at 1.35 ms & 1.50 ms. After this the expanded bubble oscillates towards the rubber beam, finally impinging the surface as shown at 2.90 ms

The collapse of a spark-generated bubble initiated at a moderate distance away from the rubber beam ($H' = 1.38$) is shown in Figure 2.3. The bubble grows from 0.00 ms to its maximum radius of $R_{max} = 4.76$ mm also at $t = 0.75$ ms. At the maximum bubble radius, the center of the elastic beam reached a maximum down deflection of $z_{max,down}$

= 0.435 mm. Thereafter, the bubble collapses non-spherically with a liquid jet towards the beam (t = 0.75 ms to 1.25 ms). While this is happening, the elastic beam is being drawn towards the collapsing bubble, displacing vertically upwards. The beam center reaches a maximum vertical upwards of $z_{max,up}$ = 0.174 mm at t = 1.25 ms. The bubble is observed to re-expand from t = 1.25 ms to 1.50 ms. This expansion and collapse behaviour for the bubble continues and a collapse jet that impinges the rubber beam is observed at t = 2.90 ms. At this stage, the rubber beam has returned to its initial position.

2.1.2.3 Bubble collapse at small *H'*

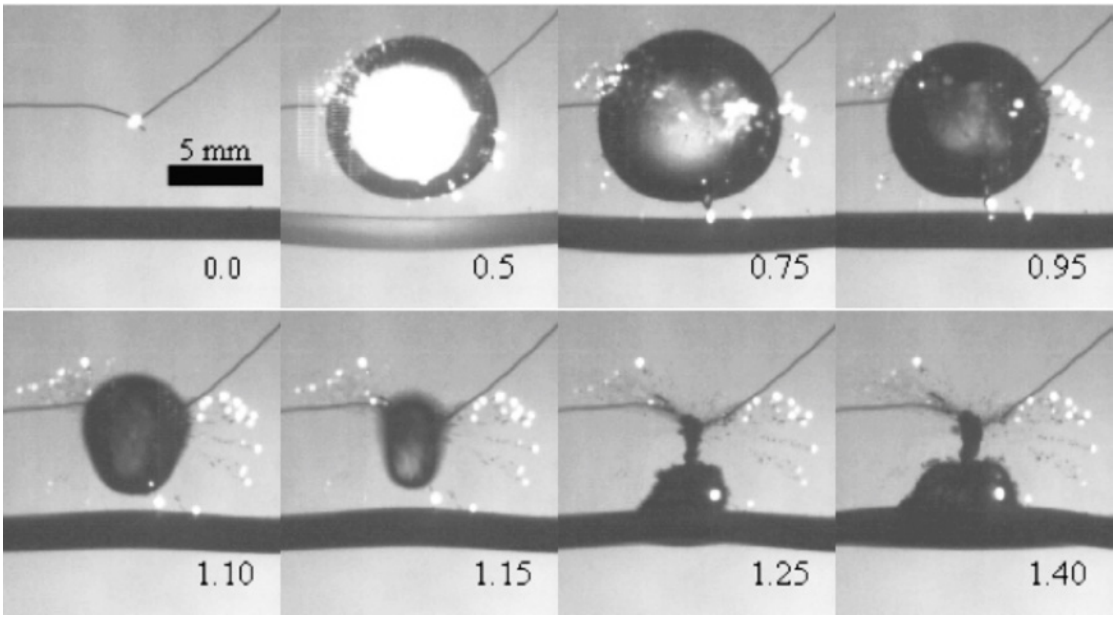

FIGURE 2.4: A spark bubble created at H' = 0.97 away from the rubber beam is shown, with the timings of each frame indicated in ms. The bubble grows from 0.00 ms to its maximum size of R_{max} = 4.64 mm at 0.75 ms. The bubble expansion causes the beam to deform downwards. From 0.95 ms, the bubble contracts non-spherically. The bubble bottom is flattened, and it forms an elongated shape. The bubble collapses at 1.20 ms then re-expands during the time up to 1.40 ms.

In Figure 2.4, we explore the case of a spark-generated bubble created near to the rubber beam at H' = 0.97. The bubble grows from 0.00 ms to its maximum radius of R_{max} = 4.64 mm at t = 0.75 ms. It is noted that the bubble expansion causes the beam to deflect

vertically downwards (t = 0.50 ms, 0.75 ms). The maximum downwards deflection the beam center encounters is $z_{max,down}$ = 0.641 mm at t = 0.50 ms. The bubble contracts non-spherically from 0.75 ms with a flattened bottom and an elongated shape as shown at t = 1.10 ms. The bubble collapses with a liquid jet towards the elastic beam at t = 1.25 ms, and at this point we observe the maximum upwards beam center deflection at $z_{max,up}$ = 0.214 mm. The bubble then continues to re-expand until 1.40 ms, at which the beam has almost returned to its initial position.

2.1.2.4 Bubble collapse at very small *H'*

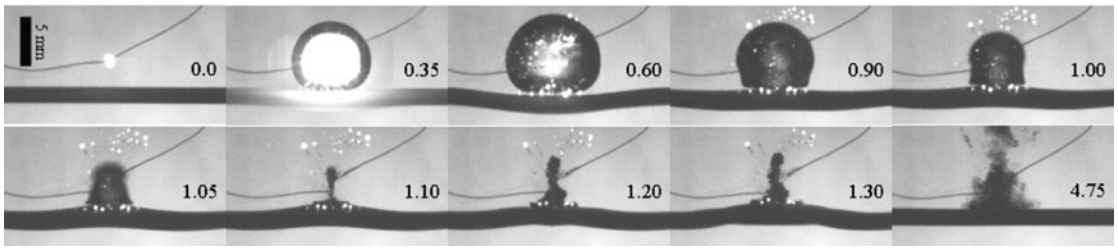

FIGURE 2.5: A spark bubble created at H' = 0.56 away from the rubber beam is shown, with the timings of each frame indicated in ms. The bubble grows from 0.0 ms to its maximum size of R_{max} = 4.64 mm at 0.60 ms. The expanding bubble comes into contact with the beam and causes it to deflect downwards. From 0.35 ms, the bubble contracts non-spherically, with a flattened bubble bottom that is attached to the rubber beam, and finally collapses at 1.10 ms. This bubbly jet re-expands and rebounds, as shown at 4.75 ms. The scale bar is given in the first frame. Timing (in ms) is indicated in every frame.

The final example refers to the case of a spark bubble collapse very near to the rubber beam. In Figure 2.5, a spark-generated bubble created at H' = 0.56 away from the rubber beam. The bubble is shown growing to its maximum size of R_{max} = 4.64 mm, at t = 0.60 ms. During its expansion, much of the bubble is actually in contact with the rubber beam and that forces the beam center to deflect vertically downwards. The maximum downwards beam center deflection for this case is $z_{max,down}$ = 0.812 mm. From 0.60 ms to 1.10 ms, the bubble contracts non-spherically while having the bottom of the bubble attached to the rubber beam. This contraction of the bubble actually causes the

beam center to translate upwards until the bubble collapses at 1.10 ms, where $z_{max,up} =$ 0.299 mm is recorded. The bubble collapses rapidly with a bubbly liquid jet impinging onto the rubber surface and a counter jet is shown to re-expand (1.20 ms, 1.30 ms) and move upwards. The liquid jet impact onto the rising rubber beam surface can actually be visualized through observations on the beam shape. At $t = 1.20$ ms, 1.30 ms, the center of the beam is now seen to propagate downwards and translating this motion to its sides. At around 4.75 ms, the rubber beam is shown to have returned to approximately its initial position.

2.1.2.5 Results summary for different *H'*

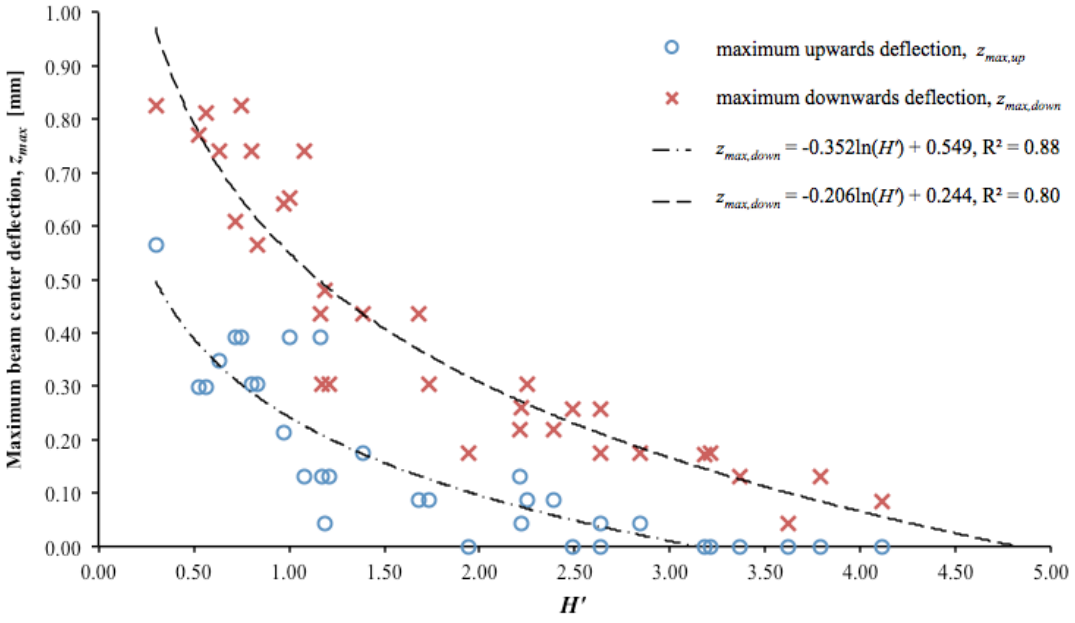

FIGURE 2.6: Graph of maximum beam center deflection, z_{max} vs. dimensionless stand-off distance H' of the cases in this experiment. A logarithmic trend line is fitted to one of the two deflection directions, upwards and downwards.

33 cases are conducted in this study, and a plot of maximum beam center deflections, z_{max} vs. H' is be generated (Figure 2.6). For the bubble beam-interaction in the cases presented, the maximum downwards deflection of the beam center typically occurs when the cavitation bubble reaches its maximum radius; whereas the timing just before the

bubble collapse typically gives the maximum upwards deflection of the beam center. It is noticed from Figure 2.6 that the maximum beam center deflections, both $z_{max,down}$ & $z_{max,up}$ have a trend of decreasing magnitude with increasing H'. An increased distance between the bubble and the elastic beam suggests a weaker interaction between them. It can also be seen from the typical cases presented in Sections 2.1.2.1 to 2.1.2.4. Also from Figure 2.6, the center of the beam is found to return to its original position, and not go above, for all cases above $H' = 3.2$, i.e. $z_{max,up} = 0.00$ mm. Logarithmic trend lines are also fitted to both sets of results and the trend line for $z_{max,down}$ predicted that the finite rubber beam will not be deflected if $H' > 4.8$. Next, it can be seen from the graph that the maximum downwards deflections $z_{max,down}$ are at a larger magnitude than the maximum upwards deflections $z_{max,up}$. Predicted values of $z_{max,down}$ is greater than that of $z_{max,up}$ by around 0.2 mm when $H' = 3.00$ and the difference increases with smaller H'.

2.1.3 Discussion and Conclusion

TABLE 2.1: Experiment measurements for maximum deflections of the rubber beam center $z_{max,down}$ & $z_{max,up}$ vs. dimensionless stand-off distance H'

Case	H'	$z_{max,down}$ [mm]	$z_{max,down}$ [mm]
2.1.2.1	3.18	0.171	≈0.00
2.1.2.2	1.38	0.435	0.174
2.1.2.3	0.97	0.641	0.214
2.1.2.4	0.56	0.812	0.299

Experiments for spark-generated bubble near a finite elastic beam have been conducted. Four cases of varying dimensionless stand-off distance H' were presented, showing pronounced collapse jetting behaviour and increased maximum beam deflections with decreasing H', as shown in Table 2.1. From the typical cases presented, it is also noticed

that the bubble has a tendency to collapse with a liquid jet towards the elastic boundary at small to moderate H', but experiences little influence from the boundary at large H' and collapses spherically. These results from the typical cases are also included in a comprehensive plot of the cases conducted for this study (Figure 2.6). We observe a trend between the two directional maximum beam center deflections and with that are able to predict the effective zone of influence of the neighbouring cavitation bubble onto an finite elastic beam. This influence of the cavitation bubble on the elastic beam can be taken as the sum of $z_{max,down}$ and $z_{max,up}$ from these cases. They are found to decrease with increase H' and the bubble is noticed to collapse spherically without any upwards deflection of the rubber beam centre when H' increases to 3.20 and beyond. The trend also suggests that the beam will not be deflected by the bubble for cases with $H' > 4.8$. And knowing the maximum cavitation bubble radius R_{max}, one should be able to estimate the minimum stand-off distance H for which cavitation activity would be of importance.

It should be mentioned that part of this project is performed in collaboration with Dr. Gong Shi Wei (from IHPC, Singapore) in which she performed simulations based on a method coupling the boundary element method (BEM) potential flow code and a finite element structural solver. This study is intended to investigate the context of an oscillating bubble near different biomaterials and a comparison was made between rubber and materials such as muscle, cartilage, and cervical bone. This is important due to its applicability to many medical procedures in which non-equilibrium bubbles may be present in the vicinity of nearby tissues and biomaterials (Ohl et al., 2009). The collective work was published as Gong et al. (2012).

2.2 Jet orientation of a collapsing bubble near a solid wall with an attached air bubble

A single cavitation bubble in proximity to a solid boundary is a well studied phenomenon (Benjamin and Ellis, 1966; Plesset and Chapman, 1971; Lauterborn and Bolle, 1975; Blake et al., 1986; Tomita and Shima, 1986; Blake and Gibson, 1987; Ohl et al., 1999; Tong et al., 1999; Zhang et al., 2001) and under certain conditions, a liquid jet directed towards the boundary can be observed. It is generally understood that the cavitation damage on a nearby boundary is due to impact from this jet and the impulsive pressure generation during the cavitation bubble collapse (Tomita and Shima, 1986; Ohl et al., 1999; Tong et al., 1999; Blake et al., 1999). The initial distance between the rigid wall and the center of the bubble is an important parameter known as the stand-off distance, H. H is typically smaller than twice of the maximum bubble radius R_{max} for studies on liquid jet impact onto a rigid boundary. However, these liquid jets are also observed on bubbles created at $H > 5R_{max}$ (Blake et al., 1999; Ohl et al., 1998), suggesting that a rigid boundary has a prominent effect on nearby cavitation bubble(s) dynamics. On the other hand, when a cavitation bubble is created near a free surface, it is found to collapse with a liquid jet away from the surface (Chahine, 1977; Blake and Gibson, 1981; Robinson et al., 2001). However in a multiple oscillating bubble system, bubble collapsing jets towards or away from each other have been observed. It is reported that the phase difference between oscillating bubbles is an important parameter that influences the directions of such jets (Fong et al., 2009; Chew et al., 2011). Blake et al. (1993) studied the dynamics of two oscillating bubbles near a plate while Xu et al. (2010) investigated the interactions between an oscillating bubble and an air bubble held in position on a wax thread near a rigid boundary. It was found that the air bubble

and rigid boundary have competing influences with the nearby cavitation bubble. It has been shown experimentally that an air bubble on a rigid boundary could prevent the neighbouring cavitation bubble from collapsing towards the boundary. This suggests the potential of cavitation damage reduction through the use of surface coating with low density, compliant materials, which have been studied in detail previously (Gibson and Blake, 1982; Shima et al., 1989; Tomita and Kodama, 2003). Bubble properties (e.g. maximum radius and relative initial distance from the surface) and the dynamic response of the nearby surface are found to influence the collapse pattern of a nearby cavitation bubble. It is hence one motivation to systematically study the cavitation bubble jetting characteristics when it is in proximity to a rigid boundary 'shielded' by an attached air bubble. A prominent area of application would be the development of a cavitation shield for rigid surfaces. Smith and Mesler (1972) studied the interaction of a spark-generated vapour bubble with an air bubble attached to a solid boundary and reported damage mitigation effects. Reports have shown that the collapse of a wall-attached air bubble is highly dependent on the initial bubble contact angle (Shima and Nakajima, 1977), or the initial deviation from the hemispherical shape (Shima and Sato, 1979). However, Smith and Mesler (1972) did not address the initial shape of the attached bubble in their study which could be an important parameter. Essentially, the conditions to mitigate a neighbouring cavitation bubble jet in this configuration are less studied. It is thus the author's focus to prevent a cavitation bubble collapse jet directed towards a neighbouring rigid boundary through attaching an air bubble onto the boundary. A better understanding of this phenomenon and the conditions under which the boundary shielding effect may occur also forms the scope of this problem. This is achieved through an experimental study shown in this section, and an accompanying numerical simulation study which will be discussed in Section 4.3.

2.2.1 Experimental Setup

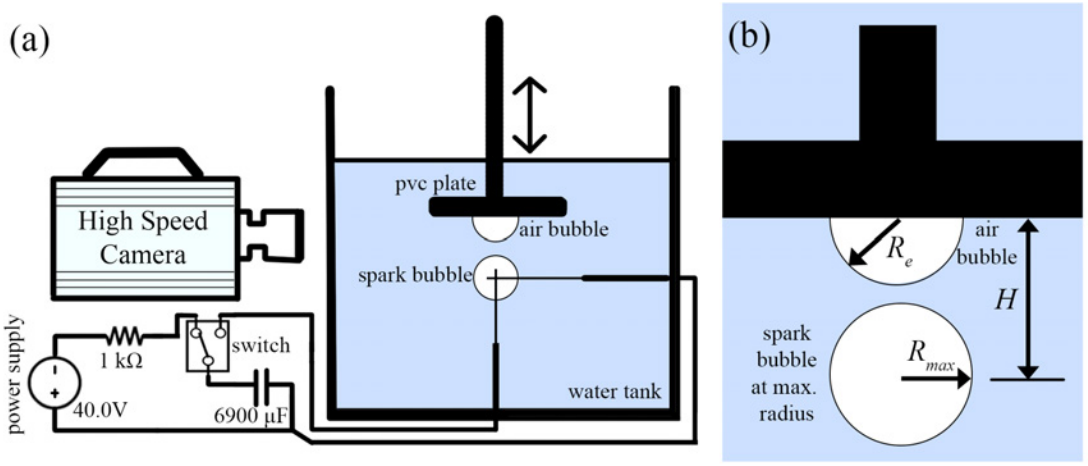

FIGURE 2.7: a) Experimental setup comprising of a spark discharge circuit with crossing 0.1 mm diameter electrodes in a 25 cm x 25 cm x 25 cm tank filled with tap water to a height of 20 cm, a submerged PVC plate (10 cm x 10 cm x 0.5 cm) with an attached hemispherical air bubble, and a high speed imaging system; b) Definition of bubble radii (R_e, R_{max}) and stand-off distance H.

The experimental setup is shown in Figure 2.7a. It is made up of a low-voltage spark-discharge circuit connected to crossing 0.1 mm diameter electrodes, submerged in a 25 cm x 25 cm x 25 cm Perspex tank filled with tap water to a height of 20 cm, a high speed imaging system (Photron RS-X or Photron Fastcam SA4 at 25 kfps frame rate, 1/50,000 s shutter speed, 250 x 250 pixels at around 13 pixels/mm resolution), and a Polyvinyl chloride (PVC) plate with a surface-attached air bubble. The PVC plate surface is cleaned with ethanol to maintain consistent surface properties between every experimental case. An air bubble of 0.01 cc, 0.02 cc or 0.04 cc volume is placed on the underside of the PVC plate (Length 10 cm x Width 10 cm x Thickness 0.5 cm) at its center with a 0.5 cc U-100 Insulin syringe. This allows us to attach a bubble that is hemispherical with a contact angle of $90,^\circ \pm 5,^\circ$. An adaptive active contour method (Boudier, 1997) is adapted to calculate the initial volume of the air bubble, which is used to calculate the equilibrium air bubble radius R_e by assuming that it is perfectly hemispherical. R_e used in the experiment ranges from 1.34 mm to 2.63 mm depending

on the volume introduced. The spark point (or the point of contact of the fine copper electrodes) is adjusted to be vertically under the air bubble center at several distances away from the plate. The electrical circuit used is as described in Section 2.1.1, but the capacitors are charged to 40.0 V before sparking to create the oscillating bubble in this study. As a result, we obtain a bubble with maximum radius R_{max} 2.00 $\pm$ 0.15 mm, which is similar to R_e of a 0.02 cc attached air bubble ($\approx$ 2.1 mm). The definition of other important parameters used in this study are shown in Figure 2.7b, which include the initial stand-off distance H and the maximum oscillating bubble radius R_{max}. The time taken for the spark-generated oscillating bubble from its creation to the first minimum volume or collapse is defined as T. Some 150 experimental cases were conducted and discussed in the following sections. All experiments were performed under atmospheric pressure and at room temperature (24°C).

2.2.2 Results

In studies concerning a cavitation bubble near to a boundary, the dimensionless stand-off distance $H' = H/R_{max}$ is typically the key parameter that influences the bubble dynamics. As such, the influence of observed cavitation bubble jetting behaviour with H' will first be investigated. Following this, typical cases of the different collapse jet behaviours and investigate on the actual physical parameter(s) governing this problem will be presented.

2.2.2.1 Influence of dimensionless stand-off distance

In the present study, a hemispherical air bubble is introduced and attached to the bottom surface of the submerged PVC plate. Therefore, H represents the dimensionless distance

from the attached base of the hemispherical air bubble to the spark point.

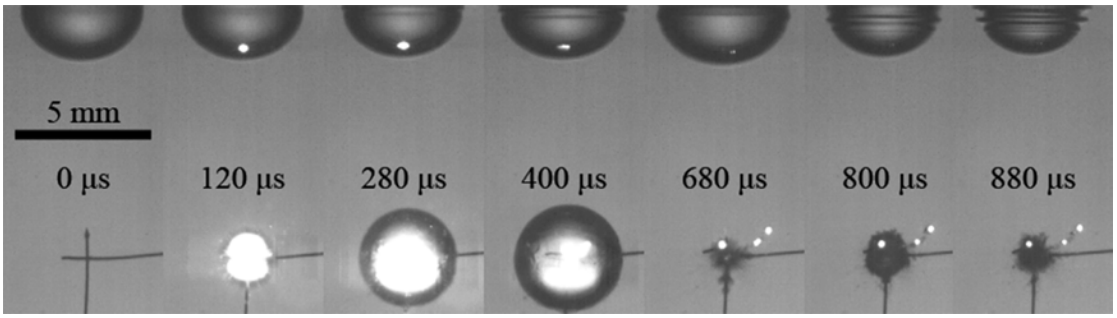

FIGURE 2.8: Case of $H' = 4.54$, $T' = 1.07$, $R_e = 2.07$ mm, $R_{max} = 2.00$ mm. The spark bubble (bottom of frames) reaches its first maximum at t = 400 μs and collapses at $T = 680$ μs. The response of the nearby wall-attached air bubble is shown on top of each frame and the rigid PVC plate is exactly at the top border of the frames. The spark bubble collapses without any visible liquid jet(s). A 5 mm scale bar is shown in the first frame and the respective timings are shown at the center of each frame

Figure 2.8 shows the case of the spark bubble generated far away from the attached air bubble and PVC plate with $H' = 4.54$ and $R_e = 2.07$ mm. On the top of the first frame ($t = 0$ μs) we can clearly see the initial hemispherical air bubble, under which are two crossing electrodes just before spark-discharge. The spark generates an oscillating bubble which grows in size from $t = 0$ μs to 400 μs. This growth is accompanied by a gradual shrinkage of the air bubble size. At time $t = 400$ μs, the spark bubble attains its maximum radius of $R_{max} = 2.00$ mm. Following this, the spark bubble rapidly shrinks and finally collapses at $T = 680$ μs. At the same time, the air bubble rebounds to its initial size as shown in the same frame. There are no observable liquid jets upon the bubble collapse in this case. This expansion and collapse of the spark bubble at such a large H' also has minimal deviations from the spherical shape. A second expansion and collapse of the disintegrated cavitation bubble cloud can be seen at $t = 800$ μs and 880 μs respectively. Surface instabilities on the air bubble can also be observed. The surface waves appear from $t = 280$ μs on the air bubble at its contact perimeter with the solid plate. They are shown to propagate away from the rigid plate and become increasingly prominent, especially after the spark bubble collapse.

For a large $H'(> 4.5)$, this behaviour of cavitation bubble collapse without a liquid jet remains consistent with different R_e or R_{max}. However, when H' decreases to the range of between 1.5 and 4.5, the formation of liquid jet(s) on the spark bubble upon its collapse can be observed. These jet(s) can be classified into three main types: a jet towards the plate, a jet away from the plate, and jets both towards and away from the plate (i.e. oppositely directed jets). Typical cases of each scenario will be presented in the subsequent Sections 2.2.2.2, 2.2.2.3, & 2.2.2.4. When the cavitation bubble is created very close to the boundary ($H' < 1.5$), complex interactions such as venting or coalescence of the bubbles were observed. As the focus is to determine cavitation bubble collapse jet directions, these results are omitted from discussion in this study.

2.2.2.2 Collapsing bubble jet towards plate

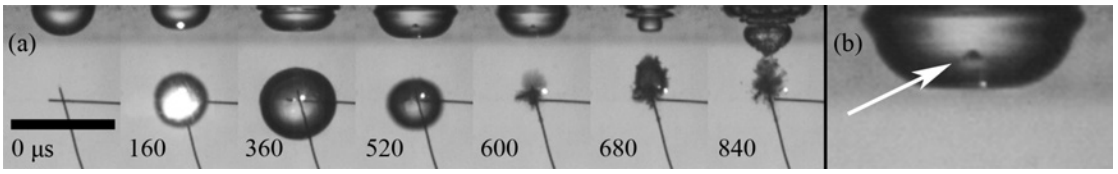

FIGURE 2.9: Cavitation bubble jet towards a wall-attached hemispherical air bubble. The air bubble is shown on the underside of the plate (top border of images). a) $H' = 2.48$, $T' = 1.23$ and $R_e = 1.48$ mm. The cavitation bubble grows its maximum radius $R_{max} = 1.84$ mm at $t = 360$ μs. The air bubble initially contracts, then expands to its first maximum at $t = 520$ μs. Following this, it enters its second contraction phase. At $T = 600$ μs, the cavitation bubble collapses with a jet towards the plate, shown more clearly at $t = 680$ μs in the form of a bubble cloud. The air bubble exhibits prominent surface instability during the cavitation bubble expansion and shape oscillations after the cavitation bubble collapse. A 5 mm scale bar is shown in the first frame and the respective timings in μs are shown at the bottom of each case; b) an enlarged view of fourth frame ($t = 520$ μs) with an arrow pointing to the tip of a visible liquid protrusion in the air bubble.

The first case is when the cavitation bubble collapses with a jet towards the PVC pate. An example is shown in Figure 2.9a, where $R_e = 1.48$ mm and $H' = 2.48$. Similar cases are typically present when the introduced air bubble R_e is smaller than the cavitation bubble R_{max}. The spark at the electrodes contact point creates an expanding cavitation bubble as shown from time $t = 0$ μs to 160 μs. The attached air bubble contracts into

its first minimum volume as the cavitation bubble expands. Slight surface waves on the air bubble can be noticed and they appear to initiate from the liquid-air-solid interface on the air bubble perimeter on the PVC plate. The spark bubble continues to expand non-spherically, with the side closer to the plate slightly compressed with influence of the neighbouring plate and air bubble, until its maximum radius $R_{max} = 1.84$ mm at $t = 360$ μs. Following this, the cavitation bubble enters its collapse phase and contracts. The expanding air bubble is observed to reach its first maximum size at $t = 520$ μs. The air bubble then enters its second contraction phase which continues until $T = 600$ μs when the cavitation bubble collapses. At this instant, a small protrusion direction towards the plate from the bottom surface of the air bubble can be observed (Figure 2.9b). This liquid 'jet' with a bubble cloud propagates towards the PVC plate ($t = 600$ μs, 680 μs, & 840 μs) but does not come in contact with it. The air bubble is observed to undergo distinctive shape oscillations upon the cavitation bubble collapse.

Another case of cavitation bubble collapse jet towards the boundary and attached air bubble is presented in Figure 2.10. In this case however, H' is larger at 3.17 while R_e = 2.05 and $R_{max} = 2.01$ mm. In terms of the bubble dynamics and response, this case is very similar as before. However in this case, the jet that forms within the air bubble during the cavitation bubble expansion is less obvious. This is presumably due to the difference in H', suggesting a weaker interaction between the two. The collapse time of the spark bubble is around 800 μs. As before, the bubble is seen to collapse and jet towards the rigid wall, and this also happens while the air bubble is contracting. Surface perturbations are also present on the air bubble. They are quite similar in that the surface waves propagate from the bubble-wall interface. The waves also appear to initiate as the air bubble is compressed to its minimum volume, and then re-expands.

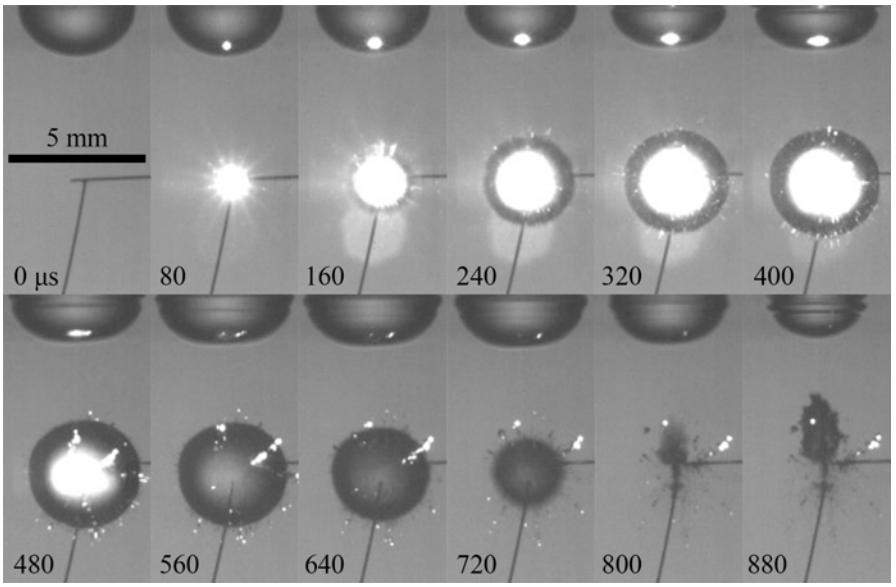

FIGURE 2.10: Cavitation bubble jet towards a wall-attached hemispherical air bubble at a larger stand-off distance. The air bubble is shown on the underside of the plate (top border of images). $H' = 3.17$, $T' = 1.27$ and $R_e = 2.05$ mm. The cavitation bubble grows its maximum radius $R_{max} = 2.05$ mm at $t = 480$ μs. The air bubble initially contracts, then expands to its first maximum at $t = 640$ μs. Following this, it enters its second contraction phase. At around $T = 800$ μs, the cavitation bubble collapses with a jet towards the plate, shown more clearly at $t = 880$ μs in the form of a bubble cloud. The air bubble exhibits prominent surface instability during the cavitation bubble expansion and shape oscillations after the cavitation bubble collapse. A 5 mm scale bar is shown in the first frame and the respective timings in μs are shown at the bottom left hand corner of each case.

2.2.2.3 Collapsing bubble jet away from plate

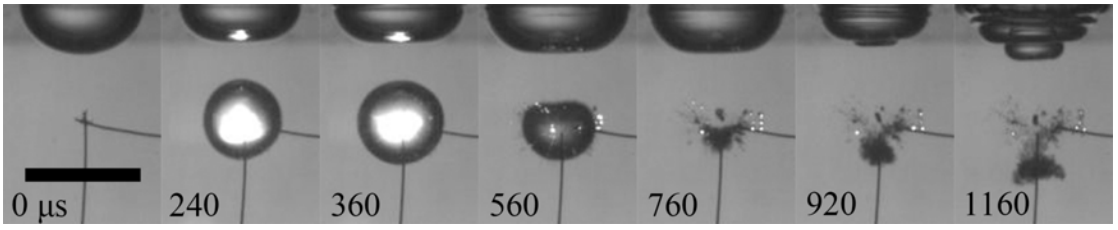

FIGURE 2.11: Cavitation bubble jet away from a rigid plate (top border) with an attached hemispherical air bubble. $H' = 2.77$, $T' = 0.99$ and $R_e = 2.49$ mm. The cavitation bubble grows until its maximum radius $R_{max} = 1.90$ mm at $t = 360$ μs. The air bubble initially contracts, then expands from $t = 240$ μs until the cavitation bubble collapses with a jet away from the plate at $T = 760$ μs (shown by the migrating bubble cloud). The air bubble shows slight surface instability near the plate during the cavitation bubble expansion that becomes more prominent shortly after the cavitation bubble collapse ($t = 920$ μs & $t = 1160$ μs). A 5 mm scale bar is shown in the first frame and the respective timings in μs are shown at the bottom of each frame.

The second scenario is the cavitation bubble collapse with a jet away from the rigid plate. It is most prominent when the attached air bubble has a larger R_e as compared

to the previous case in Section 2.2.2.3. Figure 2.11 shows the case of $R_e = 2.49$ mm and $H' = 2.77$. A spark-generated cavitation bubble expands while the air bubble first contracts after $t = 0$ μs, until its minimum volume at $t = 240$ μs. $R_{max} = 1.90$ mm at $t = 360$ μs after which the cavitation bubble collapses non-spherically with its upper portion compressed and contracting faster than its lower portion, as seen at $t = 560$ μs. This is likely due to the influence from the expanding air bubble at this stage. The air bubble continues to expand until the cavitation bubble collapse at $T = 760$ μs. The two frames after this ($t = 920$ μs & 1.16 ms) show that this jet is directed away from the rigid plate, with a bubble cloud surrounding it. The air bubble also exhibits slight surface instability that propagates from the rigid boundary, but it is not as prominent as that in Figure 2.9. Shape distortions of the air bubble are visible at $t = 1.16$ ms.

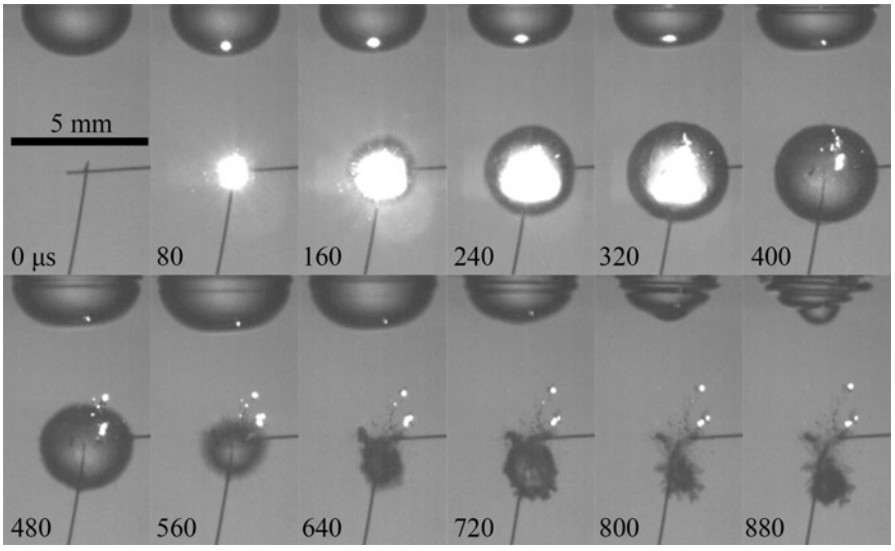

FIGURE 2.12: Cavitation bubble jet away from a rigid plate (top border) with an attached hemispherical air bubble, but with a larger $H' = 3.16$. $T' = 0.98$ and $R_e = 2.00$ mm. The cavitation bubble grows until its maximum radius $R_{max} = 1.91$ mm at $t = 320$ μs. The air bubble initially contracts, then expands from $t = 240$ μs until the cavitation bubble collapses with a jet away from the plate just after $t = 560$ μs. This jet is shown to propagate downwards as seen until the last frame at $t = 880$ μs. A 5 mm scale bar is shown in the first frame and the respective timings in μs are shown at the bottom left hand corner of each frame.

Figure 2.12 is a second representation of bubble collapse away from the wall due to the presence of an air bubble. The parameters for this case are $H' = 3.16$. $T' = 0.98$, and

R_e = 2.00 mm. The cavitation bubble grows until its maximum radius R_{max} = 1.91 mm at t = 400 μs. And at the point of cavitation bubble collapse, the air bubble is seen to be expanding and reaching its maximum volume. The interactions between the two bubbles are similar to that of the case in Figure 2.11 and surface instabilities are present on the air bubble. Again, they appear to initiate just after the air bubble contracts to its minimum volume and expands.

2.2.2.4 Collapsing bubble jet both towards and away (opposite directions) from plate

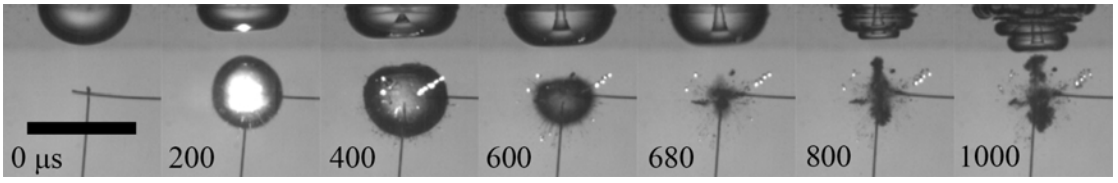

FIGURE 2.13: Cavitation bubble jets both towards and away (oppositely directed) from a rigid plate (top border of frames) with an attached hemispherical air bubble on the underside of the plate. H' = 2.12, T' = 1.09 and R_e = 2.03 mm for this case. The cavitation bubble grows until its maximum radius R_{max} = 1.92 mm at t = 400 μs. The air bubble initially contracts (t = 200 μs) but expands until T = 680 μs when the cavitation bubble collapses. This spark bubble collapse is accompanied with two jets: a jet towards the plate and a jet away from the plate (t = 800 μs, 1000 μs). The air bubble has slight surface instability during the cavitation bubble expansion and prominent shape oscillations after the cavitation bubble collapse. Note that a clear jet can be seen in the air bubble from t = 400 μs onwards which has an estimated velocity of 2 ms^{-1}. A 5 mm scale bar is shown in the first frame and the respective timings in μs are shown at the bottom of each frame.

The last cavitation bubble collapse case is that of two jets, one towards and one away from the PVC plate. This only occurs under specific conditions, which we will investigate in the following Section 2.2.2.5. Figure 2.13 shows a case in which R_e = 2.03 mm and H' = 2.12. The spark-generated cavitation bubble expands to R_{max} = 1.92 mm at t = 400 μs. During the later stages of the cavitation bubble expansion, it is observed to take a non-spherical shape with a flattened upper portion. The attached air bubble initially contracts until its first minimum volume at t = 200 μs before expanding in size. A

budding liquid jet from the underside of the air bubble directed towards the PVC plate can be observed which is most prominent at $t = 400$ μs. This jet comes into contact with the plate surface as shown at $t = 600$ μs with an estimated velocity of 2 ms^{-1} from the frames before this contact. As the cavitation bubble contracts in volume, this liquid jet in the air bubble develops into a water 'channel' that maintains contact with the rigid wall. The spark bubble collapses at $T = 680$ μs. It develops into two bubbly jet streams directed both towards and away from the plate (as shown at $t = 800$ μs & 1 ms). Minor surface instability is also observed on the air bubble in this case during the initial cavitation bubble expansion. The air bubble appears to be close to the end of its first expansion phase and just about to enter its second contraction phase during the cavitation bubble collapse. Shape oscillations can be seen on the air bubble after the cavitation bubble collapse.

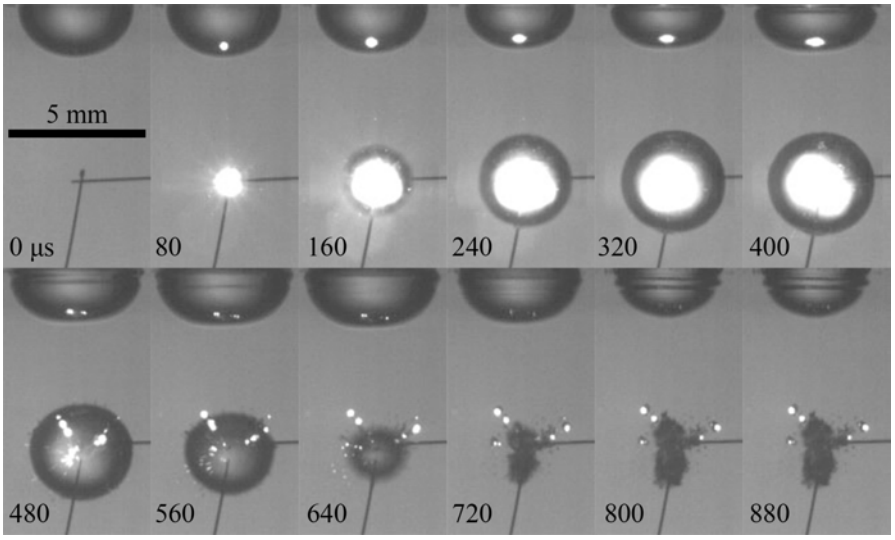

FIGURE 2.14: Second case of cavitation bubble jets both towards and away (oppositely directed) from a rigid plate (top border of frames) with an attached hemispherical air bubble on the underside of the plate. $H' = 3.14$, $T' = 1.14$ and $R_e = 2.06$ mm for this case. The cavitation bubble grows until its maximum radius $R_{max} = 1.95$ mm at t = 400 μs. The cavitation bubble collapses just before $t = 720$ μs. This spark bubble collapse is accompanied with two jets: a jet towards the plate and a jet away from the plate (as seen from $t = 720$ μs to 880 μs). A 5 mm scale bar is shown in the first frame and the respective timings in μs are shown at the bottom left hand corner of each frame.

A second example of oppositely directed jets upon the collapse of a spark bubble is

presented in Figure 2.14 . In this case H' is larger at 3.14, with $T' = 1.14$ and $R_e = 2.06$ mm. The spark bubble expands to its $R_{max} = 1.95$ at $t = 400$ μs. However unlike the previous case, a distinctive jet created within the air bubble that impinges onto PVC plate is not present in this case. Instead, the air bubble is observed to have perturbations on its surface right after its first minimum volume, in a manner more like Figure 2.10 & 2.12. This is likely due to the increased initial distance between the cavitation bubble and the wall-attached air-bubble, causing a diminished influence of the cavitation bubble onto the air bubble. Nonetheless, the cavitation bubble collapses with two jets: one towards and one away from the rigid wall, as seen at $t = 720$ μs to 880 μs.

2.2.2.5 Dimensionless cavitation bubble oscillation time

From the cases presented earlier in Sections 2.2.2.2, 2.2.2.3, & 2.2.2.4, the cavitation bubble collapse jet direction does not seem to depend on the dimensionless stand-off distance H'. For the cases where $H' = 2.48$ (Figure 2.9) & 3.17 (Figure 2.10), the cavitation bubble is observed to collapse with a jet towards the plate; the cases where $H' = 2.77$ (Figure 2.11) & 3.16 (Figure 2.12), a cavitation bubble collapse with a jet away from the plate can be observed; and the cases where $H' = 2.12$ (Figure 2.13) & 3.14 (Figure 2.14), the cavitation bubble collapse with jets directed both towards and away from the plate can be observed. This non-dependency of H' to the collapse jet direction suggests that there are other governing parameter(s) on the dynamics in this problem. Further observations on the cases suggest that the phase difference between the cavitation bubble and the air bubble appears to have an effect on the bubble collapse jet directions. If the air bubble is expanding when the cavitation bubble collapses, there is a tendency for the jet to be directed towards the plate (Figures 2.9 & 2.10). Conversely,

if the air bubble has started to contract again during the cavitation bubble collapse, it appears to induce a jet away from the PVC plate (Figures 2.11 & 2.12). This is alike observations in the literature that the phase difference between two neighbouring oscillating bubbles has an influence in the bubbles' collapse jet directions (Fong et al., 2009; Chew et al., 2011).

We can evaluate the phase difference between the cavitation bubble and air bubble in this problem by comparing the oscillation time of the spark-generated bubble and the theoretical natural period of oscillation of an initially quiescent air bubble. We can introduce a new parameter, the dimensionless cavitation bubble oscillation time T' in this section.

$$T' = \frac{T}{2\pi R_e \sqrt{\frac{\rho}{3\gamma_2 p_\infty}}} \tag{2.1}$$

The numerator T here refers to the experimentally measured spark bubble oscillation time, the time taken from the creation of the spark to the first collapse of the bubble. It is directly related to $R_{max}\sqrt{\frac{\rho}{p_\infty - p_v}}$, in which p_v is the unknown vapour pressure. ρ and p_∞ refers to the liquid density (ρ = 1000 kg.m^{-3}) and reference pressure (p_∞ = 100 kPa) respectively. The spherical air bubble has a theoretical resonant frequency (Minnaert frequency) of $f = \frac{1}{2\pi R_e}\sqrt{\frac{3\gamma_2 p_\infty}{\rho}}$, where γ_2 (= 1.4) is the ratio of specific heats of air (Minnaert, 1933). The denominator in Equation (2.1) is the theoretical period of oscillation of an air bubble $T_a = \frac{1}{f} = 2\pi R_e\sqrt{\frac{\rho}{3\gamma_2 p_\infty}}$. This relationship essentially is also applicable to a surface-attached hemispherical bubble of equilibrium radius R_e (Tho et al., 2007; Blue, 1967).

Figure 2.15 shows a plot of T' against H' and we notice that the spark bubble collapse jet directions are dependent on T'. For T' smaller than unity (< 1.0), we observe a tendency for jets directed away from the plate to occur. Jets towards the plate are typically found

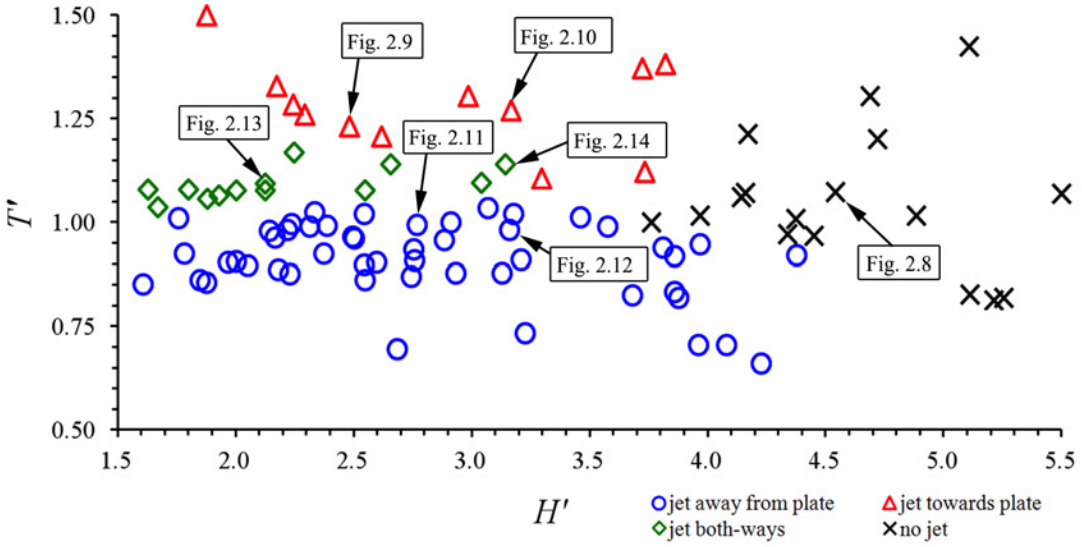

FIGURE 2.15: Dimensionless cavitation bubble oscillation time T' against dimensionless stand-off distance H' showing groups with different cavitation bubble collapse jet directions. Cavitation bubble collapse without a jet is observed for all cases with H' more than 4.5 (indicated with crosses). At smaller $H' < 3.3$ we observe 3 types of collapse jets; firstly, a jet towards the plate, (indicated with triangles); secondly, a jet away from the plate (indicated with circles); and thirdly, jets simultaneously towards and away from the plate (lozenges in the figure). For $H' > 3.3$, cases with jets that go both-ways were not observed but instead cases with spherical collapse were seen

at larger $T'(> 1.2)$. The majority of cases with jets directed both towards and away from the plate during the cavitation bubble collapse occur at T' of approximately 1.1. This observation is consistent for H' lesser than 3.3, beyond which oppositely-directed jets no longer appears in the experiments.

This shows that a larger T' has the capacity to influence the cavitation bubble to jet towards the rigid plate with an attached bubble. On the other hand, when T' is relatively small, a cavitation bubble collapse jet away from the plate tends to occur. There are two parameters that could result in T' across the experiments and they are the difference between the characteristic bubble radii and the vapour pressure p_v, both of which influences the bubble oscillation times. If R_e and R_{max} are largely disparate, the jetting direction can be predicted depending on which of the two values is greater. For instance, if R_e is $\gg R_{max}$, T_a should be greater than T, giving us a T' lesser than 1.0

and predicting a jet away from the rigid plate. The same holds for $R_e \ll R_{max}$, T_a lesser than T, large T' and correspondingly a liquid jet away from the rigid plate.

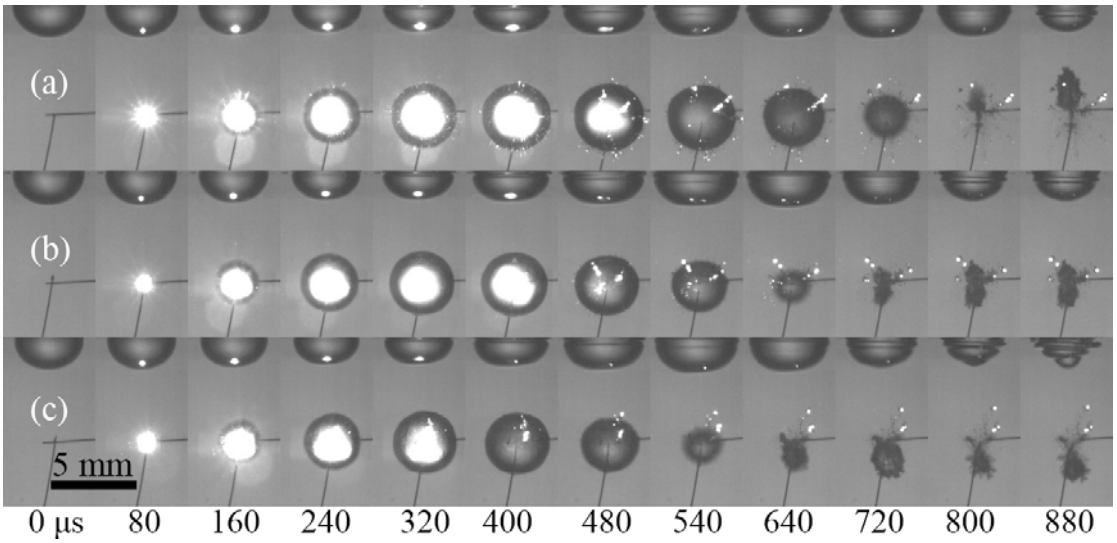

FIGURE 2.16: Cavitation bubble collapse a) jet towards plate ($R_e = 2.05$ mm, $R_{max} = 2.01$ mm, $H' = 3.17$, $T' = 1.27$); b) jet both-ways ($R_e = 2.06$ mm, $R_{max} = 1.95$ mm, $H' = 3.14$, $T' = 1.14$); c) jet away from plate ($R_e = 2.00$ mm, $R_{max} = 1.91$ mm, $H' = 3.16$, $T' = 0.98$). The three case were presented earlier as Figures 2.10, 2.14, & 2.12. However as they possess similar R_e, R_{max} and H' but different T', they are reproduced here for comparison. The cavitation bubble is created below an attached air bubble on a PVC plate. The plate boundary is exactly at the top border of each individual frame. The frames are displayed from left to right with the timing of the first frame being 0 μs and the last frame 880 μs. A 80 μs time difference is present between adjacent frames. Each set shows the growth and collapse of a cavitation bubble and the direction of the jet(s). A common 5 mm scale bar is shown at the bottom left hand corner.

However when the R_e and R_{max} are comparable, the collapse jet directions are more difficult to predict since the influence of p_v may be important. As p_v affects the cavitation bubble collapse time, it is therefore worthwhile to investigate how p_v may affect the collapse jet direction given similar radii of the air bubble and cavitation bubble. Figures 2.16 above shows three cases of comparable R_e, R_{max}, and H', but exhibiting different collapse jet directions and T'. These cases are presented in the earlier subsections as a typical case of each jet direction (as Figures 2.10, 2.14, & 2.12), but compiled here to allow an easier comparison. A wall-attached air bubble is on the top of each frame, under which shows the growth and collapse of a spark-generated cavitation bubble. The timing between each consecutive frame is 80 μs. Figure 2.16a is the case of a

cavitation jet towards the rigid wall with $R_e = 2.05$, $R_{max} = 2.01$ mm, $H' = 3.17$, and $T' = 1.27$. Figure 2.16b shows a case of oppositely-directed jets, both towards and away from the wall, with $R_e = 2.06$ mm, $R_{max} = 1.95$ mm, $H' = 3.14$, and $T' = 1.14$. Finally, I show the case of a collapse jet directed away from the wall in Figure 2.16c with R_e = 2.00 mm, $R_{max} = 1.91$ mm, $H' = 3.16$, and $T' = 0.98$. It can be observed from the images that the case in Figure 2.16a takes the longest time to collapse, followed by that in Figure 2.16b and lastly Figure 2.16c. The consequence is a change in jet direction from towards the plate to away from the plate. This is also shown with decreasing values of $T' = 1.27$, 1.14 and 0.98. The reason for this difference is due to p_v which increases T and correspondingly T'. We have validated this observation with numerical simulations that will be discussed in Section 3.2.

2.2.3 Discussion and Conclusion

The results illustrate the presence of two key parameters in this problem of a cavitation bubble with a nearby rigid wall-attached air bubble. They are the dimensionless stand-off distance H' and the dimensionless cavitation bubble oscillation time T' (which essentially expresses the phase difference between the bubbles). It is noticed from the experiments that $H' \geq 4.5$ should be the requirement for a cavitation bubble to collapse spherically without any distinct jet(s) near a wall with a hemispherical air bubble. For the simpler case of a cavitation bubble collapse near a rigid boundary, the jets are predicted or noticed at larger values of H' (e.g. 5.2, Blake et al. (1999) or 5.9, Ohl et al. (1998)). The results could show that there is a competing influence of the rigid wall and the air bubble onto the cavitation bubble. When $1.5 < H' < 4.5$, jet(s) from a collapsing cavitation bubble typically occur. The cavitation bubble may collapse with jet(s) directed towards, away from, or both towards and away from, the rigid boundary. Sections 2.2.2.2, 2.2.2.3,

& 2.2.2.4 show the typical cases for each of these jet directions. We observe surface instabilities on the air bubble in all cases. These surface waves form at the liquid-air-solid interface on the wall-attached air bubble and they propagate downwards on the bubble shell. They also appear to initiate after the air bubble stops its initial contraction and begins expanding. With velocity in the order of 1 ms^{-1}, they appear to be capillary ripples. Hocking (1987) reported that the limiting case for surface capillary-gravity waves in a bounded region happens when the free surface is in contact with the boundary orthogonally. Such waves motions are also shown on a hemispherical air bubble on an oscillating solid plate (Zoueshtiagh et al., 2006; Fayzrakhmanova et al., 2011), which is similar to the observations with the approximately hemispherical wall-attached air bubble. We also observe induced jets within the attached air bubble directed towards the rigid wall during the cavitation bubble oscillation. These jets may or may not touch the plate depending on experimental parameters such as H' and R_e. The velocities of these liquid jets are also approximately one order of magnitude smaller as compared to the jet of a similar cavitation bubble just beside a rigid boundary (up to 80 ms^{-1}) (Versluis et al., 2000; Ohl et al., 2006). Therefore, we may assume that these induced jets are less damaging than a neighbouring cavitation bubble collapse with an impacting jet onto a rigid boundary, without an attached air bubble.

It is found that the dimensionless cavitation bubble oscillation time T' is the primary parameter to determine the cavitation bubble collapse jet direction for $1.5 < H' < 4.5$. If T' is greater than 1.2, a collapsing jet directed towards the plate can be observed. If T' is lesser than 1.0, we observe a jet directed away from the rigid boundary. However when T' is approximately 1.1, the spark bubble splits up in two parts during its collapse and generates both an upwards jet and a downwards jet. However, if R_e and R_{max} are disparate, the effect of p_v could be significant. The main reason behind this observation

of varying collapse jet direction is the phase difference between the two bubbles in this problem. Numerical simulations are also conducted to better understand the physical mechanisms behind this problem. The results are shown in in Chapter 4, Section 4.2.

Finally, it is notable that none of the collapsing liquid jets from the cavitation bubble came in contact with the PVC plate in all of the cases. Although the effect bubble coalescence at low H' is not studied, it is highly likely the addition of a wall-attached air bubble is effective in protecting a rigid boundary from an impinging cavitation bubble collapse jet.

2.3 A low-voltage spark-discharge method for generation of consistent oscillating bubbles

The underwater spark generation method has been widely used to study cavitation dynamics due to its relative simplicity in experimental setup (Burtsev and Shamko, 1977; Buogo and Cannelli, 2002; Lu et al., 2002; Buogo et al., 2009; Lew et al., 2007; Khoo et al., 2009; Pain et al., 2012; Gong et al., 2012). The basis of an underwater spark discharge method is the impulsive discharge of current through two electrodes from a charged capacitor. The electrodes are commonly separated by a small gap, also known as the spark cap. Such methods are known as high-voltage underwater spark-discharge methods due to the requirement of a very high initial capacitor voltage requirement, ranging from 2 kV to 20 kV (Burtsev and Shamko, 1977; Buogo and Cannelli, 2002; Lu et al., 2002; Buogo et al., 2009). The major concerns of these methods are the handler's safety as well as consistency of results due to the high voltage. In recent years, low-voltage underwater spark-discharge methods have emerged. They utilize a pair of fine electrodes in contact, lowering the potential difference requirement for spark

generation to under 100 V (Lew et al., 2007; Khoo et al., 2009; Pain et al., 2012; Gong et al., 2012; Goh et al., 2014b). This includes the two studies used in the previous two sections, Sections 2.1 & 2.2. The benefits of these methods include safety (due to the low voltage used), simple and cheap setup, and less influence on the generated bubble dynamics with the use of finer electrodes as compared to high-voltage methods. However, one inherent disadvantage of this method is the breaking of electrodes during spark-discharge, highlighting the need for adjustments or replacements of electrodes at experiment intervals.

Regardless of high-voltage or low-voltage spark-discharge methods, obtaining consistent oscillating bubble characteristics has been challenging for experimental scientists. The maximum bubble radius of the generated bubble , which is related to the energy discharged through the electrodes (Buogo et al., 2009; Mackersie et al., 2005), is a key parameter of interest. It is proven to be difficult to obtain consistent and predictable bubble radii with underwater spark-discharge methods. For high-voltage spark-discharge, Buogo et al. (2009) obtained a large scatter of maximum bubble radii, with the largest bubble radius obtained almost twice of the smallest bubble radius with other parameters constant. Low-voltage spark-discharge methods typically also create bubbles with a large range of maximum radii of 3 to 5 mm (Lew et al., 2007; Khoo et al., 2009). A possible explanation for this consistency is the influence of contact bounce from mechanical switches and electromechanical relays. This undesirable effect is a cause of intermittent making and breaking of contacts when the switch is triggered. The bounce time for a closing switch can be a few milliseconds (Biagi and Zanini, 1993) and such fluctuations could lead to inconsistent energy transferred. Another possible source of inconsistency is the use and setup of the electrodes. As the maximum bubble radius is related to the amount of dissipated energy between the submerged electrodes, a variation in electrode

length alters the total resistance and corresponding the current of the discharge circuit. With a constant potential difference, this results in inconsistent energy dissipation. The position and force at the contact points of the two electrodes when primed may also influence the time taken for the electrodes to break contact upon spark-discharge.

In this study, a novel low-voltage spark-discharge method which aims to repeatedly create spark-generated bubbles of consistent maximum radii is presented. This is important for enhancing control in experimental studies of cavitation bubble dynamics, for instance towards studies concerning a non-spherical inertial bubble growth and collapse where changes in obtained bubble shape and size can be evaluated.

2.3.1 Experimental Setup

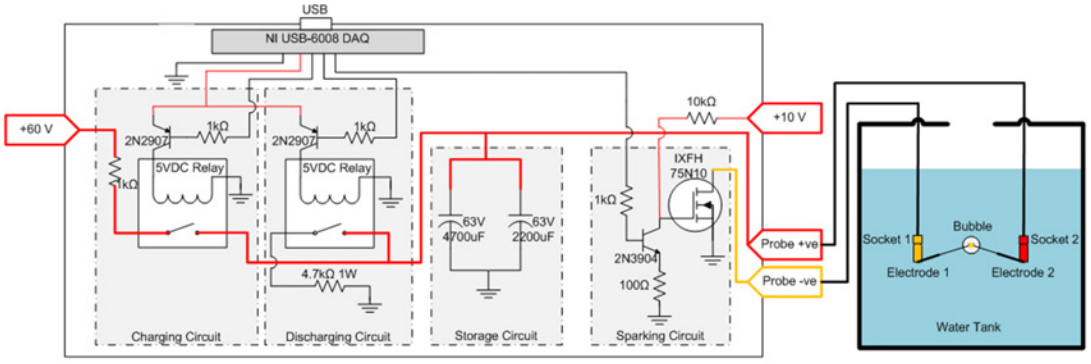

FIGURE 2.17: Experimental circuit comprising of four sub-circuits: a charging circuit, with a 60 V DC power supply; a discharging circuit, with a 4.7 kΩ resistor; a storage circuit, with 6900 μF in two capacitors; and a sparking circuit, with a 10 V DC power supply to trigger a n-channel MOSFET connected to touching electrodes submerged in a Perspex tank filled with de-ionized water.

The experimental setup, comprising of a novel spark-discharge circuit is shown in Figure 2.17. A typical setup for bubble dynamics study also include a high-speed imaging system, power supplies and oscilloscope. The electrical circuit can be divided into four sub-circuits (marked out in Figure 2.17) that serve different purposes, namely charging, storage, discharging, and sparking. These circuits are centrally controlled by a National

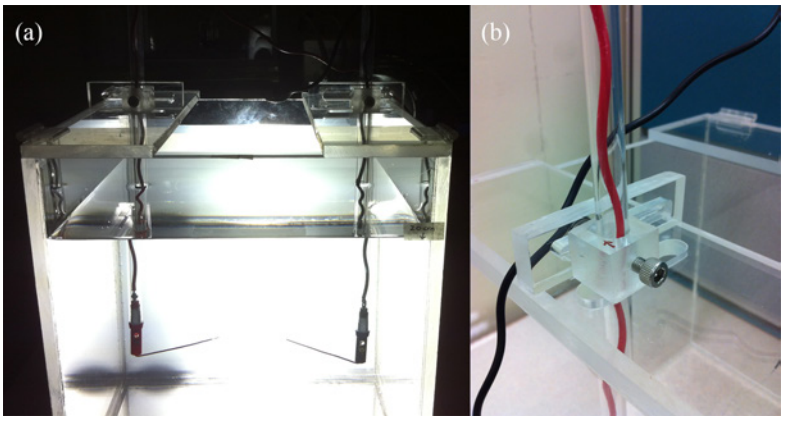

FIGURE 2.18: (a)Backlit tank setup (b) Traversing mechanism for electrodes placement and adjustment

Instruments NI USB-6008 Data Acquisition Unit connected to a computer. In the charging circuit, a Topward Electric Instruments TPS-2000 60V 3A DC power supply at 60 V is used and charging is carried out through a 1 kΩ resistor. The storage circuit comprises of a 2200 μF, 63V capacitor and a 4700 μF, 63V capacitor connected in parallel thus giving a total capacitance of 6900 μF. A discharging circuit is present to safely discharge the capacitors through a 4.7 kΩ resistor. This circuit is engaged should charging beyond the intending voltage occur and to ensure a consistent starting state in the conduct of each experiment. It is also deployed to completely discharge the capacitors at the end of each experiment or when the operator is to come in contact with the water (the nature of the circuit keeps the water tank charged at the voltage across the capacitors). A grounding stick can also be used before any adjustments as a safety precaution. The final sub-circuit is the sparking circuit, which comprises of a 75A 100V N-channel metal-oxide semiconductor field-effect transistor (MOSFET) (IXYS IXFH75N10) responsible for discharging the capacitors through a pair of probe terminals. A DC power supply at 10 V is required to trigger the MOSFET. The relays used in these circuits are Omron G4A-1A-E 5V DC.

A pair of electrodes is connected to the terminals of the discharge circuit and submerged

in a Perspex tank of dimensions 25 cm x 25 cm x 25 cm. The tank is filled with de-ionized water to a height of 20 cm and the electrodes are arranged to touch using a traversing mechanism on the top of the tank (Figure 2.18). This mechanism is on both sides of the tank and comprises of two slot channels (horizontal and vertical) through which two bolts are fastened onto a Perspex slider. This allows for two-directional motion with rotation of the submerged sockets to which the electrodes are connected. The use of electrical sockets allow for changing of electrodes after each experiment to ensure consistent start-state. Multiple pairs of electrodes are prepared and each of them is made up of a 100 mm long, 0.6 mm diameter single core tinned copper wire with one end soldered to a banana plug and the other end stripped at 20 mm from the tip. A 0.1 mm tinned copper wire, which is obtained from a 10/0.1 multi-core electrical wire of different lengths L = 10 mm, 20 mm, 30 mm, 40 mm or 50 mm, is soldered at the free end of the wire. This configuration is shown in Figure 2.19, and the electrode will be plugged into each of the two submerged socket for adjustments to touch at a point 100 mm vertically from the base of the tank. This point is adjusted to be at the center of the tank, equi-distant from each of the tank's side walls using scales on top and at the bottom of the Perspex tank. For every experiment in this study, the fine tip of an electrode is placed approximately 1 mm away from the final desired position before the other electrode is adjusted by displacing it back in place and ready to spark.

The activation of the charging, discharging and sparking circuits is controlled by a program with a Graphical User Interface created for this circuit using NI LabVIEW (Figure 2.20). This program obtains data from the NI USB-6008 DAQ unit and sends out signals to turn the relays 'on' or 'off' via transistors to charge and discharge the capacitors. The NI USB-6008 DAQ unit is also responsible for switching on the MOSFET at a 100 ms time frame for sparking to be achieved. For this experiment,the

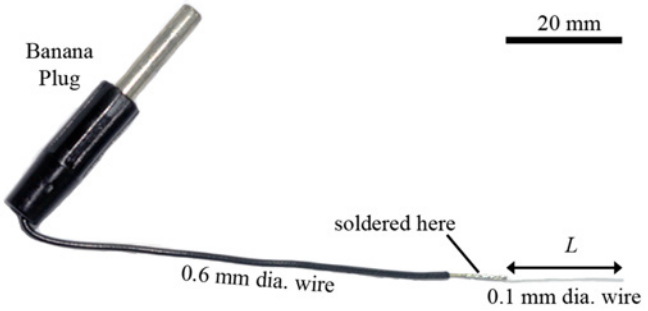

FIGURE 2.19: Schematic showing the configuration of one electrode. A 0.6 mm diameter wire is soldered at one end to a banana plug and at the other end soldered to a 0.1 mm diameter wire of length L. A 20 mm scale bar is shown at the top right hand corner of the image.

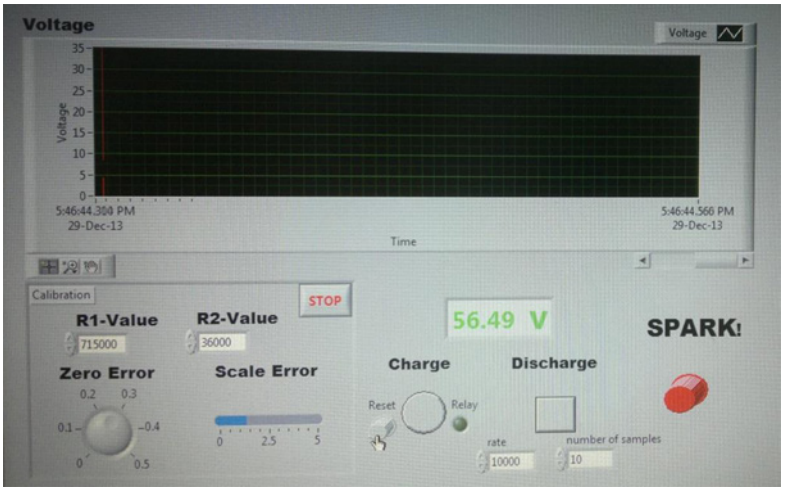

FIGURE 2.20: Graphical User Interface of program in Labview for circuit control. The buttons or icons displayed perform tasks like charging, discharge, and spark(-discharge).

charging circuit is first activated for the capacitors to reach 60.0 V and then charging is halted. The voltage across the capacitors is monitored using a Rigol DS 1004B digital oscilloscope and the discharging circuit can be deployed in case of over-charging. With the electrodes in place, pressing the 'SPARK' button on the circuit (Figure 2.20) will discharge the capacitors to the electrodes through the MOSFET. This is achieved by pulling the potential at the MOSFET's 'Drain' terminal to ground, creating a 60.0 V potential difference and correspondingly a large current flow across the electrodes. The resistance of the sparking circuit is greatest at the point of contact of the two electrodes because of the minimal conducting cross-sectional area. The discharged energy at the contact point creates a spark in which a portion of the fine electrodes breaks at that

point. The dissipated energy at this point creates a spark, which in turns creates an oscillating vapour bubble. This whole process is recorded with a high-speed camera (Photron Fastcam SA5) at 50 kfps and a shutter speed of 1/81,000 s. The images are recorded at 320 x 320 pixel, corresponding to a resolution of around 16 pixels/mm. A Sumita LS-MS350 light source is used for illumination of the tank and the light is diffused using tracing paper placed on the projecting side of the tank. Around 150 runs were performed to create spark-generated bubbles for this experiment. All cases were performed under atmospheric pressure at room temperature (23.5 °C).

2.3.2 Results

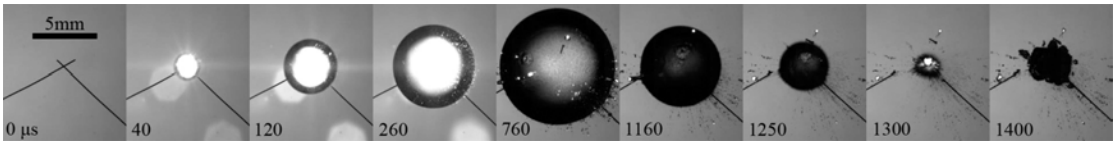

FIGURE 2.21: A typical spark bubble growth and collapse with this setup. Frame 1 (from left to right) shows a pair of $L = 20$ mm electrodes in contact initially at $t = 0$ μs. During capacitive discharge, a spark at the contact point grows into an oscillating bubble ($t = 40$ μs) which expands to its maximum radius $R_{max} = 4.53$ mm at $t = 760$ μs. From then on, it contracts until its first collapse at $t = 1.30$ ms. The frame at $t = 1.40$ ms shows the second expansion of the disintegrated bubble cloud. A 5 mm scale bar is shown at the top of the first frame and corresponding time (in μs) is shown at the bottom left hand corner of each frame.

Single spark-generated bubbles can be repeatedly generated with the setup. To evaluate on the consistency and efficiency of this method, we study the typical growth and collapse of the generated bubble (Figure 2.21). The first frame in Figure 2.21 shows that there is a portion on each of the two fine electrodes that extends beyond the contact point which is included in the definition of L. This extended length is maintained to be less than 1 mm for all experiments hence are assumed to have negligible effects for subsequent discussions. The bubble expands to first maximum bubble radius, represented by R_{max}, before collapsing into a minimum bubble volume. $t = 0$ μs, 40 μs shows the bubble generated at the point the two fine electrodes (each of $L = 20$ mm) touch, causing spark

during electrical discharge. The bubble grows into its maximum radius $R_{max} = 4.53$ mm as shown at $t = 760$ μs. It rapidly collapses into a minimum volume at $t = 1.30$ ms. After the collapse, the single bubble disintegrates into a bubble cloud which then expands again ($t = 1.40$ ms). This bubble is generated more than 20 R_{max} away from the walls and free surface of the water tank, which can be assumed to be created within an infinite fluid medium.

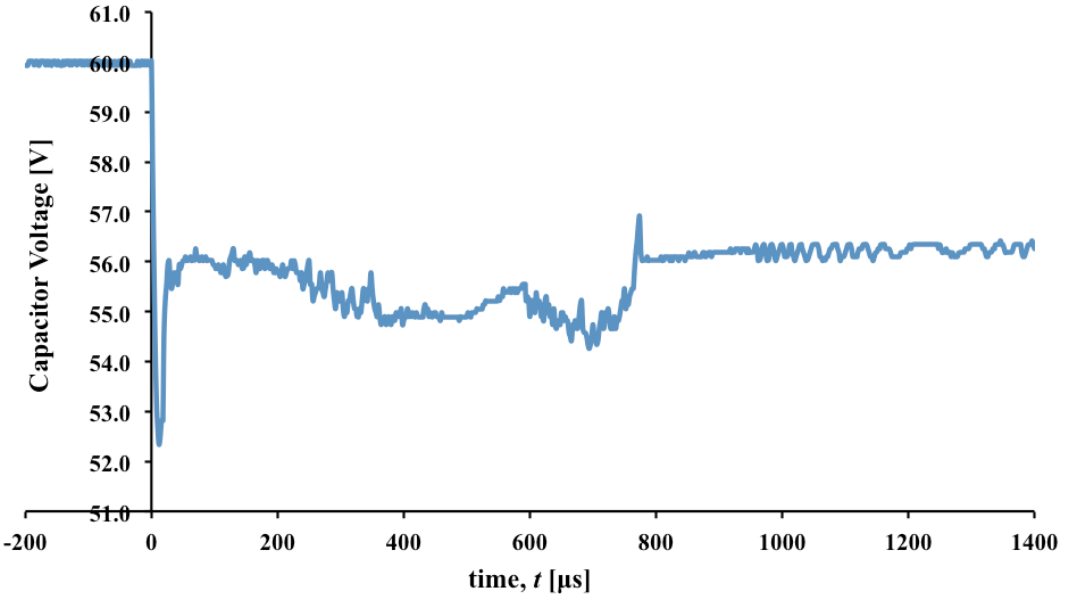

FIGURE 2.22: Capacitor voltage against time during typical spark bubble oscillations of case 2.21

The voltage drop across the capacitors during the spark-discharge of the typical case shown in Figure 2.21 is also monitored. This is presented as a voltage against time plot in Figure 2.22 and the timing t in this plot corresponds to that shown in the earlier typical case (Figure 2.21). When $t = 0.00$ μs, a spark is created across the touching electrodes due to the MOSFET activation and the capacitor voltage drops sharply from 60.0 V to 52.3 V. This voltage drop is better seen at Figure 2.23 which shows the initial 40 μs after spark-discharge. This begins as a rather linear drop from 60.0 V ($t = 0.00$ μs) to 52.3 V (around 12 μs). The voltage then remains below 53.0 V before rising sharply to around 55.0 V at $t = 20.0$ μs. This is likely a result of the vaporizing of the electrodes

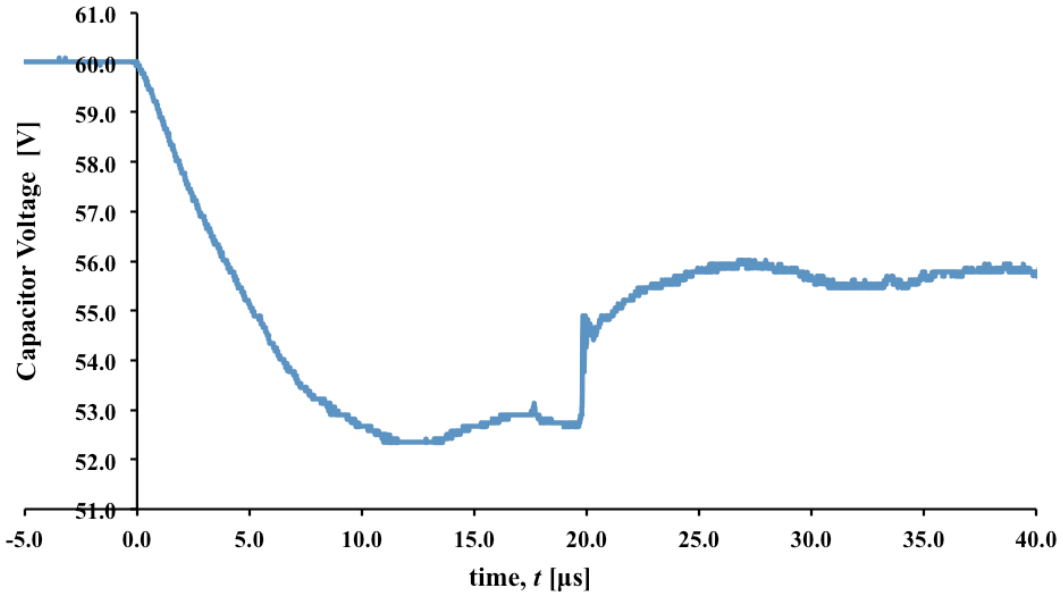

FIGURE 2.23: Expanded view of the initial timings of the capacitor voltage against time during typical spark bubble oscillations shown in Figure 2.22

near the initial point of contact, which causes very much increased resistance in that part of the discharge circuit. The capacitor voltage then fluctuates between 54.0 V and 56.0 V up until almost $t = 800$ μs when it rises rapidly. After this rise to around 57.0 μs, the voltage dips and then remains rather consistent at around 56.0 V until $t = 1.4$ ms. If we compare this against Figure 2.21, it can be noticed that the bubble reaches its maximum radius at $t = 760$ μs. This corresponds to the timing at which the voltage is seen to rise up to around 57.0 V. And from the frames showing the first expansion of the cavitation bubble in Figure 2.21, the bubble is seen to be much brighter at its core due to the spark. This spark appears to diminish as the bubble reaches its maximum radius. This suggests that current continues to flow across the separated electrodes within the vapour bubble, despite a heightened resistance due to the breakage in electrode contact. From $t = 1.25$ ms to 1.40 ms in Figure 2.21, the fine electrode on the left is clearer separated from the bubble and electrode on the left. This suggests a greatly increased resistance at this part of the discharge circuit and that essentially halts current flow across the electrodes.

In the following subsections, several parameters that would determine the spark bubble R_{max} obtained and its consistency will be investigated.

2.3.2.1 Bubble size dependency on electrode length *L*

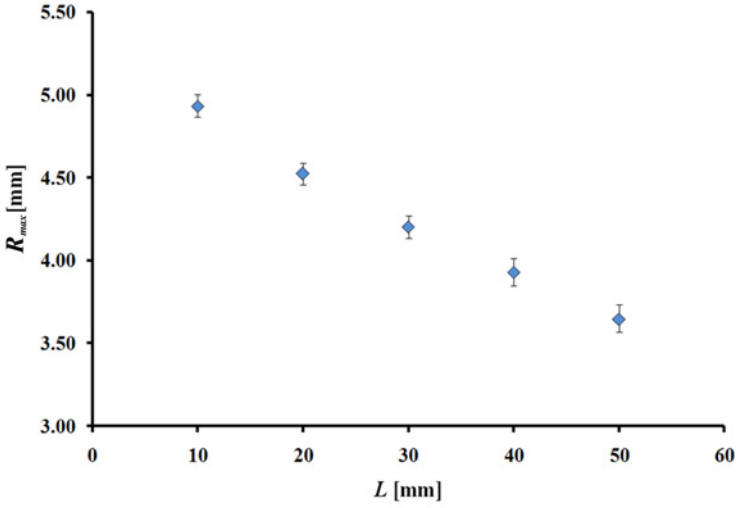

FIGURE 2.24: Graph of maximum spark-generated bubble radius R_{max} against length of 0.1 mm diameter wire per electrode, L. Around 150 experimental cases are shown here with standard deviation bars shown for each data set.

The primary objective of this experiment is to obtain consistent maximum bubble radius R_{max}, in which we should maintain parameters, such as electrode length L and discharge voltage, constant across all experiments. However, we can vary one of these parameters while keeping the other constant to evaluate on the bubble size dependency on a particular parameter. In this case, experiments are conducted using electrodes of different L (from 10 mm to 50 mm) and Figure 2.24 shows the corresponding maximum bubble radii R_{max} obtained. Results show that by keeping L constant, we are able to obtain consistent R_{max}. For instance, for a pair of electrodes with $L = 30$ mm each, bubbles obtained are with a mean $R_{max} = 4.20$ mm, within standard deviation $\sigma = 1.6$ %. When L is increased to 50 mm each, bubbles of mean $R_{max} = 3.67$ mm, with $\sigma = 2.5$ % are generated.

TABLE 2.2: Mean maximum bubble radius $\dot{R_{max}}$ obtained for different initial fine electrode wire lengths L.

L (mm)	10	20	30	40	50
$\dot{R_{max}}$ (mm)	4.93	4.52	4.20	3.93	3.64
Std. Dev. σ (%)	1.6	1.4	1.6	2.1	2.5

Table 2.2 shows the different L configurations and the corresponding mean maximum bubble radius, represented by $\dot{R_{max}}$, and standard deviation σ, in which $\sigma \leq 2.5$ % for the 150 experiments conducted. $\dot{R_{max}}$ decreases with increase in fine electrode length L, however in a non-linear fashion. When L is increased from 10 mm to 20 m, the $\dot{R_{max}}$ decreased by 0.39 mm. However when L is increased from 40 mm to 50 mm, $\dot{R_{max}}$ only decreased by 0.29 mm. It appears that as the fine electrodes become shorter in length, there is a correspondingly larger increase in R_{max}. The difference in circuit resistance shall be evaluated in the next Section 2.3.2.2 to understand the mechanisms behind this trend.

2.3.2.2 Resistance

For all cases with a fixed fine electrode wire length L, the total initial resistance of the discharge circuit is approximately constant. The resistance of a wire of length l, resistivity ω and cross sectional area A is:

$$Z_{w,l} = \omega \cdot l/A. \tag{2.2}$$

$A = 7.85 \times 10^{-9}$ m^2 and $\omega = 1.70 \times 10^{-8}$ Ω.m at 23.5 °C (Griffiths, 1999). L = 10 mm, 20 mm, 30 mm, 40 mm, and 50 mm for the 0.1 mm diameter electrode wires and $Z_{w,l}$ ranges from 21.9 Ω (for L = 10 mm) to 107 Ω (for L = 50 mm). Using $Z_{w,l}$ for the case of L = 10 mm as a reference, the increase total initial discharge circuit resistance due

to increase in L can be referred to as:

$$Z_A = 2(Z_{w,L} - Z_{w,10mm}). \tag{2.3}$$

The factor of 2 in Equation (2.3) is due to the presence of two electrodes with the same length L used in the experiment.

The results obtained in Section 2.1.2.1 can be plotted as mean maximum bubble radius $\dot{R_{max}}$ against Z_A (Figure 2.25). It is shown that $\dot{R_{max}}$ decreases with increasing Z_A. As an additional validation, resistors of different known values is added to the discharge circuit onto the reference cases of electrodes with L = 10 mm each. This additional resistance is represented by Z_a and four values of Z_a are selected (i.e. 0.10 Ω, 0.15 Ω, 0.20 Ω, 0.25 Ω) by connecting 0.05 Ω and 0.10 Ω power resistors in several arrangements to an electrode terminal. 3 experiments are conducted for each value of Z_a and results are also shown in Figure 2.25. As Z_a increases, the total discharge circuit resistance

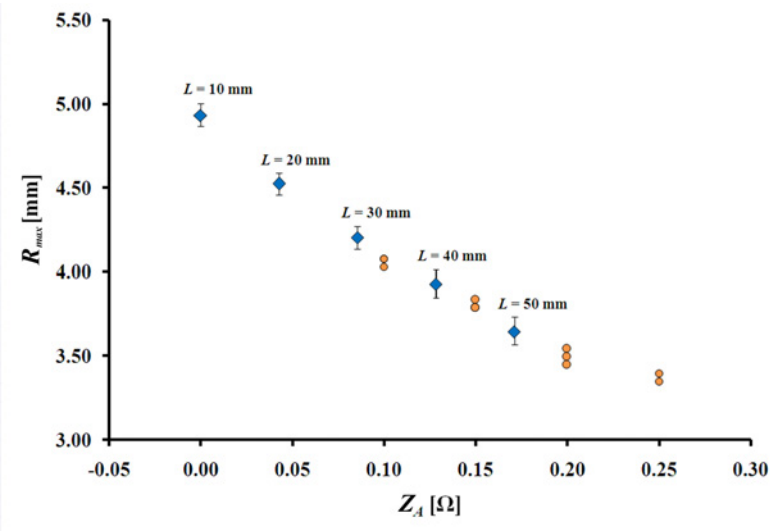

FIGURE 2.25: Graph of maximum spark-generated bubble radius R_{max} against additional discharge circuit resistance Z_A taking the case of L = 10 mm as a reference (Z_A = 0 Ω). The respective length of fine electrode wire L used in the experiment is shown above each data set with a standard deviation bar. Circular data points present in the graph represent cases with various additional resistance Z_A in the discharge circuit, while using L = 10 mm to generate the spark-bubble.

contributing to a decrease in $\dot{R_{max}}$. This trend coincides with the trend obtained with experimental cases due to varying L. Therefore, this verifies that the electrode resistance is a dominant factor in obtaining spark bubbles of varying $\dot{R_{max}}$ in this setup.

We also know that the total amount of energy delivered to the discharge circuit during spark-discharge can be taken as:

$$E_T = \int \frac{V(t)^2}{Z_T(t)} dt. \tag{2.4}$$

where $V(t)$ is the capacitor voltage and $Z_T(t)$ is the discharge circuit resistance. The bubble's potential energy at its maximum radius R_{max} can be estimated as:

$$E_{R_{max}} = \frac{4}{3}\pi p_\infty R_{max}^3. \tag{2.5}$$

where p_∞ is the ambient liquid pressure (Klaseboer and Khoo, 2006). With the assumption of consistent conversion of E_T into $E_{R_{max}}$, an increase in initial discharge circuit resistance will result in a bubble with a smaller R_{max}. This would explain the experimental observations that maximum bubble radius decreases with increasing initial discharge circuit resistance.

2.3.3 Discussion and Conclusion

The generation of consistently-sized spherical cavitation bubbles has been challenging by means of spark-discharge methods. A novel setup has been developed with the aim of repeatedly producing bubbles of predictable sizes. The results are obtained through a spark-discharge electrical setup, which is equipped with a MOSFET switching control to improve consistency in terms of the elimination of contact bounce issue from mechanical

switches and setting a pre-determined discharge time period. This setup also benefits from the use of a low-voltage power source (60.0 V) as opposed to the high-voltage methods (e.g. several kV) which possess inherent dangers in operation. For spark generation, very fine copper wires/electrodes are selected and placed in contact with each other before every experiment. The initial resistance of these electrodes Z_w accounts for a signification portion of the total initial discharge circuit resistance. This has been verified with a marked dependency of the maximum bubble radius R_{max} with Z_A, the additional discharge circuit resistance due to increase in L. As a result, consistent R_{max} (within 2.5% σ) can be obtained by carefully selecting the initial length of the each electrode L. Using a constant 60.0 V source and fine electrode wires with a cross-sectional diameter of 0.10 mm, oscillating bubbles with maximum radius of 3 to 5 mm are obtained. This is an ideal size for bubble dynamics studies using high-speed imaging as it would take approximately 1.3 ms (Figure 2.21) for a typical cavitation bubble to collapse, suggesting that a 25 kfps recording should be sufficient to record the bubble dynamics (a modest requirement for many high-speed cameras, such as the Photron Fastcam SA5 in this study which can go up to 1 Mfps). We also gained a better understanding of such low-voltage spark-discharge methods by monitoring the capacitor voltage during the bubble creation and oscillation. This method is adopted in this study with motivations for cavitation bubble interactions with a neighbouring cell in Section 4.1.

Chapter 3

Numerical Simulations of Cavitation Bubble Interactions

Apart from experimental investigations of cavitation bubble dynamics, numerical simulations of cavitation bubble interactions were also conducted. Computational validation and simulations would allow scientists to gain a deeper understanding of the physics involved in cavitation problems. Two numerical simulation projects that were conducted will be presented in this chapter. The codes used are variations of a Boundary Element formulation of the axi-symmetrical incompressible potential flow theory. This axi-symmetrical numerical method will first be illustrated in the first Section 3.1, followed by a discussion on the two projects numerically investigated. Section 3.2 illustrates the interaction of a cavitation bubble in proximity to a neighbouring quiescent air bubble. Depending on the initial parameters such as distance between the bubbles and their respective characteristic radii, differing interaction patterns can be observed. Section 3.3 is an extension of the study in Section 2.2, which reports the jet orientations of a collapsing bubble near a wall-attached air bubble. With numerical simulations conducted,

we are able to investigate the influence of parameters such as the vapour pressure on the cavitation bubble jet directions. Pressure field plots of selected cases are also conducted to better illustrate this problem. Parts of the results shown in Sections 3.2 & 3.3 have been published in Pain et al. (2012) and Goh et al. (2014b).

3.1 Axi-symmetrical Boundary Element Model for Cavitation Bubble Dynamics

Cavitation bubbles are important for many problems and applications, and they can be found of varying dimensions (from micrometer-sized ultrasound contrast agent bubbles to bubbles of several meters in underwater explosions). Essentially, many phenomena concerning cavitation are inertia controlled, dimensionless numerical studies of such oscillating bubble dynamics based on the potential flow theory can be applied to different disciplines. In this section, an axi-symmetrical Boundary Element formulation for a single cavitation bubble is described. This method has been adapted to investigate the problems discussed in Sections 3.2 & 3.3.

3.1.1 Key Assumptions

The fluid medium in this problem can be assumed as incompressible(Fong, 2007). With this assumption, the continuity equation is reduced to

$$\nabla \cdot \vec{v} = 0, \tag{3.1}$$

where $\vec{v}$ is the velocity vector, and the potential ϕ can be defined as

$$\vec{v} = \nabla\phi, \tag{3.2}$$

assuming irrotational flow. Using the Equations 3.1 & 3.2, the Laplace equation of the velocity potential in a fluid domain takes the form of

$$\nabla^2\phi = 0. \tag{3.3}$$

We now look at the dependency of gravitational and surface tension effects. The Froude number (Fr) represents the ratio between inertia and gravitational forces

$$Fr = \frac{{U_\infty}^2}{gL_c} = \frac{U_\infty}{gt_c}. \tag{3.4}$$

where U_∞ is reference velocity, L_c is the length scale, and g is gravitational acceleration. With t_c as the time scale, L_c can be represented as $U_\infty t_c$. Subsequently, the length scale in this problem is the maximum cavitation bubble radius R_{max} and U_∞ can be represented as $\sqrt{\frac{p_\infty}{\rho}}$, where p_∞ and ρ are the reference pressure (taken as atmospheric pressure of 100 kPa unless otherwise specified) and density of the fluid (= 1000 kg.m^{-3} for water) respectively. Equation 3.4 now becomes

$$Fr = \frac{p_\infty}{\rho g R_{max}} = \mathcal{O}(10^3), \tag{3.5}$$

taking R_{max} = 5 mm, corresponding to approximately the largest cavitation bubble in the present studies, and taking g as 9.81 m.s^{-2}, Fr is greater than 2000, which suggests that gravitational forces are negligible compared to inertia forces (Turangan et al., 2006; Fong, 2007). Similarly, the Weber number (We) represents the ratio of inertia forces

over surface tension, and in our case can be shown as

$$We = \frac{\rho {U_\infty}^2 L_c}{F_s} = \frac{\rho p_\infty R_{max}}{\rho F_s} = \frac{p_\infty R_{max}}{F_s} = \mathcal{O}(10^3), \tag{3.6}$$

where F_s is the surface tension of water (taken as 0.07 N.m^{-1}), and taking R_{max} of 2 mm (the smallest cavitation bubble in the numerical studies). Essentially, surface tension effects can also be neglected (Fong, 2007).

3.1.2 Boundary and Initial Conditions

For an incompressible, inviscid and irrotational flow, the unsteady Bernoulli equation is valid with

$$p = p_\infty - \rho \frac{D\phi}{Dt} + \frac{1}{2}\rho |\vec{v}|^2, \tag{3.7}$$

where ρ is the density of fluid , p is the pressure in the fluid, p_∞ is the reference pressure, t is time and $\frac{D}{Dt}$ is the material derivative which is equal to $\frac{\delta}{\delta t} + \vec{v} \cdot \nabla$. It is notable that for problems in which surface tension, gravitational forces, and/or surface tension effects are important, components of these forces can be added to Equation 3.7.

A spherical cavitation bubble of a certain initial volume V_0 is introduced to the fluid domain. The gas within the bubble is assumed to be uniform and behave adiabatically, thus the gas pressure within the bubble is

$$p_g = p_{g,0}(\frac{V_0}{V})^{\gamma_1}, \tag{3.8}$$

where the subscript '0' denotes the initial values and the volume of the bubble is represented by V. The ratio of specific heats γ_1 is empirically selected to be 1.25 based on an

explosion bubble (Cole, 1948). The total pressure within the bubble is represented as

$$p_b = p_g + p_v = p_{g,0}(\frac{V_0}{V})^{\gamma_1} + p_v, \tag{3.9}$$

where p_v is the vapour pressure. The initial pressure inside the bubble $p_{g,0}$ is chosen as $100(p_\infty - p_v)$ with p_v and V_0 selected such that the cavitation bubble collapse time and maximum radius coincides with the experimental case. The initial condition for the bubble surface is $\phi = 0$ at $t = 0$. Using Equations 3.2, 3.7 & 3.9, and equating the pressure just outside the bubble surface with the pressure in the bubble, $p = p_b$, we obtain the following equation on the bubble's surface.

$$\rho\frac{D\phi}{Dt} = p_\infty + \frac{\rho}{2}|\nabla\phi|^2 - p_{g,0}(\frac{V_0}{V})^{\gamma_1} - p_v. \tag{3.10}$$

3.1.3 Boundary Element Implementation

The free field Green's function is defined as

$$G(\vec{r}, \vec{r_0}) = \frac{1}{|\vec{r_0} - \vec{r}|}, \tag{3.11}$$

where $\vec{r}$ & $\vec{r_0}$ are vectors in the numerical domain, and the subscript '0' means that $\vec{r_0}$ is the reference vector while $\vec{r}$ is the integration variable. Using this, we can transform the Laplace equation of the velocity potential in the fluid domain (Equation 3.3) into a surface integral

$$c(\vec{r_0})\phi(\vec{r_0}) + \int_S \phi(\vec{r})\frac{\delta G(\vec{r_0}, \vec{r})}{\delta \vec{n}}dS = \int_S G(\vec{r_0}, \vec{r})\frac{\delta \phi(\vec{r})}{\delta \vec{n}}dS, \tag{3.12}$$

where S represents the bubble surface, $\frac{\delta}{\delta\vec{n}} = \vec{n} \cdot \nabla$ represents the normal derivative on S, and $c(\vec{r_0})$ is the solid angle on S. $c(\vec{r_0}) = 4\pi$ within the fluid domain but if $\vec{r_0}$ is situated on S, $c(\vec{r_0}) = 2\pi$ if S is smooth at $\vec{r_0}$. Equation 3.12 represents the relationship between the potential $\phi(\vec{r})$ and its normal derivative $\frac{\delta\phi(\vec{r})}{\delta\vec{n}}$ on the surface S. By selecting $\vec{r_0}$ on S, we can obtain either ϕ or $\frac{\delta\phi}{\delta n}$ on S if one is known. Once both are known, the potential anywhere in the numerical domain can be determined by setting $c(\vec{r_0}) = 4\pi$ for any point $\vec{r_0}$ outside of S.

For the axi-symmetrical formulation, we use polar coordinates with $\vec{r_0}$ = (r_0,0,z_0) and $\vec{r}$ = (r,θ,z). Now Equation 3.11 becomes

$$\begin{aligned} G(\vec{r},\vec{r_0}) = \frac{1}{|\vec{r_0}-\vec{r}|} &= \frac{1}{\sqrt{(rcos\theta - r_0)^2 + r^2 sin^2\theta + (z-z_0)^2}} \\ &= \frac{1}{\sqrt{(r+r_0)^2 + (z-z_0)^2 - 4rr_0 cos^2\frac{\theta}{2}}}. \end{aligned} \tag{3.13}$$

The surface S is also parameterized by the variable ξ such that

$$\left.\begin{aligned} r &= r_j + \xi(r_{j+1} - r_j) \\ z &= z_j + \xi(z_{j+1} - z_j) \end{aligned}\right\} \quad 0 \le \xi \le 1. \tag{3.14}$$

Now using $v_n = \frac{\delta\phi}{\delta\vec{n}}$, we obtain

$$\left.\begin{aligned} \phi(\xi) &= (1-\xi)\phi_j + \xi\phi_{j+1} \\ v_n(\xi) &= (1-\xi)v_{n,j} + \xi v_{n,j+1} \end{aligned}\right\} \quad 0 \le \xi \le 1. \tag{3.15}$$

The Jacobian of coordinate transform from (r,z) to (ξ) is defined as

$$Ja = \sqrt{(\frac{dz}{d\xi})^2 + (\frac{dr}{d\xi})^2}. \tag{3.16}$$

The two integrals in Equation 3.12 can now be represented as a summation of integrals over individual elements represented by 'k'

$$\int_S \phi(\vec{r})\frac{\delta G(\vec{r_0},\vec{r})}{\delta \vec{n}}dS = \sum_{k=1}^{N-1}\int_{S_k} \phi(\vec{r})\frac{\delta G(\vec{r_0},\vec{r})}{\delta \vec{n}}dS, \tag{3.17}$$

$$\int_S G(\vec{r_0},\vec{r})\frac{\delta \phi(\vec{r})}{\delta \vec{n}}dS = \sum_{k=1}^{N-1}\int_{S_k} G(\vec{r_0},\vec{r})v_n(\vec{r})dS. \tag{3.18}$$

With ξ, the integrals over one element 'k' for Equations 3.17 & 3.18 become

$$\begin{aligned}\int_{S_k} \phi(\vec{r})\frac{\delta G(\vec{r_0},\vec{r})}{\delta \vec{n}}dS &= \phi_j(\vec{r})\int_0^1 (1-\xi)r(\xi)Ja\int_0^{2\pi}\vec{n}\cdot\nabla\frac{1}{|\vec{r_0}-\vec{r}|}d\theta d\xi \\ &\quad + \phi_{j+1}(\vec{r})\int_0^1 \xi r(\xi)Ja\int_0^{2\pi}\vec{n}\cdot\nabla\frac{1}{|\vec{r_0}-\vec{r}|}d\theta d\xi \\ &= \phi_j A_1 + \phi_{j+1}A_2,\end{aligned} \tag{3.19}$$

$$\begin{aligned}\int_{S_k} G(\vec{r_0},\vec{r})v_n(\vec{r})dS &= v_{n,j}(\vec{r})\int_0^1 (1-\xi)r(\xi)Ja\int_0^{2\pi}\frac{1}{\vec{r_0}-\vec{r}}d\theta d\xi \\ &\quad + v_{n,j+1}(\vec{r})\int_0^1 \xi r(\xi)Ja\int_0^{2\pi}\frac{1}{\vec{r_0}-\vec{r}}d\theta d\xi \\ &= v_{n,j}(\vec{r})B_1 + v_{n,j+1}(\vec{r})B_2.\end{aligned} \tag{3.20}$$

We can now perform the integrations in Equation 3.12 with a linear representation of the potential and the normal velocity as described in Wang et al. (1996a,b); Klaseboer and Khoo (2004a). This results in a system of equations of size N x N

$$\mathbf{G}\cdot v_n = \mathbf{H}\cdot\phi \tag{3.21}$$

with influence matrixes **G** and **H**. The terms inside the influence matrixes are influence coefficients and they only depend on the geometry of the problem and not on ϕ and its derivatives. The diagonal elements of matrix **H** should include the $c(\vec{r_0})$ coefficient. However, the volume within the surface S (internal problem) has a constant potential ϕ,

thus $v_n = 0$ everywhere on the boundary S. The sum of solid angles for the internal and external problem should be 4π and since the normal vector $\vec{n}$ for the internal problem is exactly directed opposite to that of the external problem, $H_{i,j} = -H_{i,j}^{internal}$. As such, the diagonal elements of matrix **H** can now be replaced with

$$H_{ii} = 4\pi - \sum_{j \neq i}^{N} H_{ij}, \tag{3.22}$$

eliminating the need to compute the solid angle in Equation 3.21. We can then determine the unknown normal velocity v_n at each node using Gaussian Elimination. The potential distribution along the surface of the bubble is used to determine the tangential velocity v_t. Consequently, the velocity vector $\vec{v}$ (Equation 3.2) is found and we can obtain the potential distribution of the nodes at the next time step for the cavitation bubble using the Bernoulli Equation 3.10. The position vector of the nodes on the bubble surface can also be updated for each time step since $\vec{v} = \frac{D\vec{r}}{Dt}$.

Figure 3.1 shows the surface of the cavitation bubble that is represented by N_1 nodes arranged in a semi-circle for this axi-symmetrical implementation, with $N_1 = 51$ for all cases simulated. If there is a neighbouring boundary or bubble etc., an additional N_2 number of nodes can be added to the system which gives a total of $N = N_1 + N_2$.

An adaptive time step is chosen based on the Bernoulli equation

$$\Delta t = \frac{0.02}{max||p_\infty| + p_g + \frac{\rho}{2}|\nabla\phi|^2|}, \tag{3.23}$$

to find the minimum Δt across all nodes and applied to problems which may encounter numerical instability. Otherwise, a constant time step can also be chosen for numerical implementation. A smoothing scheme for nodes redistribution is performed every 10

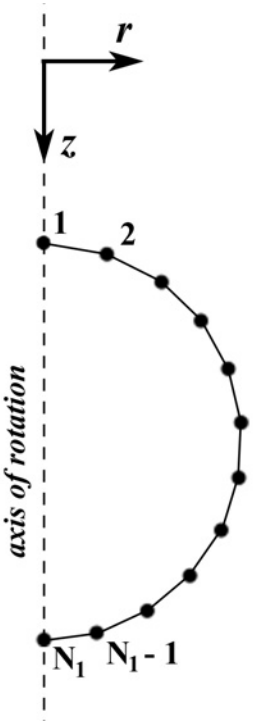

FIGURE 3.1: Linear mesh of a cavitation bubble surrounded by a fluid comprising of N_1 nodes. The node numbering is clockwise with the node number '1' on top and the node number 'N_1' at the bottom of the image.

time steps to prevent numerical surface instabilities (Klaseboer and Khoo, 2004b).

3.2 Quiescent bubble jet caused by a nearby oscillating bubble

The first numerical study presented here is that of the interaction between a cavitation bubble and an initially quiescent air bubble in vicinity. This is important because bubbles do not typically exist in isolation thus it is vital to understand the dynamics involved in a problem like this. Studies of multiple oscillating bubble systems have reported bubble collapsing jets towards or away from each other, and the phase difference is an important parameter that affects the directions of these jets (Fong et al., 2009; Chew et al., 2011). However, this study focuses on the interaction of a cavitation and a nearby initially stable (non-oscillating) bubble, and differs from the above studies of

multiple cavitation bubbles in proximity. Xu et al. (2010) investigated the interactions between an oscillating bubble and an air bubble near a rigid boundary and found that cavitation bubble may collapse with a jet direction in different directions depending on the positions of the bubbles in this system. The behaviour of a cavitation bubble near to a quiescent bubble, away from other boundaries has not been studied. Stable bubbles are more common and one interesting example is the lipid-coated microbubble. These bubbles when combined with cavitation mechanisms have tremendous potential in diagnostic and therapeutic applications such as drug delivery (Unger et al., 2004; Qin et al., 2009) in which the targeted liquid jets or concentrated pressure waves from the bubble(s) collapse could permeabilize neighbouring cell membranes and disrupt drug-carrying vesicles.

Parts of the results in this section have been published under Pain et al. (2012). The interaction between a cavitation bubble and a nearby equilibrium bubble is found to create a jet which exits the stationary bubble in the direction away from the cavitation bubble. This jet is predicted to reach great velocity and could have an effect on neighbouring structures. Therefore, it is of interest to evaluate on the conditions which could prevent the occurrence of such a jet or minimize its effect. For the purpose of discussion, the numerical studies performed based on the numerical setup presented in 3.1 with some variations discussed below will be highlighted.

3.2.1 Numerical Setup

An axi-symmetrical boundary element method (BEM) model is used in the simulations of the interactions between an oscillating bubble and an initially stationary gas bubble. Figure 3.2 shows the primary parameters used in this study, in which R_a, R_{max}, and D refers to the initial air bubble radius, cavitation bubble maximum radius, and the

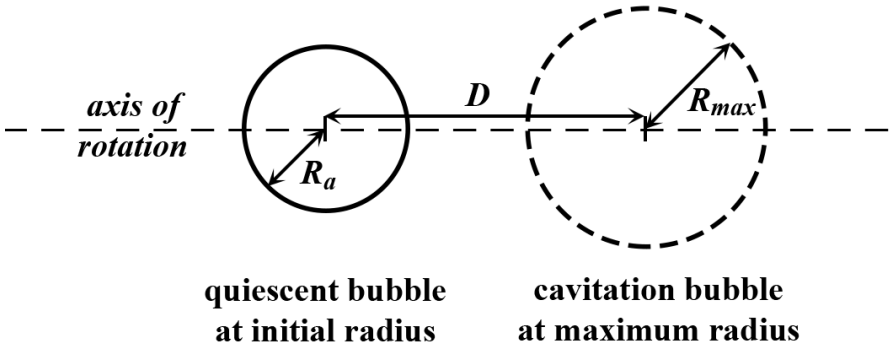

FIGURE 3.2: Primary parameters of the problem, showing a cavitation bubble at its maximum radius R_{max} next to a quiescent air bubble at its initial radius R_a. The initial distance between the two bubbles is denoted as D. The horizontal axis of rotation for the axi-symmetrical BEM implementation is shown.

distance between the centre of the two bubbles, respectively. Details of the BEM formulation for the cavitation bubble have been given in Section 3.1. However, please note that this problem now comprises of a neighbouring quiescent air bubble. The quiescent air bubble is modelled as a spherical gas bubble with an initial internal pressure of $p_{a,0}$ = 100 kPa. The pressure within the air bubble p_a is also assumed to be uniform and adiabatic, thus following

$$p_a = p_{a,0}(\frac{V_{a,0}}{V_a})^{\gamma_2}, \tag{3.24}$$

where $V_{a,0}$ and V_a represent the initial and instantaneous volume of the air bubble respectively. γ_2 represents the ratio of specific heats for air, which is 1.40. As a result, the Bernoulli equation on the quiescent bubble surface takes the form of

$$\rho\frac{D\phi}{Dt} = p_\infty + \frac{\rho}{2}|\nabla\phi|^2 - p_{a,0}(\frac{V_{a,0}}{V_a})^{\gamma_2}. \tag{3.25}$$

The quiescent air bubble is discretized into 51 nodes with the axi-symmetrical formulation which is similar for the cavitation bubble (Equation 3.10). We can now solve for the unknown normal velocity at each node and update its position with time using

Equation 3.12. From the dimensionless analysis of parameters in numerical simulations of cavitation bubble dynamics Turangan et al. (2006), the main dimensionless parameters in this problem are time $t' = \frac{t}{R_{max}}\sqrt{\frac{p_\infty - p_v}{\rho}}$, velocity $u' = u\sqrt{\frac{\rho}{p_\infty - p_v}}$ and the two dimensionless distances $D' = \frac{D}{R_{max}}$ and ${R_a}' = \frac{R_a}{R_{max}}$.

R_{max} and R_a relates to the maximum cavitation bubble radius and the initial air bubble radius respectively. The quiescent air bubble in this section is assumed to take a spherical shape initially, which is not to be confused with the R_e in 2.2 that refers to the equilibrium radius of the initial air bubble attached to the wall. ${R_a}'$ represents the bubble size ratio of the initial air bubble radius and the maximum cavitation bubble radius. D is also a new parameter as it defines the initial between a quiescent spherical air bubble and the cavitation bubble. D' represents the dimensionless initial distance between the bubbles and it gives a relative measure of how near the cavitation bubble is generated to the quiescent bubble. The dimensionless time parameter t' is presented to allow the numerical results to be applied across problems of various scale, as long as the assumptions in this study (such as inertial-controlled) are valid. The liquid jet velocity u_j is of special interest to this study as it provides a basic measure of how drastic the induced liquid jet exiting the air bubble could be to neighbouring surface(s). Starting from the dimensionless liquid jet velocity ${u_j}'$, the actual liquid jet velocity u_j does not depend on the length scale of the problem (maximum radius of the oscillating bubble). As such, no matter how large the maximum oscillating bubble radius is, the actual liquid jet velocity will still be only dependent on ρ, p_∞, and p_v when scaling from dimensionless to dimensional. p_v is assumed as 0 kPa for all simulations, except for the cases in comparison with spark-bubble experiments (Figures 3.3 & 3.4) in which p_v is chosen as 47 kPa, after iterating different values of p_v (rounded to closest 1 kPa) until the predicted collapse (first minimum volume) timing of the cavitation bubble has the

smallest difference to the experimental collapse timing of the spark-bubble.

3.2.2 Results

Numerical simulations of cases with varying D' and ${R_a}'$ were conducted. It is noticed that depending on the input parameters, a liquid jet could be induced in the quiescent air bubble by the neighbouring cavitation bubble. It may develop and penetrate the air bubble wall directed away from the neighbouring cavitation bubble. As this liquid jet may reach high velocities and affect structures in proximity, the velocity of this jet at the point of exit on the air bubble wall for different D' and ${R_a}'$ is computed. Two typical cases with experimental validation, followed by a comprehensive evaluation of the main parameters are shown in the subsections below.

3.2.2.1 Typical cases and experimental validation

Two numerical cases are presented here to show the typical interactions between the cavitation bubble and quiescent bubble. Parameters from these cases are obtained from experiments, and the simulations are compared with the experimental results for validation of the code. The experiments are conducted using a low voltage spark-generated bubble method to generate the cavitation bubble, similar to that in Sections 2.1 & 2.2. Silicone oil is used to 'trap' an air bubble of initial radius R_a around 1 mm on one of the electrode wires used to generate the spark. The spark-generated cavitation bubble reaches a maximum radius R_{max} of around 5 mm and its interaction with the neighbouring air bubble is being captured using a high-speed imaging setup. More details of this experimental method can be found in Pain et al. (2012).

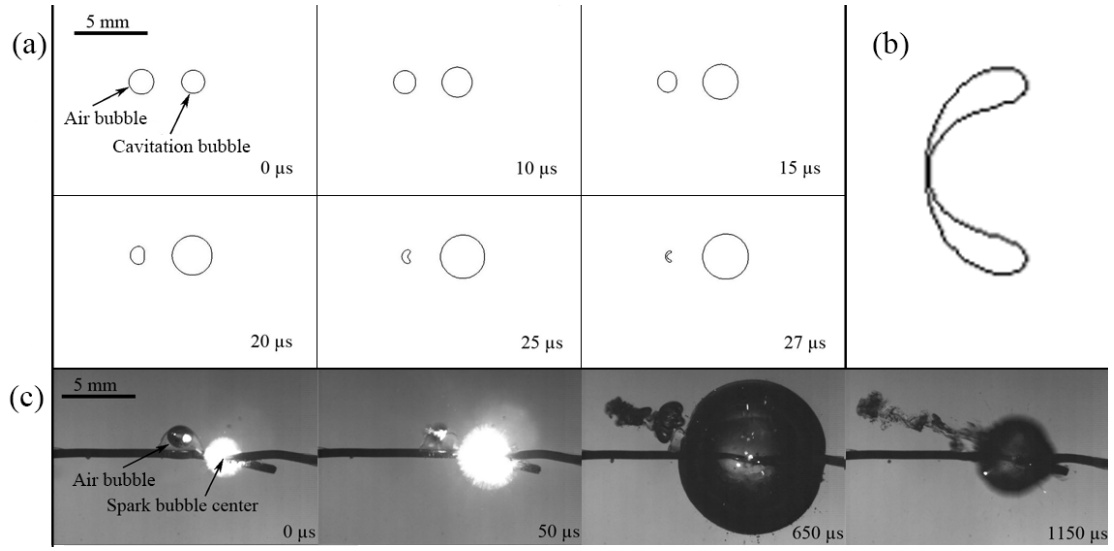

FIGURE 3.3: Case of quiescent bubble ($R_a = 0.84$ mm) at $D = 3.43$ mm away from a cavitation bubble ($R_{max} = 5.15$ mm) initially, giving $R_a{}' = 0.16$ & $D' = 0.67$. A liquid jet develops and penetrates the air bubble wall, directed away from the cavitation bubble. (a) The top frames show the numerical simulations at during the cavitation bubble oscillation, and (b) on the right of the set is an insert showing the enlarged view of the air bubble jet from the frame at $t = 27$ μs. (c) The bottom frames show the corresponding experimental images (Pain et al., 2012). A 5 mm scale bar is shown on the top left hand corner of each set, and the corresponding timings t of each frame is shown on the bottom right hand corner.

Figure 3.3 shows the first case of a cavitation bubble oscillation beside an initially stationary air bubble with the parameters $R_a = 0.84$ mm for the air bubble, $D = 3.43$ mm between the two bubbles initially, and $R_{max} = 5.15$ mm for the cavitation bubble. The top portion of the figure shows the numerical simulation results and the bottom image set comprises of high-speed camera images from the experiments (Pain et al., 2012). The timings t are shown at the bottom right hand corner of each frame and a 5 mm scale bar in the top left hand corner of the frames at $t = 0$ μs. From the numerical simulations, the air bubble is compressed on its side closer to the expanding cavitation bubble, for t up to 20 μs. This compressed bubble wall develops into a liquid jet directed away from the cavitation bubble, as shown at $t = 25$ μs. This jet comes into contact with the air bubble surface on the left hand side of the frame at $t = 27$ μs, which can be better seen as an expanded view insert on the top right hand side of Figure 3.3. The jet velocity u_j is defined as the velocity of this liquid jet at this instant (time it comes

into contact with the air bubble surface). u_j in this case is calculated to be 124 m.s^{-1} from the simulations. From the experimental results shown (performed by Ms. Agnes Paín), the first frame ($t = 0$ μs) shows an air bubble held in place by encapsulating it in a silicone oil droplet, and a bright region labelled 'Spark bubble centre' shows the electrical spark discharge which will develop into a cavitation bubble. The expanding spark bubble almost instantaneously creates a jet through the air bubble in the direction away from the cavitation bubble. It is clear that this jet has emerged from the stationary bubble surface at $t = 50$ μs. The spark bubble expands to its maximum radius R_{max} at $t = 650$ μs. It is shown at $t = 1150$ μs that the collapsed air bubble clouds continue to move away from the collapsing cavitation bubble, in the direction of the liquid jet. Essentially, the numerical simulations seem to predict interactions between the two bubbles as seen with the experimental images. The numerical simulations also complement the experimental data in two key aspects for this case: predict the bubble shapes during the initial timings, i.e. between 0 μ and 50 μs (for which experimental high-speed imaging are limited in this case) and compute the liquid jet velocity at the instant of jet impact with air bubble surface.

Figure 3.4 shows the second case of a single cavitation bubble interaction with a neighbouring quiescent air bubble. Similarly, the top half of the figure shows the numerical simulation results whereas the bottom half is an image set obtained from an high-speed imaging experiment (Pain et al., 2012). The parameters used in this case are $R_a = 0.96$ mm, $D = 10.01$ mm, $R_{max} = 4.81$ mm, hence giving a comparable $R_a{}' = 0.20$ and much greater $D' = 2.08$ with respect to the previous case (Figure 3.3). It is predicted from the numerical simulations that the cavitation bubble expands rapidly to its maximum radius R_{max} at $t = 750$ μs and then collapses. While the cavitation bubble is expanding, the air bubble shows a developing jet directed away from the cavitation bubble at $t =$

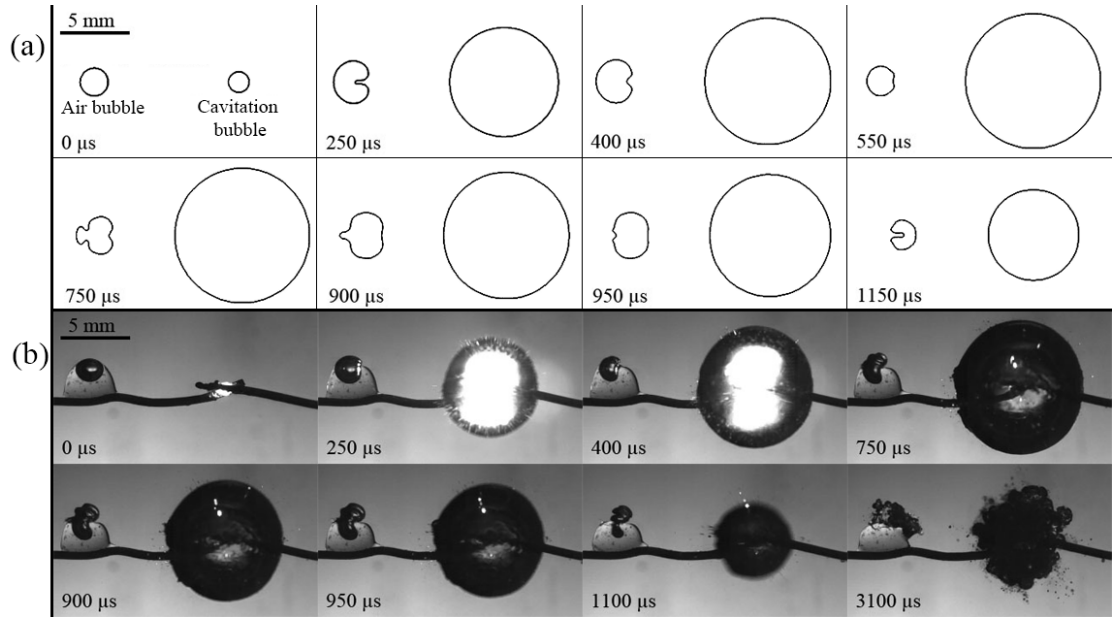

FIGURE 3.4: Case of quiescent bubble ($R_a = 0.96$ mm) at $D = 10.01$ mm away from a cavitation bubble ($R_{max} = 4.81$ mm) initially, hence ${R_a}' = 0.20$ & $D' = 2.08$. A developing jet within the air bubble can be seen but the it does not end up penetrating the air bubble surface it traverses towards. (a) The top frames show the numerical simulations at during the cavitation bubble oscillation, and (b) the bottom frames show the corresponding experimental images (Pain et al., 2012). A 5 mm scale bar is shown on the top left hand corner of each set, and the corresponding timings t of each frame is shown on the bottom left hand corner.

250 μs. However as the cavitation bubble expands, the air bubble undergoes volume oscillation itself and this jet recedes in the direction towards the cavitation bubble ($t =$ 400 & 550 μs). The air bubble is predicted to pinch off into a peculiar protrusion on its left hand side, shown at $t = 750$ & 900 μs. This bubble protrusion then develops into an interior liquid jet towards the cavitation bubble as the cavitation bubble contracts in size ($t = 950$ & 1150 μs). As the developing liquid jet on the air bubble at $t = 250$ μs did not eventually come into contact with the bubble surface on the left-hand side, this case would be classified as having a velocity of $u_j = 0$ m.s^{-1}. The experimental images on the bottom show a very good agreement to the numerical simulations. The expanding spark-generated cavitation bubble creates an impending jet which also does not penetrate the air bubble. The peculiar air bubble protrusion can also be seen at $t =$ 900 & 950 μs. After the cavitation bubble collapses at 3100 μs, the air bubble is seen to

disintegrate into smaller bubbles, without any apparent jet(s) towards the left-hand side unlike the previous example. It appears that the increase in initial dimensionless distance between the two bubbles can negate the induced jet penetration of the air bubble wall.

The two cases above provide a validation of the numerical code. The cases are representative cases as a penetrating jet is formed in one case and in the other case it is absent. In the next Section 3.2.2.2, a systematic study using different $R_a{}'$ and D' will be conducted to have a better understanding of this problem and study the influence of the key parameters.

3.2.2.2 Liquid jet velocity dependency on D' and $R_a{}'$

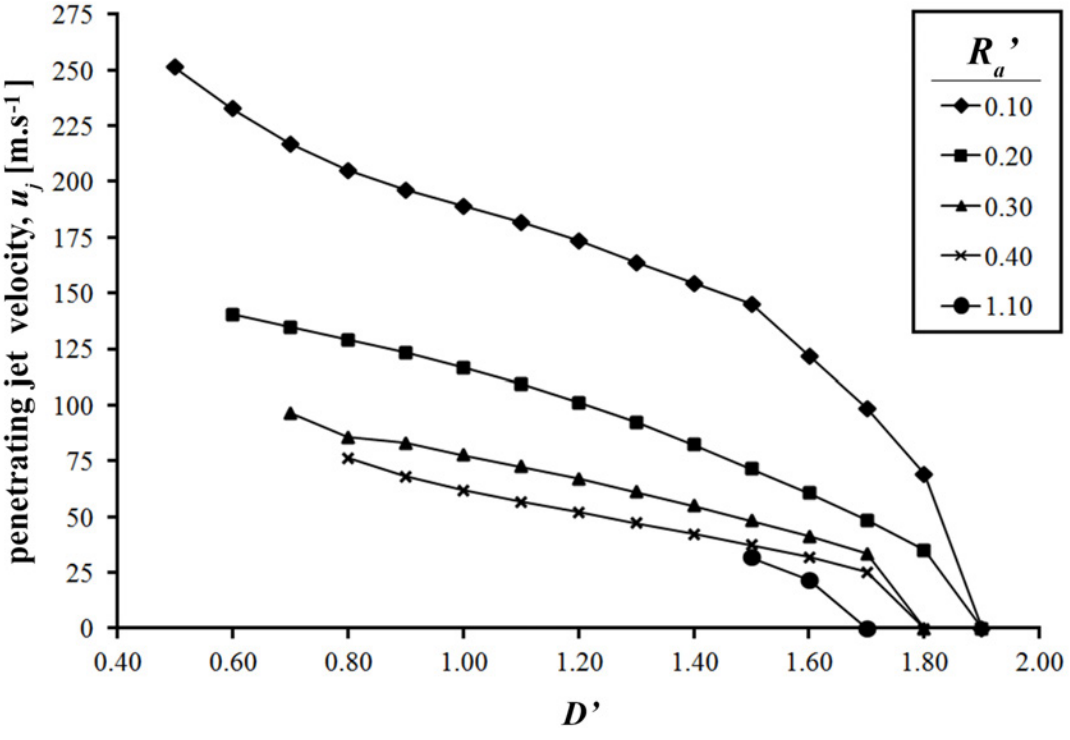

FIGURE 3.5: Graph of liquid jet velocity on the air bubble as it contacts the bubble surface away from the cavitation bubble u_j against initial dimensionless distance between the bubbles D' for various bubble size ratios $R_a{}'$.

Numerical simulations are conducted for different bubble size ratios $R_a{}'$ and initial dimensionless separation between the bubbles D'. Figure 3.5 shows a summary of the velocity of the liquid jet in the air bubble directed away from the cavitation bubble as it penetrates the air bubble surface u_j obtained for $D' > 0.40$ and $R_a{}' > 0.10$, in steps of 0.10 for both D' and $R_a{}'$. The jet velocities are plotted in m/s and not dimensionless as they do not depend on the length scale of the problem R_{max}, as mentioned in the numerical setup 3.2.1. A penetrating jet in the air bubble directed away from the cavitation bubble is present for cases with $D' < 1.90$. For cases of $D' \geq 1.90$, the liquid jet in the air bubble directed away from the cavitation bubble is either absent or does not come into contact with (or penetrate) the air bubble surface. Small values of D' (≤ 0.4) might result in coalescence of the bubbles instead of developing a jet hence are neglected in this discussion. For the cases in which a penetrating liquid jet is present, u_j decreases with D' at any given $R_a{}'$. This is intuitive as the liquid jet is primarily developed due to the rapid expansion of the neighbouring cavitation bubble, hence a smaller D' suggests a higher effect of the cavitation bubble expansion on the air bubble and consequently the jet velocity u_j. The penetrating jet is only present for $R_a{}' \leq 1.10$. This means that if the initial air bubble radius R_a is more than 110% of the maximum cavitation bubble radius R_{max}, a penetrating jet is no longer predicted, regardless of the initial distance between the bubbles. For cases with a penetrating jet, the jet velocity u_j decreases with increasing $R_a{}'$ a constant D'. For example, for bubbles at $D' = 1.00$, the jet velocity u_j for $R_a{}' = 0.10$ is 189 m.s^{-1}, but decreases to 62 m.s^{-1} for $R_a{}' = 0.40$. One possible explanation is that the induced jet in a larger bubble would traverse a larger distance as compared to a smaller bubble before exiting, hence resulting in a loss of kinetic energy and correspondingly the velocity. It can also be noticed that there are minimal disturbances to the cavitation bubble oscillation for small values of $R_a{}'$

(≤ 0.30), and the cavitation bubble collapses spherically. Gathering the trend of both parameters, the maximum jet velocity is predicted for the case of smallest $R_a{}'$ and D', i.e. $u_j = 251$ m.s^{-1} for $R_a{}' = 0.10$ and $D' = 0.50$.

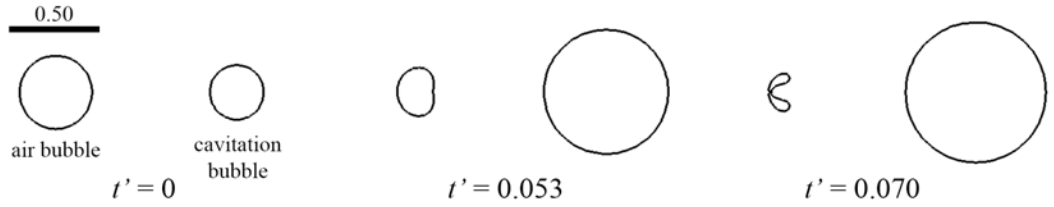

FIGURE 3.6: Case of $D' = 1.00$, $R_a{}' = 0.20$. The respective dimensionless timings are shown at the bottom of each frame and a 0.50 scale bar is shown in the first frame.

To have a better understanding of the physical differences of the different cases conducted, three of these cases have been selected and their results are presented below for comparison. The results from these cases are presented as Figures 3.6, 3.7 & 3.8, using parameters of $D' = 1.00$, $R_a{}' = 0.20$; $D' = 3.00$, $R_a{}' = 0.20$; $D' = 1.00$, $R_a{}' = 0.70$ respectively. In the first case of Figure 3.6, the bubble size ratio $R_a{}' = 0.20$ and the initial dimensionless separation $D' = 1.00$. As the cavitation bubble rapidly expands, the air bubble wall closer to the cavitation bubble is clearly compressed, as shown at t' = 0.053. At $t' = 0.070$, there is a clear penetrating jet in the air bubble away from the expanding cavitation bubble.

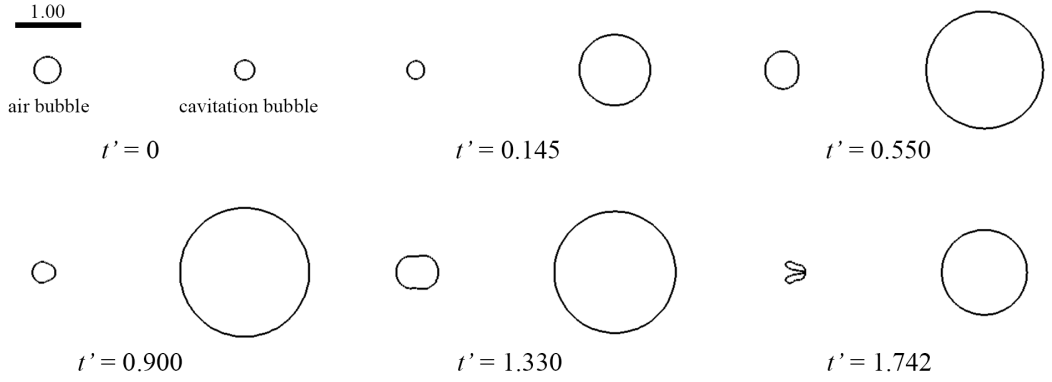

FIGURE 3.7: Case of $D' = 3.00$, $R_a{}' = 0.20$.The respective dimensionless timings are shown at the bottom of each frame and a 1.00 scale bar is shown in the first frame.

When the initial separation between the air bubble and cavitation bubble is greatly increased (to 300% that of Figure 3.6, i.e. $D' = 3.00$), it should result in the absence of a penetrating air bubble liquid jet away from the cavitation bubble. Figure 3.7 shows such a case. In the previous example, the rapidly expanding cavitation bubble has a direct effect on the neighbouring air bubble shape oscillation, which results in a jet directed to the left. However, in this case, The air bubble shrinks almost spherically to its first minimum volume at $t' = 0.145$ during the cavitation bubble expansion. The air bubble continues to undergo two more cycles of oscillations, going from maximum volume ($t' = 0.550$) to minimum volume ($t' = 0.900$), and back again ($t' = 1.330$). At around $t' = 1.00$, the cavitation bubble reaches its maximum volume and begins its contraction phase. The air bubble is then predicted to collapse towards the shrinking air bubble at $t' = 1.742$ with a liquid jet directed towards the shrinking cavitation bubble.

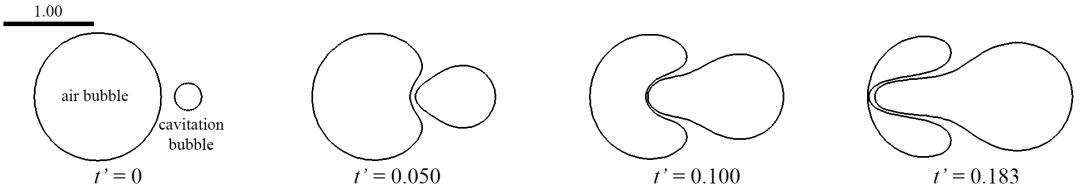

FIGURE 3.8: Case of $D' = 1.00$, $R_a{}' = 1.00$. The respective dimensionless timings are shown at the bottom of each frame and a 1.00 scale bar is shown in the first frame.

Figure 3.8 shows the final case, which has an increased $R_a{}'$ (now = 1.00) as compared to the case of Figure 3.6, but D' remains as 1.00. It is noticeable that the cavitation bubble is created very close to the air bubble wall. This is the limiting case of increasing $R_a{}'$ for $D' = 1.00$ before bubble coalescence takes place without any penetrating jets. This is also the reason why the minimum D' values increases for increasing $R_a{}'$ in Figure 3.5. As the cavitation bubble expands, its is shape is limited by the air bubble just adjacent to it. This results in the shape shown at $t' = 0.050$, in which a depression is seen in the contracting air bubble and a pointed tip on the expanding cavitation bubble 'pushing' into the air bubble. A thin film of liquid lies between this area between the two bubbles

and the cavitation bubble continues to propagate towards the air bubble, forming a liquid jet to the left, as shown at $t = 0.100$. At $t' = 0.183$, this liquid jet finally penetrates the air bubble wall on the left at $u_j = 61.3$ m.s^{-1}.

3.2.3 Discussion and Conclusion

The interaction between a cavitation bubble and a neighbouring quiescent air bubble has been described using an axi-symmetrical BEM numerical model. Two typical examples will first be presented, which show the presence (and absence) of a liquid jet that penetrates the air bubble in the direction away from the cavitation bubble. Parameters of these two cases are taken to be identical to actual spark-discharge experiments for comparison, and it was shown that the numerical method can correctly capture the physics of the problem based on the interactions between the bubbles. It was predicted that the two main dimensionless parameters governing the creation of the penetrating liquid jet and its subsequent velocity u_j are the bubble size ratio ${R_a}'$ and dimensionless initial distance between the bubbles D'. It is possible to predict the occurrence of this liquid jet and its velocity from simulations with varying values of ${R_a}'$ and D'. From the results, it appears that $D' < 1.9$ is a minimum requirement for the appearance of a penetrating jet through the air bubble away from the cavitation bubble. No such jets were predicted numerically for $D' \geq 1.9$ regardless of the bubble size ratio ${R_a}'$. The results in Figure 3.5 also show that the penetrating liquid jet velocity increases for decreasing D' and/or ${R_a}'$. For ${R_a}' \geq 1.20$, the cavitation bubble no longer appears to be able to induce a liquid jet capable of penetrating the air bubble. These two conditions ($D' < 1.9$ and/or ${R_a}' < 1.20$) essentially allow us to have a prediction on the occurrence of jets through the initially stationary air bubble which is of interest in this study, and the respective jet velocities (if the jet is present). The results presented here highlight the importance of

a thorough understanding of cavitation bubble dynamics beside a bubble in vicinity as liquid jets reaching great velocities may be present and could cause collateral damage on tissues. Alternatively, this fine liquid jet could also be utilized for micro-bubble drug delivery (Liang et al., 2010; Hernot and Klibanov, 2008; Wu and Nyborg, 2008).

3.3 Jet orientation of a collapsing bubble near a solid wall with an attached air bubble

The second numerical study to be discussed is the interaction between a cavitation bubble and a neighbouring wall-attached quiescent air bubble. This is an extension of the experimental work on this problem discussed in Section 2.2. Some of the results in this Section have also been published in Goh et al. (2014b). As it is shown with spark-discharge experiments (Section 2.2), the cavitation bubble may collapse with liquid jet(s) in different directions depending on the experimental parameters. The key parameters of this problem were found to be the dimensionless cavitation bubble oscillation time T' and the dimensionless stand-off distance H'. To gain a better understanding of the physics involved in this problem, the axi-symmetrical BEM model is employed.

3.3.1 Numerical Setup

An axi-symmetrical boundary element method is used to simulate the interactions between an oscillating bubble and an initially stationary wall-attached hemispherical air bubble. This is achieved with the numerical setup shown in Figure 3.9 (page 83), with the axis of rotation along the line $r = 0$, joining the centres of the bubbles. This system is exactly similar to the previous study (Section 3.2), except for the inclusion of a cavitation bubble image directly opposite of the cavitation bubble about $z = 0$. The centre

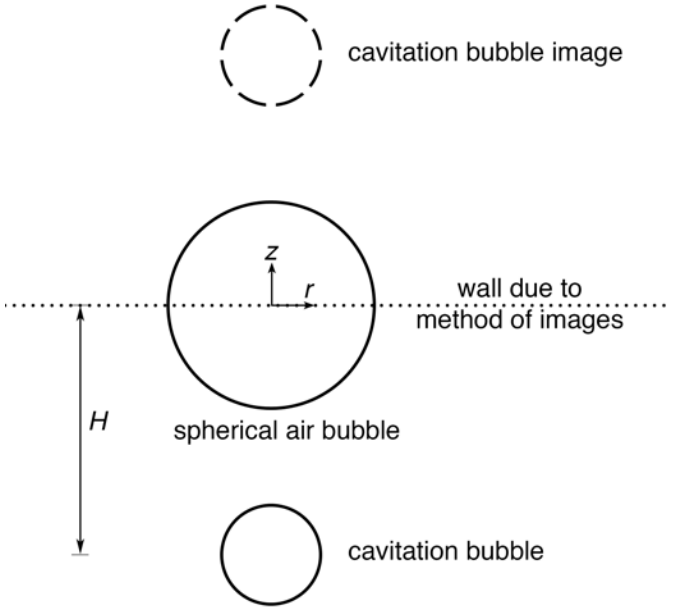

FIGURE 3.9: Numerical setup and coordinate system of a cavitation bubble near to a wall-attached initially stationary hemispherical air bubble. The cavitation bubble at the top of the image is a reflection of the cavitation bubble at the bottom about the plane $z = 0$. An initially spherical air bubble is modelled with its centre at coordinates $z = 0$; $r = 0$. Due to the method of images, the top half of the air bubble can be taken as a reflected image of its bottom half. The dotted line ($z = 0$) thus represents a rigid wall with an attached hemispherical air bubble. The axis of rotation for the axi-symmetrical method is along the line $r = 0$.

of the air bubble is initially separated from the cavitation bubble and this image at a distance represented by H, the stand-off distance. This results in a three-bubble system in line, with a quiescent air bubble in between two cavitation bubbles with identical growth and collapse. Due to the method of images, such a setup essentially represents this problem, i.e. a cavitation bubble growth and collapse near to a quiescent hemispherical wall-attached air bubble, as the horizontal line of symmetry ($z = 0$) is representative of a rigid wall. The implementation of the numerical code is almost identical to that of Section 3.2, but now when we consolidate the influence matrixes (Equation 3.21), we add in the contributions from the cavitation bubble image. As the influence coefficients are only dependent on the geometry of the problem, the influence coefficients of the cavitation bubble image are easily obtained using the cavitation bubble nodes with identical r values but -z values, i.e. reflected about $z = 0$. The initial pressure

within the air bubble is taken at atmospheric pressure (100 kPa). The time dependent pressure within the cavitation bubble and air bubble are assumed to be uniform and adiabatic, hence following Equations 3.9 & 3.24 respectively. The unsteady Bernoulli equation (Equation 3.7) allows us to obtain the pressure p at any fixed point outside of the bubbles. This is utilized to derive pressure contour plots outside of the bubbles during the oscillation to study the pressure distribution patterns.

As defined in the experimental study of this problem (Figure 2.7), the initial air bubble radius is represented by R_e, the maximum cavitation bubble radius is R_{max}, and the vapour pressure is presented as p_v. The dimensionless initial stand-off distance H' is defined as $\frac{H}{R_{max}}$.

3.3.2 Results

The key results to study are the parameters that depict the change in direction of the cavitation bubble collapse jet as shown experimentally in Section 2.2. The jet direction shows a dependency on the bubble phase difference represented by T', which appears to be correlated to vapour pressure p_v values of the spark-discharge cavitation bubbles in the experiments. As we are unable to control the values of p_v in the spark-discharge experiments, numerical simulations now become an invaluable tool to investigate the results' dependency of this parameter. Also as a validation for the simulations, the experimental results of the three cases with different collapse jet directions (similar H' but different T', Figure 2.16) are chosen for comparison in the following subsections.

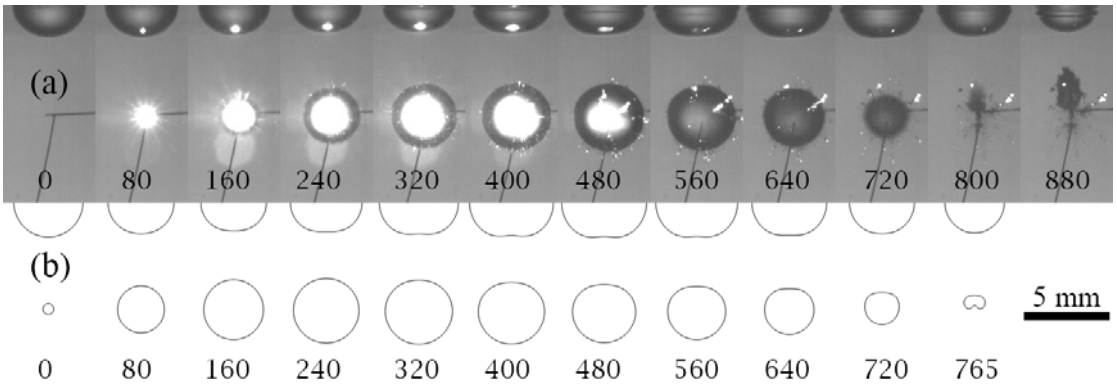

FIGURE 3.10: Case of cavitation bubble collapse jet towards rigid wall ($R_e = 2.05$ mm, $R_{max} = 2.01$ mm, $H' = 3.17$, $p_v = 65$ kPa). The top row of images (a) is adapted from the experiments, Figure 2.16(a), and the bottom row of images (b) shows corresponding numerical simulations. The respective timing of each frame is shown at the bottom of the image, and a 5 mm scale bar is shown at the bottom right hand corner.

3.3.2.1 Numerical Simulations

The first case shown in Figure 3.10 are numerical simulations with parameters that correspond to the case presented as Figure 2.16(a). $R_e = 2.05$ mm, $R_{max} = 2.01$ mm, H' = 3.17, and p_v is chosen as 65 kPa to match the experimental cavitation bubble collapse time T. The experimental results are reproduced above the numerical simulations for comparison, both showing a cavitation bubble expanding and collapsing with a liquid jet directed towards the initially hemispherical air bubble attached to a rigid wall. We can see from the numerical simulations that the cavitation bubble expands to its maximum size at around 320 μs, before that in the experiments of around 480 μs. The cavitation bubble then collapses just after 765 μs, with a liquid jet towards the wall-attached air bubble. The numerical simulations display a very good fit to the experimental images of this problem with similar expansion and collapse shapes on both bubbles. However, there is no noticeable experimental surface perturbations on the air bubble surface in the simulations. This could be due to the image-method setup used in the simulations which does not account for the physics of the bubble-boundary contact line and shockwaves from the expanding cavitation bubble reflected at the rigid boundary. Nevertheless, it

does appear that the basic mechanisms of this case (bubble oscillations and liquid jet formation) are captured to a good degree.

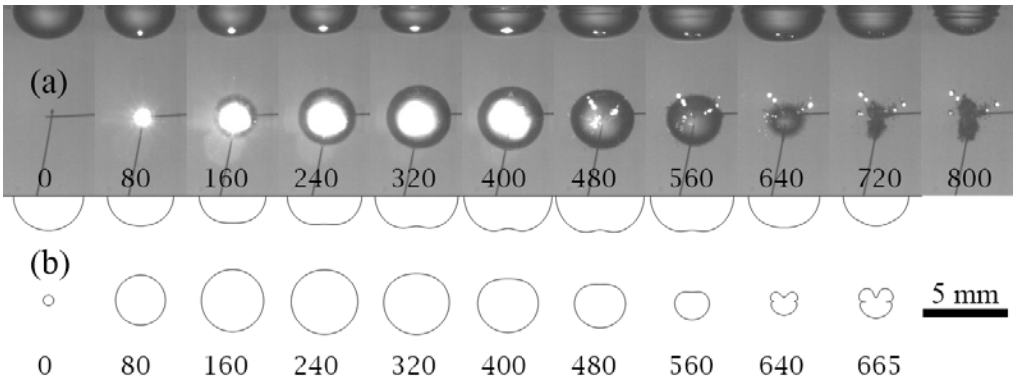

FIGURE 3.11: Case of cavitation bubble collapse jet both towards and away from the rigid wall (R_e = 2.06 mm, R_{max} = 1.95 mm, H' = 3.14, p_v = 52.5 kPa). The top row of images (a) is adapted from the experiments, Figure 2.16(b), and the bottom row of images (b) shows corresponding numerical simulations. The respective timing of each frame is shown at the bottom of the image, and a 5 mm scale bar is shown at the bottom right hand corner.

The second case shown in Figure 3.11 corresponds to the experimental case of Figure 2.16(b), with R_e = 2.06 mm, R_{max} = 1.95 mm, H' = 3.14, and p_v is selected to be 52.5 kPa. The cavitation bubble collapses sooner at around 640 μs in this case. This collapse is matched on the simulations with a lower p_v value of 52.5 kPa, as compared to the previous case (Figure 3.10). In this case, we can see from the experimental results that the cavitation bubble collapses with what appears to be two liquid jets, one directed towards the wall and the other away. However from the simulations, it seems that the cavitation bubble could have split into two bubbly clouds instead, with noticeable compressions along its equatorial axis. This could have created what appears to be two split portions of the cavitation bubble (upper and lower bubble lobes) after the collapse, which continues to expand after t = 640 μs. This could have resulted in what appears to be two liquid jets directed both towards and away from the rigid wall. The cavitation bubble reaches its maximum volume at around 240 μs in the numerical simulations, slightly earlier than the cavitation bubble in the experiments, which is around

320 μs. And as before, the surface instabilities on the experimental air bubble are not present in the simulations. However, the simulations still appear to fit the experimental bubble oscillations to a good degree.

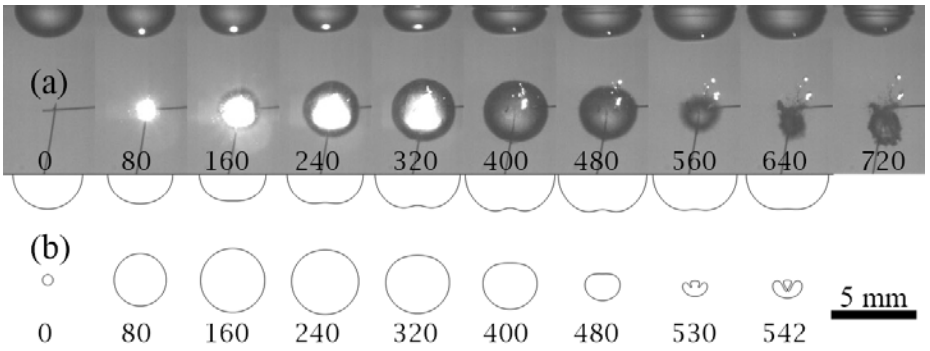

FIGURE 3.12: Case of cavitation bubble collapse jet away from rigid wall (R_e = 2.00 mm, R_{max} = 1.91 mm, H' = 3.16, p_v = 42.5 kPa). The top row of images (a) is adapted from the experiments, Figure 2.16(c), and the bottom row of images (b) shows corresponding numerical simulations. The respective timing of each frame is shown at the bottom of the image, and a 5 mm scale bar is shown at the bottom right hand corner.

The final case shown in Figure 3.12 corresponds to that of Figure 2.16 in Section 2.2, which is the case of a cavitation bubble collapse with a liquid jet directed away from the wall-attached air bubble. R_e = 2.00 mm, R_{max} = 1.91, H' = 3.16 in this case, and to match the bubble collapse timing, p_v is selected to be 42.5 kPa in the simulations. The simulations once again correctly predicts the liquid jet direction in this case, showing a collapse jet on the cavitation bubble directed away from the wall at t = 542 μs. It can be seen from both in the experiments and simulations that the air bubble contracts initially during the cavitation bubble expansion and then expands to almost its maximum size during the cavitation bubble collapse. Essentially, the numerical simulations have verified the hypothesis from the experiments that the vapour pressure p_v is important in that it could influence the cavitation bubble collapse direction for cases with similar geometrical parameters. p_v affects the collapse time of the cavitation bubble and consequently changes the phase difference between the two bubbles. For cases with similar

R_e, R_{max}, and H', a case with greater value of p_v is more likely to have a cavitation bubble collapse jet towards the wall-attached air bubble.

In the case above (Figure 3.12), the two bubbles appear to be perfectly out of phase and the cavitation bubble collapses with a jet away from the air bubble. Conversely for Figure 3.10, we can see that the air and cavitation bubbles are contracting in phase just before the cavitation bubble collapse, which results in a jet towards the rigid wall. The case of Figure 3.11 are neither in phase or perfectly out of phase, hence appears to be in a transition between collapse jet towards and away from the wall. To study the volume progression of the bubbles, a volume plot of both bubbles in the above three cases is generated for evaluation. Further, pressure contour plots of the liquid region around the bubbles that creates the change in bubble oscillation shape and collapse jet directions are also conducted. The results are shared in the next subsection.

3.3.2.2 Volumes and Pressures

Figure 3.13 shows three volume time curves of the cavitation and air bubble in the simulations conducted in the previous Section 3.3.2.1. The bubble volumes are calculated using the same Adaptive Active Contour method used to compute the bubble radii (Boudier, 1997). The graphs (a), (b) and (c) correspond to the cases of cavitation bubble collapse jet towards, both towards and away, and away from the wall-attached air bubble respectively. The red lines show the volume curves of the initially quiescent hemispherical air bubble, whereas the blue lines represent the cavitation bubble volumes. As previously discussed, the simulation parameters for the three cases are similar, except for distinct p_v values. This can be seen from the difference in cavitation bubble oscillation period, which is in decreasing order for Figure 3.13(a) (T = 760 μs), Figure 3.13(b) (T = 640 μs), & Figure 3.13(c) (T = 560 μs). The air bubbles on the other hand, have

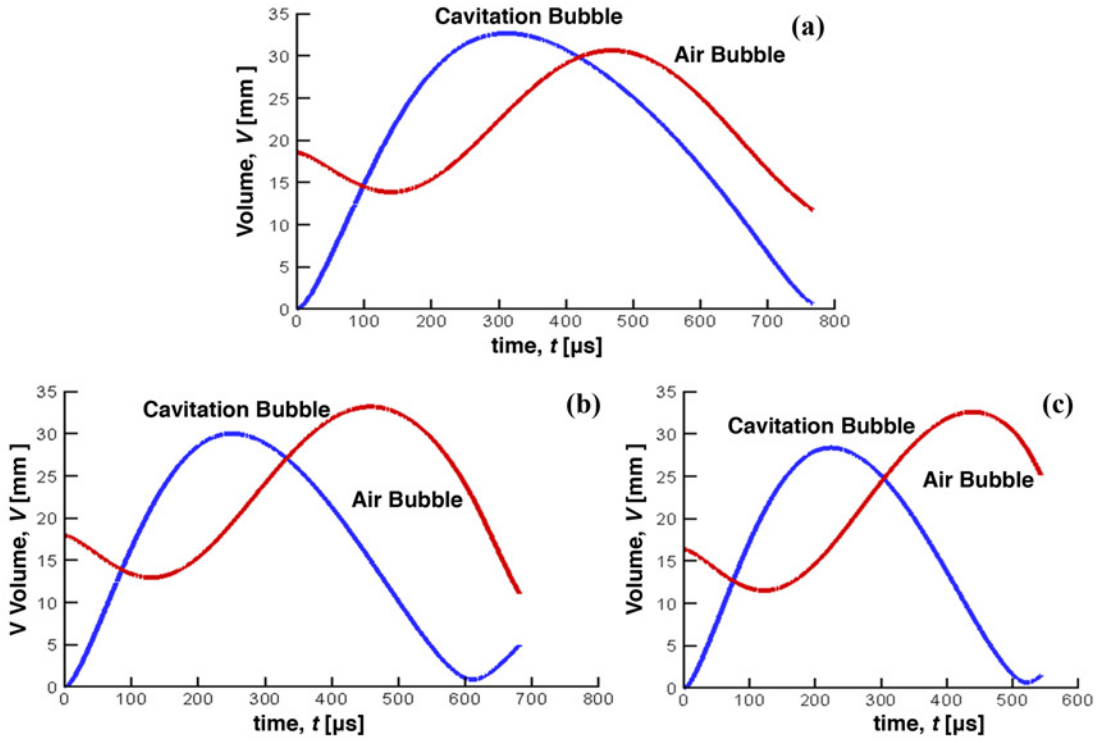

FIGURE 3.13: Cavitation bubble and air bubble volume V against time t curves of simulations conducted in (a) Figure 3.10, (b) Figure 3.11, & (c) Figure 3.12.

rather similar oscillation period, reaching their first minimum volume around 150 μs and first maximum at around 500 μs. This causes the two bubbles to have different phase differences across the three cases in Figure 3.13. For Figure 3.13(a), it is noticed that the air bubble appears to be in phase with the cavitation bubble at its point of collapse, with both bubbles approaching their minimum volumes. Conversely for Figure 3.13(c), the air bubble is close to its first maximum volume during the point of cavitation bubble collapse. This suggests that the bubbles are out of phase, which results in a collapse liquid jet directed away from the wall attached air bubble. Figure 3.13(b) appears to be an intermediate scenario in which the bubble is pinched off into two lobes, and collapses with two portions, one towards the wall and one away from the wall. These results suggest that we should be able to anticipate different cavitation bubble collapse jet directions based on the phase difference between the bubbles in such a problem.

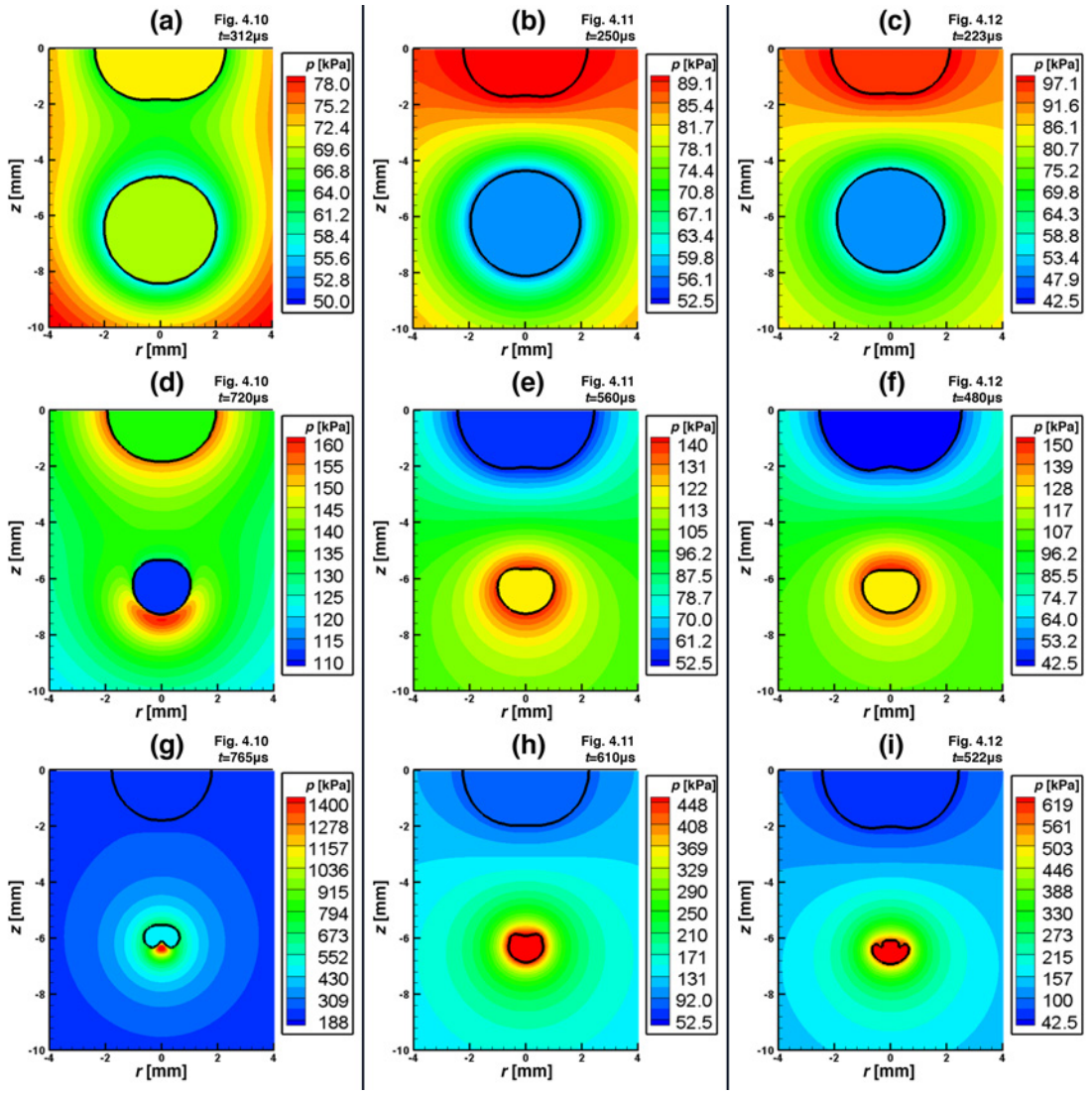

FIGURE 3.14: Pressure contour at selected timings of numerical simulation results presented in Figure 3.10 (for (a), (d) & (g)), Figure 3.11 (for (b), (e) & (h)), & Figure 3.12 (for (c), (f) & (i)). The top row ((a), (b), & (c)) corresponds to the timings in which the cavitation bubble reaches its maximum volume, the middle row ((d), (e), & (f)) is an intermediate timing during the collapsing phase of the cavitation bubble, and the bottom row ((g), (h), & (i)) contains timings just before the cavitation bubbles collapse or minimum volume.

The pressure field of the interactions between the cavitation bubble and air bubble during their oscillations are computed and presented as Figure 3.14 in the form of pressure contour plots. The image set on the left, centre and right columns of the figure correspond to the cases in Figures 3.10(b), 3.11(b), & 3.12(b) respectively. Essentially, they represent the three types of cavitation bubble collapse jet directions that have been discussed previously. Three main timings are selected for these pressure plots: maximum

cavitation bubble volume (top row), arbitrary timing during the collapse phase of the cavitation bubble (middle row), and just before the cavitation bubble minimum volume or collapse (bottom row). On the first look, one would notice that the plots on the middle and right columns of Figure 3.14 are more similar, whereas the plots on the left Figure 3.14 are more distinctive. For example, during the timing of maximum cavitation bubble volume, both Figures 3.14(b) & (c) show a marked pressure gradient between the two bubbles. Figure 3.14 (a) on the other hand show a much flatter pressure profile between the two bubbles. This effect develops into the next 3 set of images in the second row of Figure 3.14 ((d), (e), & (f)). In Figure 3.14(d), the cavitation bubble is slightly compressed its surface closer to the wall and air bubble. However, there is a high pressure region built up on the fluid just outside of the bubble surface away from the wall. For Figures 3.14(e) & (f), the cavitation bubble are both similarly shaped, with a compressed portion of the bubble surface closer to the wall, and a rounded bottom on the surface away from the wall. The pressure profiles around the two bubbles are also somewhat similar, except that the high pressure region surrounds the cavitation bubble more evenly for Figure 3.14(e) but concentrates on the surface of the bubble closer to the wall for Figure 3.14(f). Essentially, the different regions of pressure build-up around the cavitation bubbles as they are rapidly collapsing appear to identify the direction of the collapse jet(s). This is shown in Figures 3.14(g), (h), & (i) just before the cavitation bubble collapse which suggest a liquid jet towards, both towards and away from, and away from the wall-attached air bubble respectively.

3.3.3 Discussion and Conclusion

Numerical simulations that complement the experimental results of the problem of a cavitation bubble near a wall-attached quiescent air bubble (in Section 2.2) have been

presented in this section. The dependency of vapour pressure p_v of the cavitation bubble on its collapse jet direction is investigated. It is known that the experimental spark bubble oscillation time is directly related to $R_{max}\sqrt{\frac{\rho}{p_\infty - p_v}}$, wherein any changes in the vapour pressure is predicted with an accompanying change in time taken for the bubble to collapse (as in Section 2.2.2.5). The results in the present subsection show that a greater p_v may cause a cavitation bubble to collapse with a jet towards, rather than away from the wall. The results also show good comparison with the experiments conducted, validating this resource efficient model of numerical computation for this problem. From the model, an estimate of the influence of p_v due to our low-voltage spark discharge experiments is also obtained. The cases in Figure 3.10, 3.11, and 3.12 shows p_v value of 65 kPa, 52.5 kPa and 42.5 kPa respectively. This suggests that non-trivial deviations in p_v could be present in the experimental results and that the investigation of its influence as in this subsection could be useful in similar problems. Volume time curves presented in Figure 3.13 also show the phase difference changing due to changes in p_v values used in the simulations. It also ascertains that for the two bubbles to be in phase during the cavitation bubble collapse, there is a tendency for a liquid jet directed towards the wall; for bubbles that are out of phase during the collapse, the liquid jet tends to be directed away from the wall; and for an intermediate case between the two, there could be a case in which the cavitation bubble splits into two bubbly lobes, continue to oscillate both towards and away from the wall. This behaviour is similar to the dynamics of two oscillating bubbles with phase differences (Fong et al., 2009; Chew et al., 2011).

The dynamics of interactions between the two bubbles are also investigated in detail with pressure contour plots of the bubbles and the fluid surrounding them. Localized regions of high-pressure around the cavitation bubbles have contributed to the creation of liquid jet(s) that accompany the cavitation bubble collapse. The main motivation of this study

is to mitigate boundary damage from a neighbouring cavitation bubble collapse. From all the cases experimentally or numerically, none of the cavitation bubble collapse jets were found to come into contact with the rigid wall. The liquid jets are either directed away from the wall or are shielded by the attached air bubble. Therefore, as far as rigid boundary protection from cavitation damage due to an impinging cavitation bubble jet is concerned, the addition of an attached air bubble is shown to be effective under the parameters investigated in this study. Furthermore, the results have also suggested that through the recording of H' and T' we are able to predict the directions of the cavitation bubble collapse jets. Once again, this could be important for development of systems to utilize directional fine liquid jets, such as membrane poration applications (Sankin et al., 2010; Ohl, 2010).

Chapter 4

Biomedical Applications of Cavitation Bubble Dynamics

The final results chapter comprises of studies that are directly related to biomedical applications of cavitation bubble dynamics. The emergence of cavitation applications in biomedicine is apparent with recent developments in therapeutic ultrasound, targeted drug delivery etc. Many of these applications require a profound understanding of the behaviour of cavitation bubbles, especially how they would respond to neighbouring structures, bubbles, or cells.

Cavitation bubbles can be introduced into the human body either by spontaneously creating them through external excitation such as a shock wave or ultrasound, or through the introduction of small vesicles or lipid microbubbles and excited (generally with ultrasound) to cavitation. In the first Section 4.1, the interaction of a spark-generated cavitation bubble near a cell-mimic elastic sphere is discussed. This is conducted using a spark-discharge experiment and high-speed imaging to capture the dynamics. In the next Section 4.2, the interactions of a cavitation bubble in proximity to a bacterial biofilm

layer will be investigated, and the prospects of using ultrasound and microbubbles to non-invasively disrupt bacterial biofilms in the human body will be evaluated.

4.1 Cavitation bubble near an elastic sphere

The interaction of a cavitation bubble and neighbouring cells in suspension has been studied by many groups with motivations of sonoporation or drug delivery (Wu and Nyborg, 2008; Le Gac et al., 2007). Cell-identification is another potential application of such an interaction. It is known that the structure of a cell can change with physiological processes (such as differentiation, adhesion etc.) or under stress or attacks from pathogens etc. Cell elasticity or deformability measurement is a typical method to account for markers of such changes. For instance, measurements of cancer cell stiffness reveal a strong correlation between cell deformability and cell malignancy (Suresh, 2007; Cross et al., 2007; Guck et al., 2005). Cross et al. (2007) reported the stiffness of metastatic human breast cancer cells to be more than 70% lower than benign cells. Current methods of measuring cell mechanical properties include Atomic Force Microscopy (AFM) (Tao et al., 2000), micropipette aspiration (Hochmuth, 2000), magnetic methods (Wang et al., 1993), and optical trapping methods (Sleep et al., 1999). By studying a cavitation bubble created in proximity to an elastic cell, the dynamics of bubble and the elastic response of the cell can be studied. Recently, Tandiono et al. (2013) studied the interaction of a laser-induced cavitation bubble next to red blood cell(s) in a microfluidic chamber. They reported up an elongation of up to 5 times the cell's initial size towards the end of the collapse of the cavitation bubble, and that the cell's elasticity is a crucial parameter in this problem. However, there is a lack of such experimental reports on the dynamics of a single cavitation bubble interaction with a neighbouring cell away from

other boundaries. This is because the small length scale of these cells and bubbles (typically micrometer) makes it difficult to control the experiments and require high-speed imaging systems capable of acquiring at extremely high frame rates (Mfps) to record their interactions. One potential answer to this problem would be to employ cell-mimic structures and larger cavitation bubbles. This forms the focus of this study, which is the interaction of a cavitation bubble generated by a low-voltage spark discharge method and a neighbouring elastic sphere of varying elasticity. Results obtained can then be complemented with numerical simulations to better understand the physics involved in the problem and predict scenarios with different parameter choices.

4.1.1 Experimental Setup

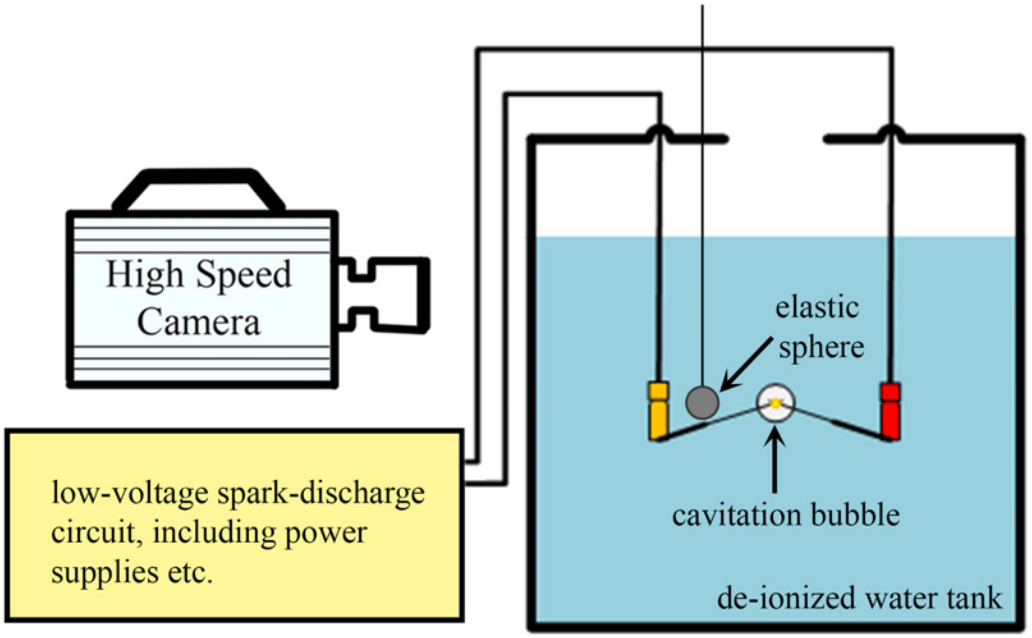

FIGURE 4.1: Experimental setup of spark-discharge cavitation bubble near to an elastic sphere held in place by a retort stand. The centre of the elastic sphere is horizontal to the left of the cavitation bubble centre, with this initial distance defined as H. The process is captured by a high-speed imaging system.

A 60 V low-voltage spark-discharge method is used to generate the cavitation bubble in this study. This method utilizes a MOSFET controlled by a National Instrument NI

USB-6008 Data Acquisition Unit, which allows for the creation of cavitation bubbles with consistent maximum radius. This method has previously been discussed in detail in Section 2.3. A pair of capacitors (2200 μF and 4700 μF) are connected in parallel and charged to 60.0 V with a DC power supply. The two electrode tips (made of 0.1 mm tinned copper wire) are placed in contact with each other, in the middle of a 25 cm x 25 cm x 25 cm Perspex tank filled with de-ionized water to a height of 20 cm. A computer controlled program discharges the capacitors and that creates a spark-discharge cavitation bubble at the initial contact point of the electrodes. Before the start of every experiment, an elastic sphere is placed with its centre horizontally to the side of the contact point in which the cavitation bubble is to be created (Figure 4.1). This is achieved using a fine copper wire (0.1 mm or 0.2 mm diameter) with one end inserted into each of the elastic sphere, and the other attached to a long nylon thread that is fastened to a retort stand above the water surface. The elastic spheres selected in the experiments are made of either silicone rubber or super absorbent polymer (SAP). Depending on the time the SAP spheres are in contact with water, their diameter and subsequently their elasticity can be varied. Using a method presented by Rodriguez et al. (1990), the elastic moduli of the spheres used can be calculated by compressing it between two plates of a load cell and measuring the change in its equatorial diameter. The densities of the spheres were calculated using a digital weighing scale and a pair of digital vernier caliper. Silicone rubber spheres of diameter 8.6 mm are used, and they are found to possess a shear modulus $G = 312$ kPa (and Young's Modulus $E = 936$ kPa, assuming a Poisson's ratio of 0.50 for elastic material) and a density of 1180 kg.m^3. Two types of SAPs are used: they have a shear modulus $G = 19$ kPa and 4 kPa (corresponding $E = 56$ kPa and 12 kPa) respectively when grown to a diameter of 5 mm.

The initial radius of the elastic sphere is defined as R_s and the maximum bubble radius of the cavitation bubble is defined as R_{max}. The initial distance between the centre of the sphere and the point of spark-discharge is defined as H. Using the maximum cavitation bubble radius as the primary length scale, two key dimensionless parameters used in this study, ${R_s}' = \frac{R_s}{R_{max}}$ and $H' = \frac{H}{R_{max}}$, are obtained. This whole process is captured with a Photron SA5 high-speed camera at 50,000 fps and a shutter speed of 1/50,000 s (Figure 4.1). The 512 x 272 pixels images has a resolution of around 10 pixels/mm. All experiments are conducted under atmospheric pressure and at room temperature (23.5 °C).

4.1.2 Results

With different dimensionless separation distance between the sphere and the bubbles (represented by H'), size ratio ${R_s}'$, and elasticity of the sphere, varying response from both the bubble and the sphere is obtained. Selected results based on the types of spheres and their shear modulus G will be presented in the following subsections.

4.1.2.1 Silicon rubber sphere, G = 312 kPa (of order 10^2 kPa)

First, results obtained from a cavitation bubble in proximity to a silicone rubber sphere of initial radius R_s = 4.3 mm and shear modulus G = 312 kPa is presented in this section. The results are presented in order of the initial distance in which the cavitation bubble is created away from the centre of the sphere H. In the first case Figure 4.2, the cavitation bubble is created at the centre of the crossing of the fine wire electrodes and H = 11.9 mm. A spark is generated at this point and it rapidly grows into a cavitation bubble, as seen at t = 160 μs. This cavitation bubble reaches its maximum radius of

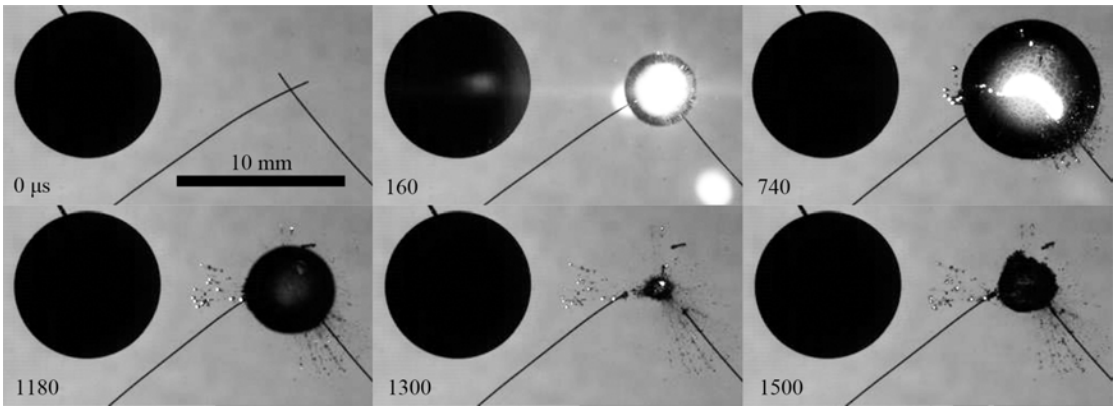

FIGURE 4.2: Cavitation bubble (right) beside silicon rubber sphere (left) at a large distance initially. $R_s = 4.3$ mm, $R_{max} = 4.14$ mm, $R_s{}' = 1.04$, $H' = 2.87$. The cavitation bubble expands and collapses spherical with no noticeable effect on the rubber sphere. Respective timings of each frame are shown at the bottom left hand corner. A 10 mm scale bar is shown on the bottom right hand corner of the first frame.

$R_{max} = 4.14$ mm at $t = 740$ μs. This allows us to obtain the dimensionless parameter values of $R_s{}' = 1.04$ and $H' = 2.87$. At this point in time, the rubber sphere does not appear to have undergone significant displacement or deformation due to the nearby cavitation bubble. The cavitation bubble appears to expand spherically, and it then collapses rapidly and radially at $t = 1.30$ ms. At $t = 1.5$ ms, the collapsed bubble is seen to re-expand into a spherical bubbly cloud while the silicone rubber sphere remains unaffected.

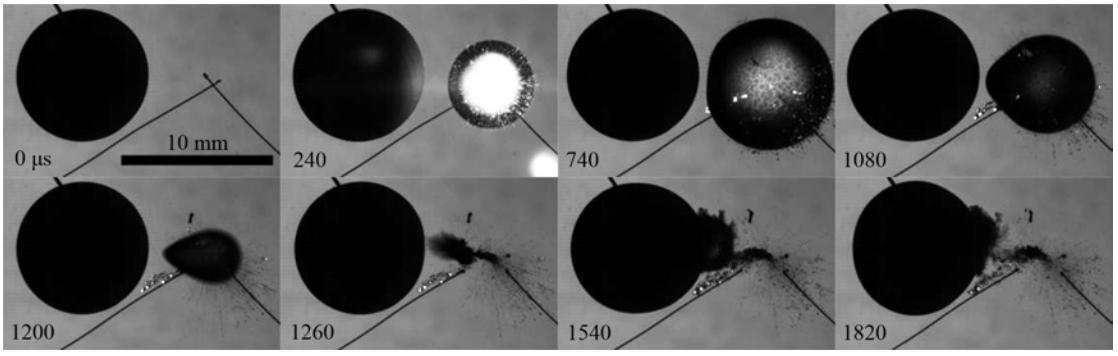

FIGURE 4.3: Cavitation bubble (right) beside silicon rubber sphere (left) at a moderate distance away initially. $R_s = 4.30$ mm, $R_{max} = 4.30$ mm, $R_s{}' = 1.00$, $H' = 1.99$. The cavitation bubble expands aspherically and collapses with a liquid jet towards the silicone rubber sphere, which deforms slightly during this process. Respective timings of each frame in μs are shown at the bottom left hand corner. A 10 mm scale bar is shown on the bottom right hand corner of the first frame.

The second case (Figure 4.3)shows an identical silicon sphere but now with a cavitation

bubble created at a increased initial distance away, $H = 8.56$ mm. The cavitation bubble expands rapidly from the spark-discharge and reaches its maximum radius of 4.30 mm at $t = 740$ μs. Therefore, $R_s{}' = 1.00$ and $H' = 1.99$ for this case. The cavitation bubble's expansion is not entirely spherical with its surface slightly compressed near the silicon rubber sphere. The shape of the rubber sphere however does not vary much. The cavitation bubble is also seen to contract aspherically, as seen at $t = 1.08$ ms & 1.20 ms. The cavitation bubble surface closest to the silicone sphere does not undergo much translation as the remaining parts of the bubble rapidly collapses. At $t = 1.26$ ms, the cavitation bubble is observed to collapse with a liquid jet towards the silicone rubber sphere. This jet can be visualized with a bubbly cloud that propagates towards the rubber sphere at $t = 1.54$ ms & 1.82 ms.

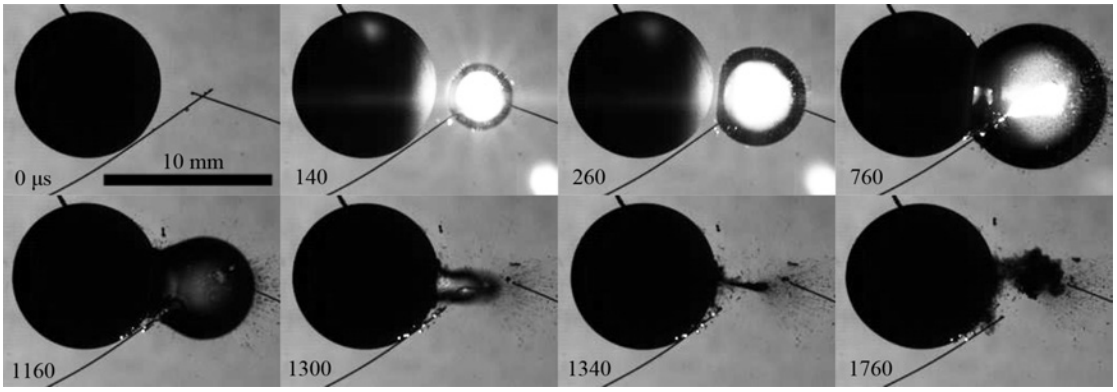

FIGURE 4.4: Cavitation bubble (right) created near a silicon rubber sphere (left). R_s = 4.30 mm, $R_{max} = 4.30$ mm, $R_s{}' = 1.00$, $H' = 1.56$. The cavitation bubble comes into contact with the rubber sphere during its expansion, then collapses with an impinging liquid jet onto the sphere. Respective timings of each frame are shown at the bottom left hand corner. A 10 mm scale bar is shown on the bottom right hand corner of the first frame.

The third case displayed in Figure 4.4 has the parameters of $R_s = R_{max} = 4.30$ mm, $R_s{}' = 1.00$, and $H' = 1.56$. During its expansion, the cavitation bubble surface quickly comes into close proximity to the silicone rubber sphere, as seen at $t = 260$ μs. At the cavitation maximum bubble radius at $t = 760$ μs, the bubble is seen to have one portion of its surface engulfing a portion of the silicone sphere. The bubble appears

to have attached itself to the silicone sphere during its expansion and this causes the sphere to translate slightly to its left. During its contraction phase, the part of the cavitation bubble attached to the silicone sphere shrinks much less as compared to the other parts of the cavitation bubble, as seen at $t = 1.16$ ms. This continues until the bubble collapse at $t = 1.34$ ms, in which the frame before at $t = 1.30$ ms shows signs of sonoluminescence like most of the other cases. This cavitation bubble collapse brings about a liquid jet towards the silicone rubber similar to Figure 4.3. The silicone sphere is observed to translate back to its initial position (towards the right of the image) during the cavitation bubble collapse. Once again, it does not appear that the silicone sphere underwent much deviation in its shape during the cavitation bubble oscillations.

4.1.2.2 Super absorbent polymer, $G = 21$ to 29 kPa (of order 10^1 kPa)

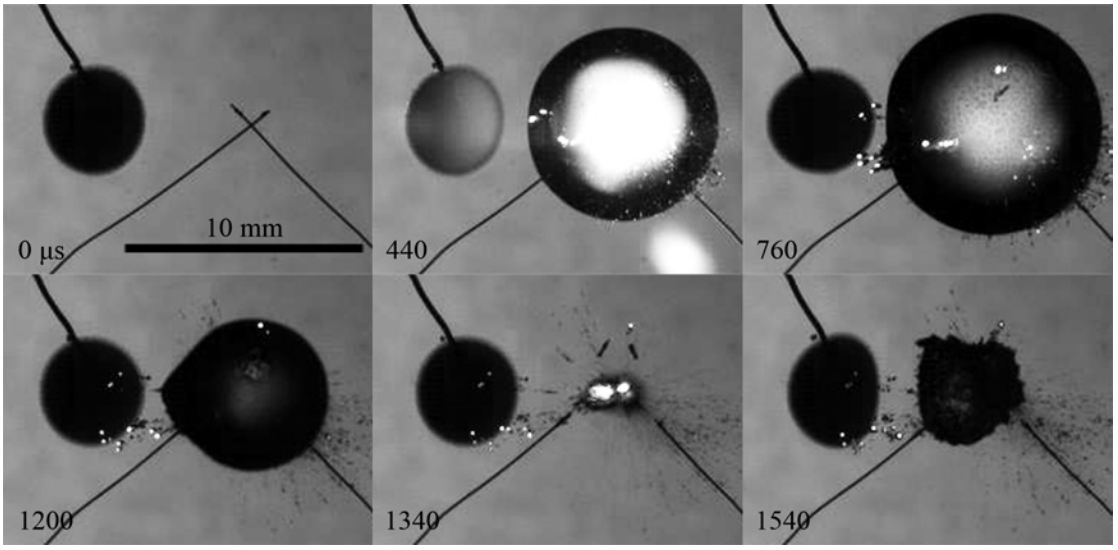

FIGURE 4.5: Cavitation bubble (right) created at a moderate distance away from a SAP sphere (left). $R_s = 2.21$ mm, $R_{max} = 4.59$ mm, $R_s{}' = 0.48$, $H' = 1.42$, and $\rho = 1180$ kg.m^3 ($E = 87$ kPa, $G = 29$ kPa). The cavitation bubble expands without touching the SAP sphere, and collapses spherically. The SAP sphere is noticed to undergo shape deformations, elongating and compressing horizontally. Respective timings of each frame are shown at the bottom left hand corner. A 5 mm scale bar is shown on the bottom right hand corner of the first frame.

The next set of elastic spheres used is the first type of super absorbent polymers (SAP). They possess varying density and elasticity with size (due to different time exposed to

water) and is found have a shear modulus $G = 19$ kPa (corresponding $E = 56$ kPa) when grown to a R_s of 2.5 mm. When their radius is smaller, they are correspondingly stiffer and possess a higher density. In Figure 4.5,a case of an SAP with $R_s = 2.21$ mm beside a cavitation bubble initially created at $H = 6.52$ mm away from the centre of the SAP sphere is shown. This SAP sphere has density $\rho = 1180$ kg.m^3 and modulus of elasticity $G = 29$ kPa (corresponding $E = 87$ kPa). This means that it has a comparable density with that of the silicone rubber sphere but is an order of magnitude lesser in its modulus of elasticity. This changes its response in its interaction with the cavitation bubble. As shown at $t = 440$ μs, the cavitation bubble is rapidly expanding and this causes the elastic sphere to be slightly compressed in the horizontal direction. At $t = 760$ μs, the cavitation bubble reaches its maximum radius of $R_{max} = 4.59$ mm, giving ${R_s}' = 0.48$ and $H' = 1.42$ for this case. At this point of time, the SAP sphere is noticed to be slightly elongated in its horizontal axis instead, while traversing to the left of the frame as compared to its initial position. The cavitation bubble then enters its collapsing phase rapidly, as shown at $t = 1.20$ ms. At this time, the SAP sphere changes shape to resemble that of $t = 0$ μs while the neighbouring cavitation bubble collapses with a pointed tip on its surface closer to the elastic sphere. At $t = 1.34$ ms, the cavitation bubble collapses and it rebounds spherically into a bubbly cloud as shown at $t = 1.54$ ms. This rapid and violent collapse and rebound causes a change in the shape of the SAP sphere as a result. The right hand side of the elastic sphere is evidently compressed to a nearly vertical surface whereas the left hand side surface of the elastic sphere remains somewhat rounded at $t = 1.54$ ms. This appears to be an amplified effect of the SAP sphere shape noticed at $t = 440$ μs (similarly compressed on its right hand side).

The behaviour of the cavitation bubble beside the SAP sphere changes when H' is decreased. Figure 4.6 shows the case of a SAP sphere ($\rho = 1117$ kg.m^3, $G = 21$ kPa) of

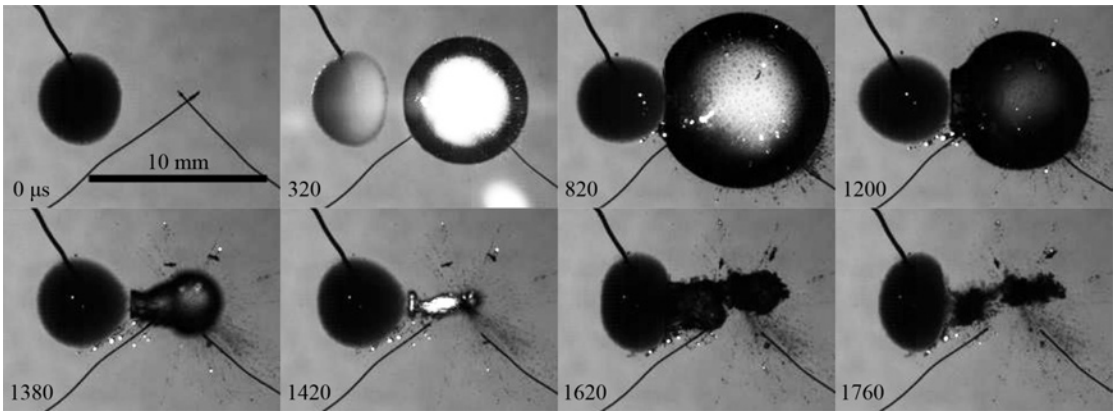

FIGURE 4.6: Cavitation bubble (right) created near to a SAP sphere (left). R_s = 2.45 mm, R_{max} = 4.90 mm, $R_s{}'$ = 0.50, H' = 1.21, and ρ = 1117 kg.m^3 (E = 61 kPa, G = 21 kPa). The cavitation bubble expands until part of its surface is in contact with the SAP sphere, and then collapses with a 'mushroom' shape ending with a noticeably bright collapse region. Respective timings of each frame are shown at the bottom left hand corner. A 5 mm scale bar is shown on the bottom right hand corner of the first frame.

R_s = 2.45 mm with a cavitation bubble created at H = 5.93 mm initially. The cavitation bubble reaches its maximum radius R_{max} = 4.90 mm at t = 820 μs, hence we now have $R_s{}'$ = 0.50 and a decreased H' of 1.21 as compared to the previous case (Figure 4.5). Similar to the previous case in Figure 4.5, the SAP sphere is seen to be compressed in its horizontal axis when the bubble is expanding (t = 320 μs) and then elongates horizontally when the cavitation bubble reaches its the maximum radius (t = 820 μs). The cavitation bubble has a portion of its surface in contact of the SAP sphere during its expansion in this case. This portion of the bubble remains in close proximity to the SAP as it collapses, forming a 'mushroom' or 'parachute' shaped collapsing bubble as shown at t = 1.20 ms & 1.38 ms. The portion of the bubble close to the SAP sphere is observed to have a vertical surface that appears flattened. At t = 1.42 ms, the cavitation bubble collapses with the neighbouring SAP sphere having a flatter surface on its left hand side as compared to a slightly pointed right hand side. There is a bright region of what appears to be sonoluminescence from the collapsed bubble. This bright region is observed to be elongated in the horizontal direction, presumably an effect of

the elongated shape of collapsing cavitation bubble. This collapse is followed by two bubbly jets, seemingly directed towards and away from the SAP sphere (t = 1.62 ms & 1.76 ms). The liquid jet directed to the SAP sphere clearly comes into contact with the sphere and causes it to be compressed horizontally.

4.1.2.3 Super absorbent polymer, G = 5 to 8 kPa (of order 10^0 kPa)

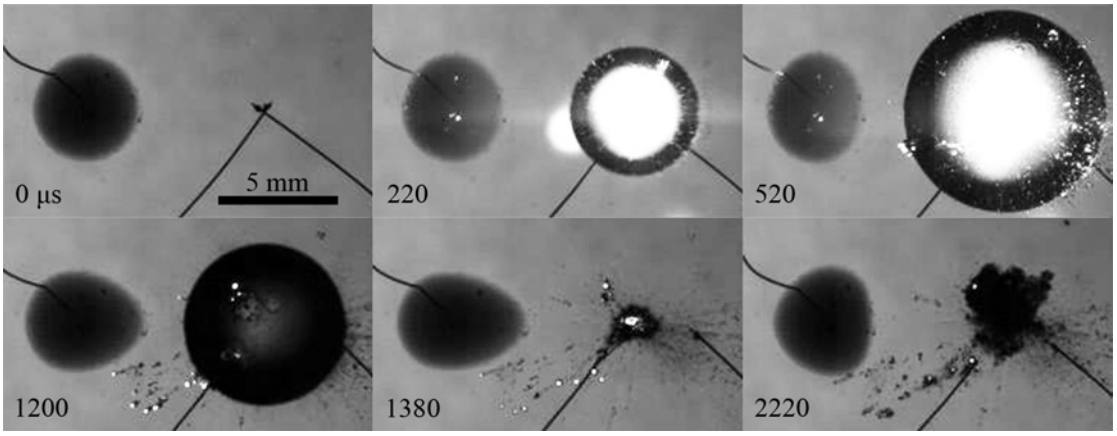

FIGURE 4.7: Cavitation bubble (right) created far away from a SAP sphere (left). R_s = 2.24 mm, R_{max} = 4.23 mm, $R_s{}'$ = 0.53, H' = 1.77, and ρ = 1065 kg.m^3 (E = 16 kPa, G = 5 kPa). The cavitation bubble expands and collapses spherically, whereas the SAP sphere compresses during the bubble expansion and elongates while the bubble is collapsing. Respective timings of each frame are shown at the bottom left hand corner. A 5 mm scale bar is shown on the bottom right hand corner of the first frame.

The next set of results is obtained using a different super absorbent polymer, which has a shear modulus of elasticity an order of magnitude smaller than the previous SAP. When these SAP spheres are grown to a R_s of 2.5 mm, they are found to possess a shear modulus G = 4 kPa (corresponding E = 12 kPa). The first example (Figure 4.7) shows one such case with a cavitation bubble created far away from it initially. The initial parameters of this example are R_s = 2.24 mm, H = 4.79 mm, and the SAP is calculated to have G = 5 kPa and ρ = 1065 kg.m^3. At t = 220 μs, we can see the expanding cavitation bubble to the right of the SAP. As compared to its initial shape (t = 0 μs), the SAP appears slightly compressed on its right hand side surface as in the previous SAP cases (Figures 4.5 & 4.6). At t = 520 μs, the cavitation bubble reaches

its maximum radius $R_{max} = 4.23$ mm, giving $R_s{}' = 0.53$ and $H' = 1.77$. at this point in time, the SAP sphere is noticed to be compressed further horizontally due to the cavitation bubble. As the cavitation bubble is collapsing at $t = 1.20$ ms, the contracting bubble is seen to draw the neighbouring SAP sphere towards it, elongating the right hand side of the SAP. This is similar to the elongation of red blood cell observed by Tandiono et al. (2013). This continues until the cavitation bubble collapse at $t = 1.38$ ms, and the SAP is at its maximum elongated shape with a compressed portion to the right, and a slightly rounded left side. The collapsed cavitation bubble then expands into a bubbly cloud that oscillates. This causes the stretched portion of the SAP to spring back to the left, which can be noticed by its flattened surface at $t = 2.20$ ms. The cavitation bubble in this case expands and collapses spherically and does not come into contact with the SAP at any instance.

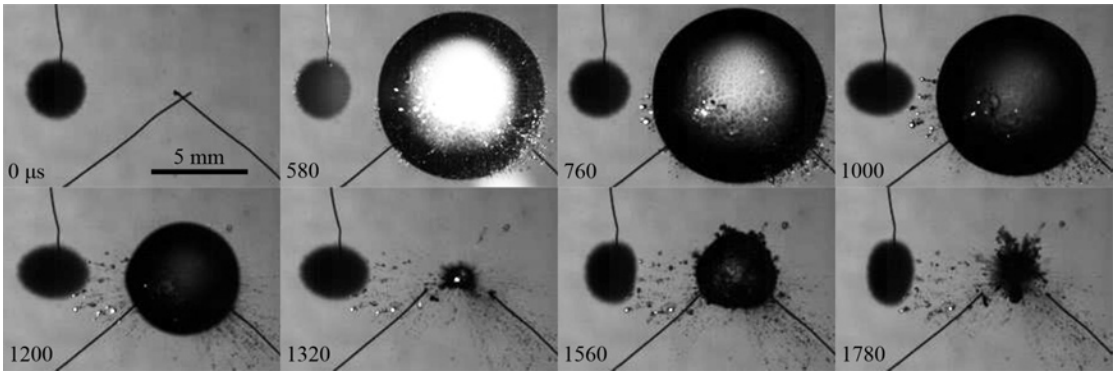

FIGURE 4.8: Cavitation bubble (right) created at a moderate distance from a SAP sphere (left). $R_s = 1.56$ mm, $R_{max} = 4.52$ mm, $R_s{}' = 0.35$, $H' = 1.45$, and $\rho = 1261$ kg.m^3 ($E = 24$ kPa, $G = 8$ kPa). The cavitation bubble expands and collapses spherically, while compressing and elongating the SAP sphere in this process. Respective timings of each frame are shown at the bottom left hand corner.

The second example of a cavitation bubble interacting with this SAP is shown as Figure 4.8. A cavitation bubble is created at the spark point, at $H = 6.55$ mm away from an SAP sphere of $G = 8$ kPa, $\rho = 1261$ kg.m^3, and $R_s{}' = 1.56$ mm. The cavitation bubble expands and compresses the SAP as seen at $t = 580$ μs. At its maximum radius $R_{max} = 4.52$ mm, the SAP appears to be almost spherical with a slightly elongated right

hand portion. The contracting cavitation bubble causes the SAP to stretch horizontally on both ends as seen at t = 1.00 ms & 1.20 ms. The cavitation bubble is noticed to collapse with a slightly pointed portion at its side close to the SAP sphere (t = 1.20 ms). It then collapses at t = 1.32 ms and following which the bubble expands spherically at t = 1.56 ms and collapses again at t = 1.78 ms. This re-expanding bubble causes the SAP to turn from elongated horizontally to a vertical elongated 'rod' shape at t = 1.78 ms. As compared to Figure 4.7, H' and ${R_s}'$ are both smaller at 1.45 and 0.35 respectively in this case. As a result, the bubble still does not come into contact with the SAP during its oscillations.

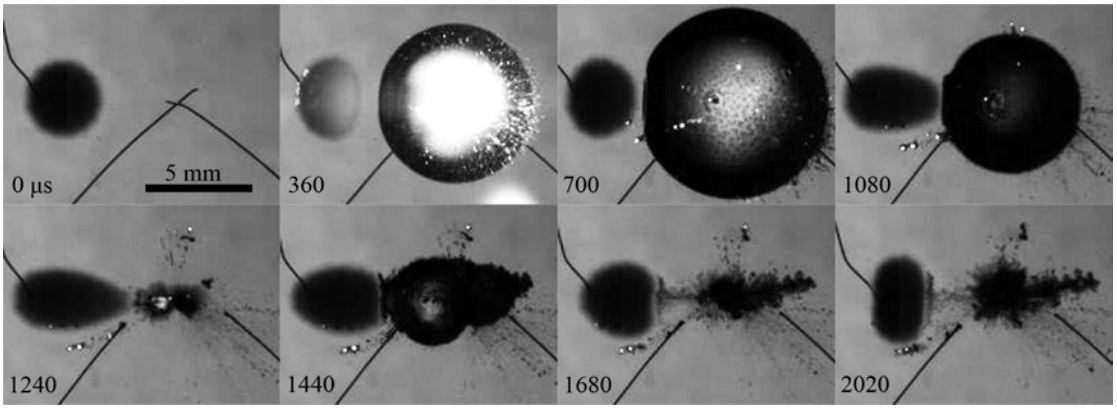

FIGURE 4.9: Cavitation bubble (right) created near to a SAP sphere (left). R_s = 1.86 mm, R_{max} = 4.52 mm, ${R_s}'$ = 0.41, H' = 1.21, and ρ = 1165 kg.m^3 (E = 20 kPa, G = 7 kPa). The cavitation bubble expands until a portion of it is very close to the compressed SAP, it then collapses with a 'mushroom' shape, during which the SAP is elongated extensively. Respective timings of each frame are shown at the bottom left hand corner.

In the final case Figure 4.9, the cavitation bubble is created very near to the SAP sphere and they come into close contact with one another, as in the cases of Figures 4.4 & 4.6. The SAP sphere has an initial radius of ${R_s}'$ = 1.86 mm and is initially located at H = 5.47 mm away from the cavitation bubble spark point. The SAP sphere is found to have G = 7 kPa and ρ = 1165 kg.m^3. The cavitation bubble expands while compressing the SAP horizontally at t = 360 μs, and reaches R_{max} = 4.52 mm at t = 700 μs. The left surface of the cavitation bubble is noticed to be compressed slightly, and

only maintaining a small fluid gap between itself and the SAP sphere. During its first contraction phase, the cavitation bubble causes the SAP sphere to elongate and comes into close contact with the bubble, as shown at $t = 1.08$ ms. The contracting bubble is noticed to have a flattened vertical surface that is in close contact with SAP and a rounded right hand portion while collapsing, forming a previously noticed 'mushroom' like shape. The cavitation bubble collapses at $t = 1.24$ ms and at this point you can notice that the SAP sphere has now been stretched extensively to 5.57 mm in length. That represents a 50% increase compared to its initial horizontal span (or diameter). The cavitation bubble then re-expands ($t = 1.44$ ms) and collapses again at $t = 1.68$ ms. This causes the elastic sphere to be compressed horizontally, and shape oscillations occur. The SAP is seen to form a vertical rod-like shape at $t = 2.02$ ms, to its right a bubbly cloud which is what remains of the collapsed cavitation bubble.

4.1.3 Discussion and Conclusion

Results that showcase the interaction of a cavitation bubble with a neighbouring elastic sphere of distinct elasticity have been presented. For the case of silicone spheres which has G of the order of 10^3 kPa, minimal deformation to the spheres in all the cases presented is observed. The cases showcased vary in the initial relative distance between the cavitation bubble and the elastic sphere. When the bubble is created at a large H' away from the silicone sphere (Figure 4.2), it is seen to expand and collapse spherically and the silicone sphere is observed to retain its position and shape throughout the bubble oscillation. When H' is reduced (Figure 4.3), aspherical bubble expansion is noticed and the cavitation bubble collapses with a liquid jet towards the silicone sphere. The silicone sphere is seen to undergo minor shape oscillation for this case. When H' is reduced further (to 1.56 in Figure 4.4), the cavitation bubble surface comes into contact with

the silicone sphere during its expansion and collapses with its contact surface attached to the elastic sphere for a long duration. Shape oscillations of the silicone sphere are noticeable after the collapse of the cavitation bubble.

Results for two types of super absorbent polymers, with G in the order of 10^1 kPa and 10^0 kPa respectively are also presented. The elastic spheres in these cases are noticed to undergo shape deviations during the oscillations of the neighbouring cavitation bubble. The SAP spheres with a smaller value of G (Figures 4.7, 4.8, & 4.9) are noticed to deviate more from their initial shape as compared to the stiffer SAP spheres (Figures 4.5 & 4.6). The extent of such shape deviations is more pronounced when the cavitation bubble is created relatively closer (smaller H') to the elastic sphere. In the most elaborated case presented (Figure 4.9), the SAP sphere is noticed to stretch to a maximum length of 1.5 times its initial diameter during the cavitation bubble collapse. Different growth and collapse shapes of the cavitation bubble which is beside these SAP spheres can also be noticed. If the cavitation bubble is close enough to the SAP spheres, aspherical growth and collapse is observed. The compressions on the surface of the bubble are due to the SAP spheres being in very close proximity. This is rather similar to the observation for the case of a cavitation bubble created near to a silicone sphere. Similarly, spherical growth and collapse of the cavitation bubble is noticed for cases with relatively large H'. When H' is small, the bubble comes into close contact with the SAP sphere during its oscillation and this is usually accompanied with a liquid jet during the bubble collapse.

The results presented show typical interactions between a cavitation bubble and an elastic sphere if one varies dimensions, elasticity and initial distance away from the bubble. This study has presented some insights on the response of a cell in suspension with a neighbouring cavitation bubble. It appears that depending on the cell properties as physical parameters of this problem, the cell could undergo large extents of elongation

and stress. This could be important for studies in the use of targeted cavitation for the disruption of cells. Examples of recent studies in this field are Kooiman et al. (2011); Carson et al. (2012); Sirsi and Borden (2012); Tandiono et al. (2013); Kiessling et al. (2014). The study also reveals that the initial distance between the cavitation bubble and the cell can garner different interaction patterns between the two. However to gain a comprehensive understanding of this phenomenon, it is very beneficial to include numerical simulations. It would allow us to correlate predicted elastic response of the sphere to the important parameters listed here. This could develop into a prospective measurements method of cell mechanical properties. As such, the results in this section has been supplemented with a Finite-Element coupled with BEM model, similar to that presented in Section 2.1.

4.2 Ultrasound-targeted microbubble disruption of bacterial biofilms

In Chapters 2 & 3, the interactions of a single cavitation bubble beside neighbouring structures such as a rubber beam, or a neighbouring air bubble have been discussed. In many of the cases presented, one might have noticed the creation of an impinging liquid jet upon the cavitation bubble collapse. The cavitation bubble collapse jet has been studied extensively near a rigid wall (Lauterborn and Bolle, 1975; Blake and Gibson, 1987), or elastic surfaces (Gibson and Blake, 1982; Shaw et al., 1999; Brujan et al., 2001a,b). Such a liquid impinging jet is typically directed towards the neighbouring rigid surface upon the cavitation bubble collapse. This liquid jet can be utilized towards the disruption of bio-materials, or more specifically of bacterial biofilms.

Biofilms refer to surface-adherent cellular aggregates that are often embedded within an extracellular polymeric substance (EPS) matrix. They are also a common root for persistent infections, due to their increased bacterial resistance against antimicrobial agents (Costerton et al., 1999). It is estimated that the antibiotic resistance of bacteria in biofilms are up to a thousand times greater as compared to during planktonic growth (free flowing bacteria in suspension). It is hypothesized that this effect is a result of the barrier property of the EPS matrix (Sutherland, 2001; Jefferson et al., 2005), the stationary phase dormancy of cells in nutrient-depleted zones in the biofilm (Walters III et al., 2003; Fux et al., 2004), and/or the presence of a metabolically heterogeneous bacterial population (Hall-Stoodley et al., 2004; Lenz et al., 2008). A study by Donlan (2001) estimates that around 65% of clinical microbial infections are associated with biofilms. These infections are typically on indwelling medical devices and materials (e.g. catheters, heart valves, & joint prosthesis) (Lynch and Robertson, 2008) and treatment methods tend to be invasive with increasing recurrence rate, complications and costs (Hebert et al., 1996; Matthews et al., 2009). The development of a combination therapy of an anti-biofilm compound with an effective antibiotic is essential to provide adequate exposure of antimicrobial agents at sites of bacterial biofilm infections. However, no such anti-biofilm therapies are currently in clinical use (Römling and Balsalobre, 2012).

There are studies of several effective methods which are able to physically disrupt the bacterial biofilm integrity to enhance efficacy of antimicrobial agents. These methods include the use of an electric or magnetic field (Costerton et al., 1994; McLeod et al., 1999), low-intensity ultrasound (Pitt et al., 1994; Yu et al., 2012), High-intensity focused-ultrasound (HIFU) (Bigelow et al., 2009; Xu et al., 2012), and ultrasound-targeted microbubble disruption (UTMD) (He et al., 2011; Dong et al., 2013), which uses microbubbles as nuclei to create ultrasound-induced cavitation. He et al. (2011); Zhu et al. (2013)

first reported the increased effect of vancomycin against *Staphylococcus epidermidis* biofilm both *in vitro* and *in vivo*, with ultrasound exposure of 0.08 MHz, 1.0 W.cm^{-2}, 50% duty cycle at a 10 minute duration on SonoVue® ultrasound contrast agent (UCA) microbubbles. More recently, Dong et al. (2013); Zhu et al. (2013) also verified the enhanced effects of antimicrobial agents against *Staphylococcus epidermidis* biofilms using UTMD. It is postulated that the microbubbles' collapse with ultrasound increases membrane permeability of the cells by shear stress, rising temperature and activation of reactive aerobic species (He et al., 2011), however the exact mechanisms behind the increased efficacy of UTMD are not understood to date.

As such, this section presents a study in which the physical mechanisms behind UTMD of bacterial biofilms are presented. This is achieved using an experimental setup which utilizes UCA microbubbles, holographic optical trapping to keep the bubble(s) in position, ultrasound and high-speed imaging. The UCA microbubbles are trapped in position at varying distances away from an *Escherichia coli* or *Pseudomonas putida* bacterial biofilm layer on a rigid coverslip, and exposed with ultrasound for cavitation. The results collected provides support towards the development of a non-invasive method to physically disrupt bacterial biofilm in the human body. The influence of several important experimental parameters on the biofilm disruption efficacy is also evaluated.

The work in this section is completed during the author's attachment to the University of Dundee, UK from May 2012 to November 2013.

4.2.1 Experimental Setup

The bacterial strains chosen for this study are the *Escherichia coli* MG1655 omR234 strain (Reisner et al., 2003) and the *Pseudomonas putida* KT2440 strain (Martínez-Gil et al., 2010; Yousef-Coronado et al., 2011). The strains are reportedly good biofilm formers and they were obtained from Prof. Søren Molin from the Department of Systems Biology, Technical University of Denmark (*E. coli*) and Dr. Manuel Espinosa Urgel from the Estación Experimental del Zaidín, Consejo Superior de Investigaciones Científicas (*P. putida*). The bacterial biofilms are cultivated on glass coverslips of either 2.5 mm x 22 mm or 22 mm x 22 mm in dimensions. These coverslips with an adherent bacterial biofilm will be used in the vertical or horizontal orientation in the experimental setup, which will be illustrated later. To prepare these coverslips, a bacterial strain is first inoculated in 5 ml of complete $Luria-Bertani$ (1 x LB) medium, overnight at 200 rpm and 37°C (for *E. coli*) or 30°C (for *P. putida*) in a Infors-HT Multitron Standard shaker. The culture is then diluted 1:100 strain to 1 x LB medium in each well of a TPP® 6-well tissue culture plate, with the glass coverslips placed at the base of the wells. The tissue culture plates are then incubated for 24 hours at 30°C, during which a bacterial biofilm forms on top of the coverslips. The coverslips are then removed and rinsed twice and placed into the ultrasound chamber in the experimental setup Figure 4.10.

The experimental setup used in this study is very similar to that used by Prentice et al. (2005) which comprises of a focused ultrasound transducer submerged in a de-ionized water tank, focusing in a ultrasound chamber illuminated by fibre optic and looking from top down through a microscope object (Figure 4.10). The de-ionized water tank is made of Perspex with dimensions L26 cm x W26 cm x H10 cm and filled with de-ionized water to the height of the horizontal coverslip in the ultrasound chamber (8.5

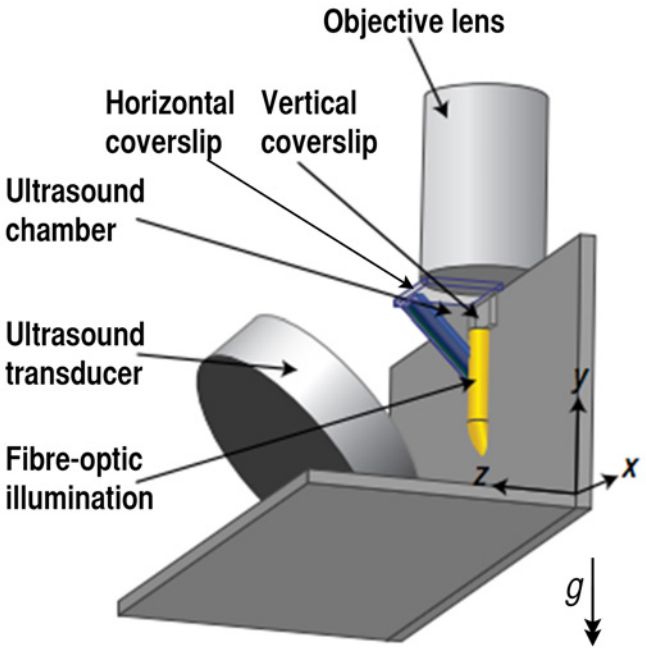

FIGURE 4.10: Experimental setup illustrating a cross sectional portion of a de-ionized water tank with a focused ultrasound transducer, illumination, the ultrasound chamber and the objective lens.

cm). The ultrasound chamber is a section separated out of the main tank with an acetate film into a column with a right-angled triangular cross-sectional profile. This chamber is also filled with de-ionized water and a vertical and a horizontal coverslip (with or without biofilm) are being placed against the upright and horizontal edges of this ultrasound chamber. The ultrasound transducers used are the Sonic Concepts H-101 and H-102 focused ultrasound transducers driven near their resonance at 1.00 MHz and 250 kHz respectively. The transducers are connected to a TTi TGA-1242 arbitrary waveform generator and an Amplifier Research 150A100B RF power amplifier through their respective impedance matching network supplied by Sonic Concepts. The transducers are placed submerged in the water tank and arranged such that the concave transducer elements focus at a common point within the ultrasound chamber. This is achieved using a Precision Acoustics Fibre Optic Hydrophone system, which is also used to measure the resultant peak-negative-pressure (P^-) in the ultrasound chamber.

Values of P^- recorded in this study ranges from 0.1 MPa to 1.0 MPa from the range of input voltage supplied.

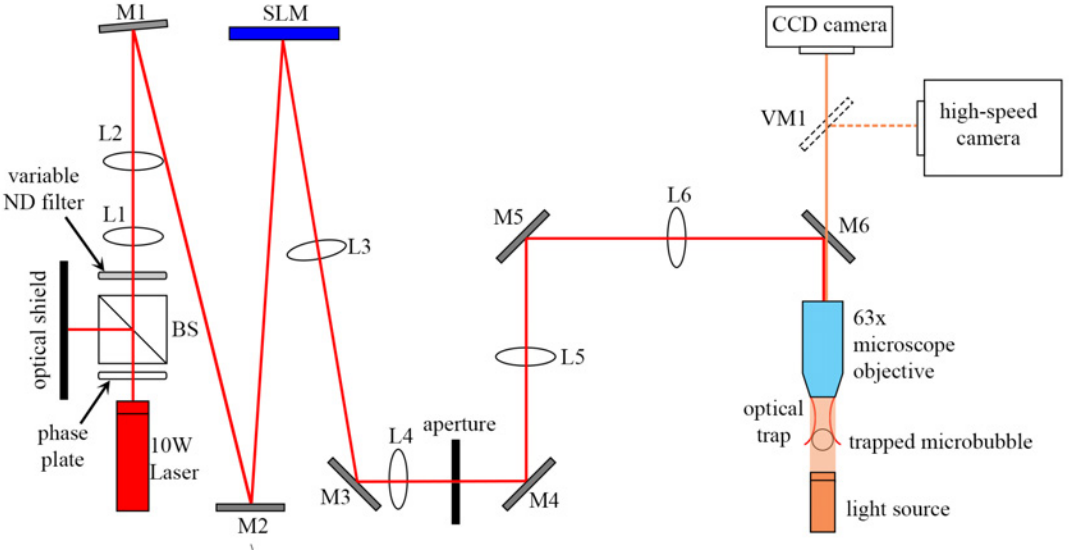

FIGURE 4.11: Holographic optical trapping and imaging setup. Red lines indicate the IR laser beam path, and the orange lines indicate the visible light path for imaging. L - IR lens, M - IR mirror, VM - visible light mirror, BS - 50:50 beam splitter, SLM - spatial light modulator.

The ultrasound chamber is illuminated with a fibre optic cable, directing light upwards towards a Leica HCX PL APO 63x / 1.3 microscope objective lens. The objective lens is arranged with a Baumer TXD08 industrial camera (to allow real-time observation of adjustments and optical trapping) and a Cordin 550-62 rotating mirror high speed camera (for high-speed imaging) with a beam splitter. The fibre optic cable is fed with a lamp-house coupled with a condenser lens to provide illumination during adjustments of the experiment and optical trapping. For high-speed imaging, the condenser lens is connected with a Cordin pulsed xenon flash lamp fed by a capacitor bank unit instead, and the flash is triggered directly from the Cordin 550 high-speed camera. The laser holographic optical trapping setup shown in Figure 4.11 mainly comprises of a IPG Photonics YLM-10-1070-LP 10 W Ytterbium fibre laser and a HOLOEYE Pluto^{TM}spatial light modulator (SLM). The near infrared (IR) laser beam (1070 nm), represented by the red lines, first passes through a phase plate, a 50:50 beam splitter and a variable neutral

density (ND) filter to change the phase and lower the intensity of the incident beam. The light beam then passes through a pair of IR lenses (L1 & L2) to expand and collimate the beam. This beam covers the entire surface of the SLM, which is connected to a computer using it as an extended secondary monitor. An operator specified hologram is displayed on the SLM with in-house Labview software on the computer, and it is variable such that a Laguerre-Gaussian (LG) beam can be produced to optically trap microbubbles of different sizes. This ability to change the LG beam diameter, position and also incorporating multiple optical traps are the key advantages of a computer-generated hologram on an SLM as compared to traditional optical holograms. An aperture is placed in the beam path and adjusted to block out the 0^{th} order beam and only allow the LG beam trap (1^{st} order) to pass through. This beam then passes through L5, L6 and the microscope objective, turning into a laser optical trap that focuses in the ultrasound chamber. The LG beam can be visualized as a focusing cylindrical laser beam and this elaborated beam pattern is essential to trap a bubble (which has a lower refractive index than its surrounding medium). The optical setup is fixed on an hydraulic optical table and adjustments to physically move the bubble into the optical trap is achieved using X-Y-Z micrometer stages supporting the ultrasound tank. The orange lines represent the visible light beginning from the light source. When trapping the bubble, a 12V 100W bulb is used in a lamp house to illuminate the focal plane in the ultrasound chamber, and this is captured with a industrial CCD camera. Once in position and ready, a visible light mirror VM1 is placed in the visible light path to direct the image into the Cordin 550 high-speed camera. The light source is also changed to high-intensity pulsed flash light to ensure ample illumination.

The Cordin 550-62 camera is a 62 frame rotating mirror streak camera capable of capturing images at up to 4 Mfps. This camera system consists of 62 independent CCDs

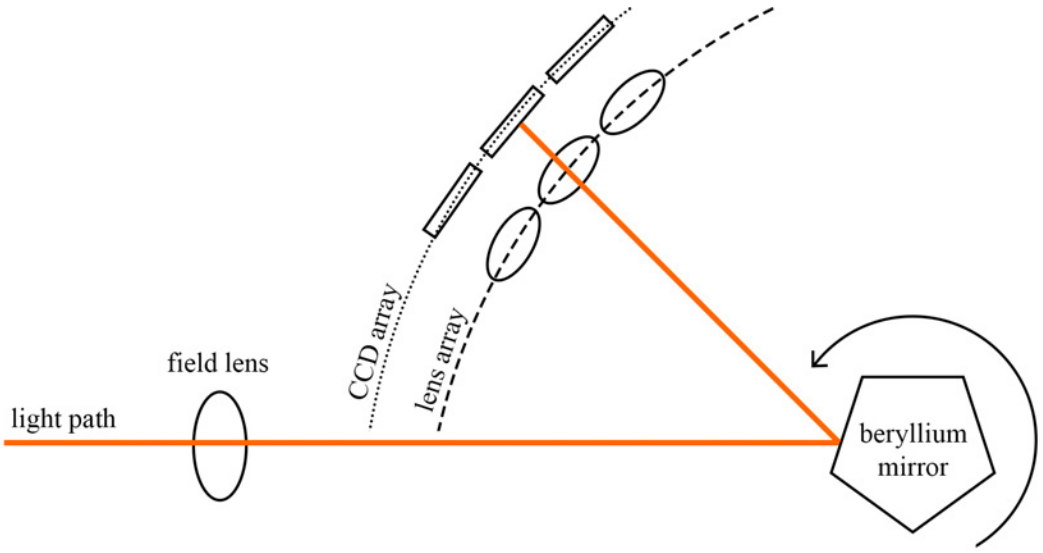

FIGURE 4.12: Simplified schematic showing the operation principle of the Cordin 550-62 rotating mirror camera.

that are positioned in two radial arrays, around a pentagonal beryllium mirror driven by a helium or (nitrogen) gas turbine. Figure 4.12 shows a simplified schematic, in which the light path enters the Cordin 550-62 camera through a Navitar 12x zoom lens and a coupling field lens and streaks across the CCD arrays through a rotating pentagonal beryllium mirror. The image frames thus are captured across 62 consecutive CCDs, at a frame rate proportional to the rotational speed of the mirror. As each image is essentially captured by an individual CCD sensor with a coupling focusing lens, precise positioning adjustment of every CCD is vital to ensure that the images correspond to the same field of view. When this is not present, spatial jitter in the resulting images obtained may arise. This problem has been addressed while conducting this experimental study, and a novel method using an image fiduciary identification method has since been published (Goh et al., 2014a). This is achieved by using a method comprising the identification of the position of the fiduciary signature(s) in the high-speed images, recording of the relative displacements of the fiducial(s) due to image jitter, and the alignment of the images in an image set by compensating for fiduciary displacements. The reader may refer to the publication for better understanding of the image capture

process and this jitter correction method. Results are collected at up to 3 Mfps in this study using helium to drive the gas turbine.

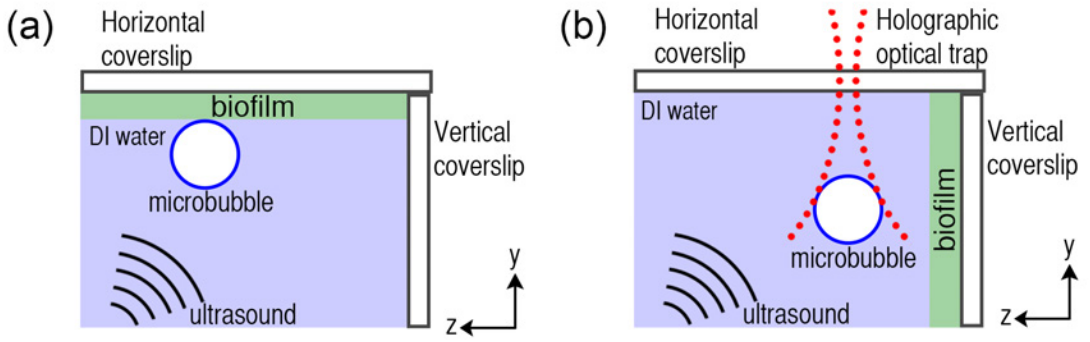

FIGURE 4.13: (a) The two experimental setup configurations in the ultrasound chamber; (a) 24 hr bacterial biofilm on a 22 mm x 22 mm coverslip placed horizontally with buoyant microbubble(s) resting underneath; (b) optically trapped microbubble placed in proximity to a vertical coverslip with 24 hr bacterial biofilm.

The bubbles used in this study are the SonoVue® ultrasound-contrast agent (UCA) microbubbles. The initial radius R_0 of the UCA microbubbles used in the experiments ranges from 1.5 μm to 5 μm. To investigate the interactions of a microbubble under ultrasound excitation near a bacterial biofilm layer, two main experimental setup configurations (Figures 4.13(a) & (b)) are decided. The first configuration involves a bacterial biofilm layer attached under a horizontal coverslip. The UCA microbubble(s) are naturally buoyant and rest underneath the biofilm. Ultrasound is then introduced and high-speed images of this interaction are taken. The holographic optical trap is not used in this case to keep the microbubble(s) in place which are in direct contact with the biofilm. However, it can be used to isolate a microbubble away from any neighbouring bubbles and the vertical coverslip, bringing it more than 20 R_0 away from all other bubbles and the vertical coverslip. As a result, the microbubble is in closest proximity to the rigid horizontal coverslip and thus it could collapse with a liquid jet towards this hard surface, thus disrupting the bacterial biofilm. Under the second configuration (Figure 4.13(b)), a clean horizontal coverslip and a biofilm attached vertical coverslip is

used. Microbubbles are introduced to the ultrasound chamber and positioned in space using an LG optical trap. The bubble is pushed more than 20 R_0 under the horizontal coverslip and other bubbles, then positioned at varying distances away from the biofilm attached vertical coverslip. This distance from center of the UCA microbubble to the vertical coverslip surface in which the biofilm adheres to is defined as the stand-off H. The ultrasound transducer and Cordin 550-62 high-speed camera are synchronized and triggered using the TGA-1242 multi-channel arbitrary waveform generator. The ultrasound is driven in the sinusoidal waveform mode at a single pulse of 50 cycles, at 1.00 MHz or 250 kHz (depending on the transducer in use). The flash unit is synchronized to the Cordin camera and synchronized to be triggered in advance to the high-speed camera exposure.

4.2.2 Results

The results are divided into two main sections according to the configurations of the bacterial biofilm attached coverslip position. When the bacterial biofilm attached coverslip is placed in the horizontal position (Figure 4.13(a)), this configuration allows us to investigate the influence of one or more UCA microbubbles in close contact with the biofilm when triggered with an ultrasound pulse. Section 4.2.2.1 will showcase the results obtained in this configuration. For bacterial biofilm disruption to occur, the proximity of a cavitation bubble to a rigid surface is an important parameter. As a result, our optical trapping rig allows us to position a microbubble in space and at varying distances away from a bacterial biofilm layer. As such, the second configuration refers to placing the biofilm attached coverslip in the vertical position (Figure 4.13(a)) and have an optically trapped microbubble at different distances away from it initially. Ultrasound is then sent to oscillate the microbubble and the extent of biofilm disruption (if any)

with high-speed images collected from the Cordin 550-62 is evaluated and presented in Section 4.2.2.2.

4.2.2.1 Biofilm under horizontal coverslip with bubble(s)

In this section, several cases of one or more microbubbles that are initially quiescent under a bacterial biofilm layer grown on a horizontal glass coverslip will be presented. The results of these cases are evaluated based on high speed image captures of the process of the microbubble(s) under ultrasound excitation, focusing on the biofilm layer to observe the biofilm disruption process (if any). Several parameters could have a bearing on the effect of biofilm disruption. They include the initial microbubble radius R_0, the bacterial biofilm strain, the ultrasound frequency and the ultrasound intensity. Several typical cases with different combinations and variations of these parameters will be presented. Lastly, the effect of several microbubbles in close proximity to each other is investigated and the dynamics of these microbubbles under ultrasound excitation are observed.

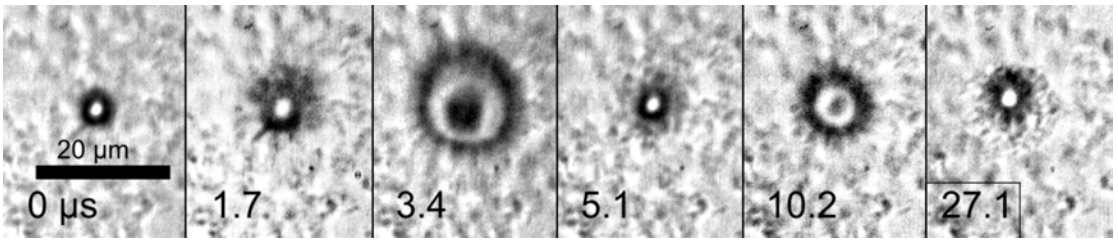

FIGURE 4.14: An UCA microbubble with $R_0 = 2.75$ μm initially resting under a 24 hr. *E. coli* PHL628 biofilm attached to a horizontal coverslip. An ultrasound pulse of 1.00 MHz, 0.7 MPa peak negative pressure (P^-) is applied. This image set is captured at 0.59 Mfps and the respective timings of each image frame is shown at the bottom left hand corner and a 20 μm scale bar is present in the first frame. The bubble oscillates and a liquid jet towards the coverslip is visible at $t = 3.4$ μs.

Figure 4.14 shows the case of an UCA microbubble of $R_0 = 2.75$ μm that is initially resting under a 24 hr. *E. coli* PHL 628 biofilm attached to a horizontal coverslip. The first frame at $t = 0$ μs shows a microbubble in contact with a bacterial biofilm layer

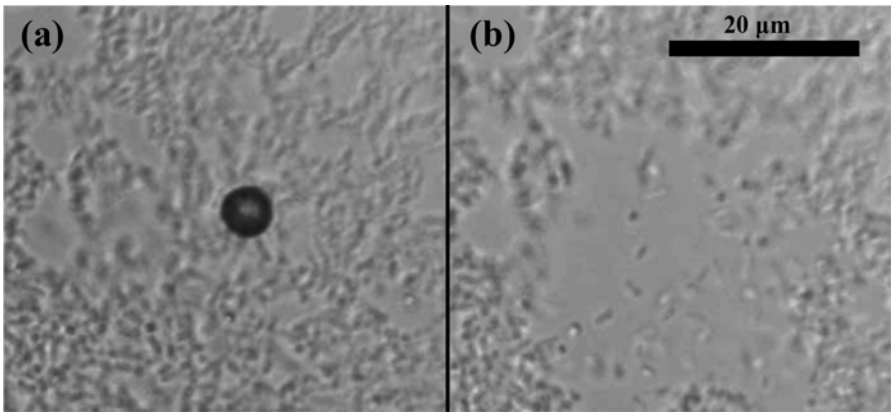

FIGURE 4.15: Screenshot of the microbubble and biofilm in the case of Figure 4.14, (a) before ultrasound exposure; and (b) the same region taken 9 mins after ultrasound exposure. A clearance area of about 30 μm in diameter can be observed where the bubble was resting. A 20 μm scale bar is presented at the top right corner of the figure.

that is in focus. A 50 μs pulse of 1.00 MHz, 0.7 MPa P^- ultrasound is applied and the microbubble expands at $t = 1.7$ μs before collapsing at $t = 3.4$ μs. An image set taken at 0.59 Mfps is presented. The expanding radial shape of the bubble with a darkened core suggests that the microbubble collapse is accompanied with a liquid jet (core) towards the horizontal coverslip, which expands upon impact. The remnants of the bubble are seen to contract at $t = 5.1$ μs before collapsing with a liquid jet towards the coverslip, as shown at around $t = 10.2$ μs. The collapsing liquid jet of the bubble also appears to decrease in intensity, observed from the decreased area of impact. After several cycles of the microbubble oscillations at $t = 27.1$ μs, there is an evident change in the bacterial biofilm integrity, appearing as clumps of cells around the bubble. This could represent the displaced or dislodged bacterial cells in the biofilm due to the repeated bubble collapse jets. To have a better understanding of the effect of the cavitation microbubble on the bacterial biofilm, snapshots from the industrial CCD camera before and after ultrasound exposure and high-speed images capture are captured. Figure 4.15(a) shows a region with the microbubble and the biofilm in the same case as Figure 4.14 before ultrasound exposure, and Figure 4.15(b) shows the same region 9 mins after ultrasound exposure. This shows that there is a localized bacterial biofilm clearance region due to

a cavitating microbubble. A clearance area with a diameter of approximately 30 μm can be observed, centred on the area where the microbubble was initially resting. This shows that the effective clearance area centres around the point of collapse jet impact and is larger than the observed contact area of the oscillating bubbly jets. This is likely because of the biofilm structural integrity in which the neighbouring cells connecting to those in the region directly disturbed by the bubble are also under significant influence.

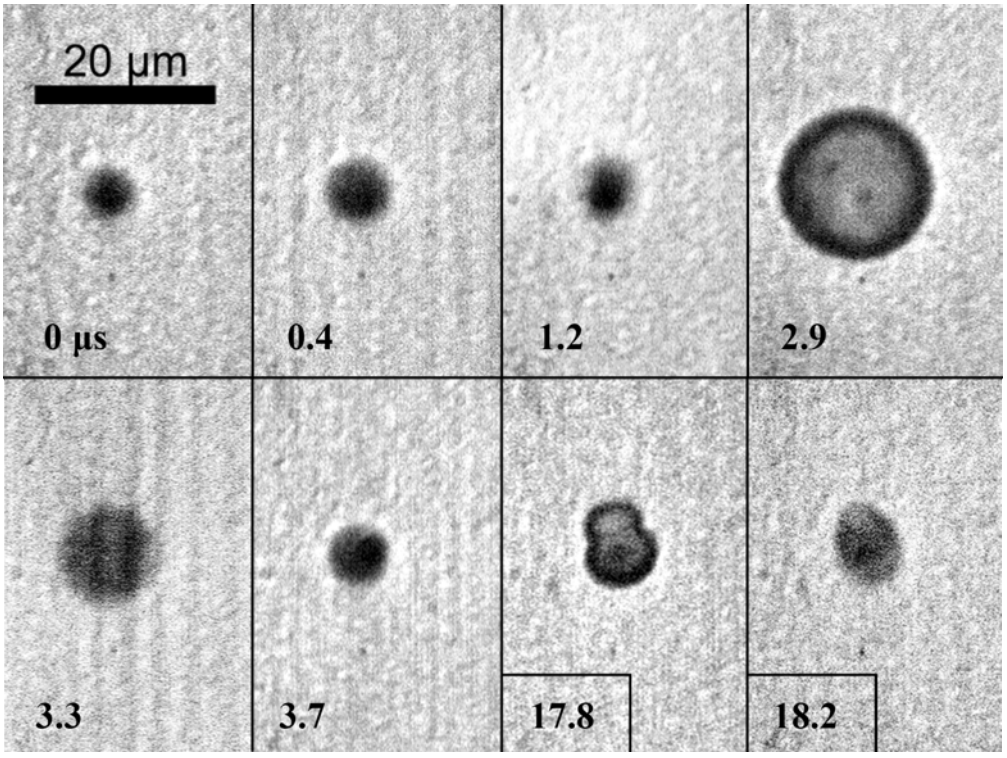

FIGURE 4.16: An UCA microbubble with $R_0 = 2.70$ μm initially resting under a 24 hr. *P. putida* KT2440 biofilm attached to a horizontal coverslip. A 1.00 MHz, 0.7 MPa P^- ultrasound pulse is applied. This image set is captured at 2.42 Mfps and the respective timings of each image frame are shown at the bottom left hand corner and a 20 μm scale bar is present in the first frame. The first few oscillation cycles of the bubble are shown, together with two frames (with their timings boxed out) showing the bubble splitting and collapsing after several more cycles.

In the second case presented in Figure 4.16, we now have a *P. putida* biofilm instead of *E. coli*. A 1.00 MHz, 0.7 MPa P^- ultrasound pulse is applied to a microbubble of R_0 2.70 μm, and an image sequence at 2.42 Mfps is captured. Figure 4.16 shows the first few cycles of the bubble's expansion and collapse. This is noticed to displace neighbouring bacterial cells away and towards the bubble as it expands and collapses respectively.

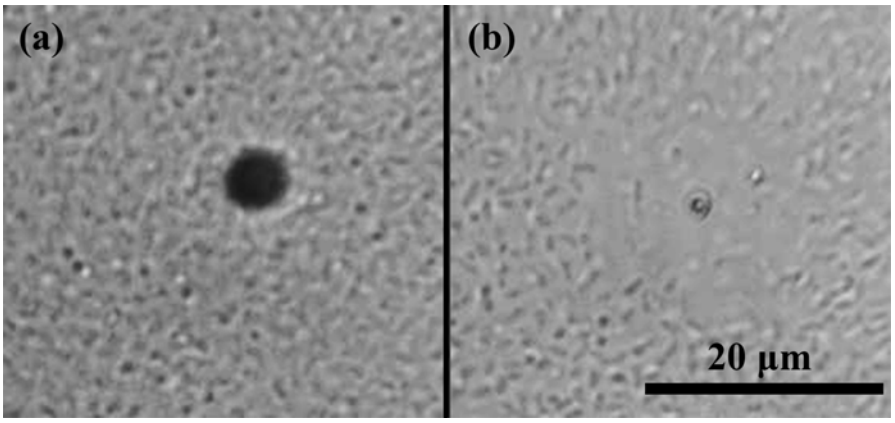

FIGURE 4.17: Screenshot of the microbubble and biofilm in the case of Figure 4.14, (a) before ultrasound exposure; and (b) the same region taken 15 mins after ultrasound exposure. A clearance area of about 18 μm in diameter can be observed where the bubble was resting. A 20 μm scale bar is presented at the bottom right corner of the figure.

However, the plane of focus is not as near to the coverslip surface as in Figure 4.14 and as a result we are unable to notice any liquid jets with the bubble collapses (t = 1.2 μs & 3.7 μs). Nonetheless, marked cell displacements upon the bubble collapse are noticed, which suggests that bubble collapse jets are likely to be present. The last two frames in Figure 4.16 (t = 17.8 μs & 18.2 μs) also highlight that the bubble oscillations belong to a violent process in which the microbubble can collapse into multiple bubbles, or a bubble cloud. These two frames show two resultant microbubbles from the later oscillation cycles, which coalesce as they collapse. Figure 4.17(a) shows the image of the bubble and bacterial biofilm layer before ultrasound exposure, and Figure 4.17(b) shows the same region 15 mins after ultrasound exposure. A clearance region of approximately 18 μm in diameter is observed, similarly centred on where the microbubble was resting initially.

In the last case of a single microbubble resting under a bacterial biofilm layer attached to a horizontal coverslip, 250 kHz ultrasound at 0.5 MPa P^- is applied instead. R_0 = 3.85 μm for the microbubble that is initially quiescent under a 24 hr. *P. putida* KT2440 biofilm on a horizontal coverslip in this case. An image set at 1.54 Mfps is taken and

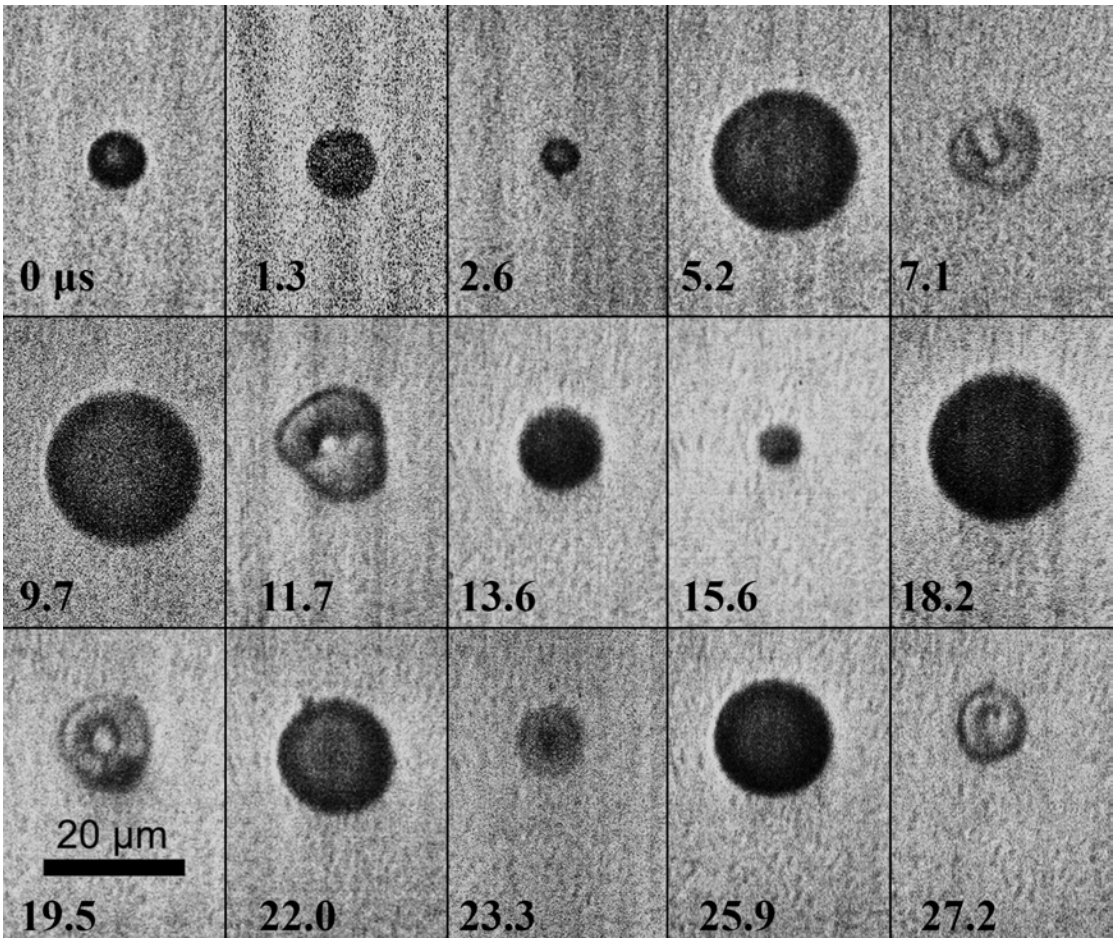

FIGURE 4.18: An UCA microbubble with $R_0 = 3.85$ μm initially resting under a 24 hr. *P. putida* KT2440 biofilm attached to a horizontal coverslip. A 250 kHz, 0.5 MPa P^- ultrasound pulse is applied. This image set is captured at 1.54 Mfps and the respective timings of each image frame are shown at the bottom left hand corner and a 20 μm scale bar is shown in the last frame. The first seven oscillation cycles of the cavitation bubble are shown here (frames with maximum and minimum bubble volumes) and multiple liquid jets towards the coverslip can be seen.

presented as Figure 4.18. Due to the lower ultrasound frequency that is applied, the bubble oscillation period is 4 times as long as the cases with 1 MHz ultrasound. As such, we are able to better capture the bubble shape oscillations and characteristics. The initial several oscillation cycles are presented in Figure 4.18, showing frames with maximum (t = 1.3, 5.2, 9.7, 13.6, 18.2, 22.0 & 25.9 μs) and minimum volumes (t = 2.6, 7.1, 11.7, 15.6, 19.5, 23.3 & 27.2 μs) of the bubble oscillation. Similar to the previous example in Figure 4.16, the bubble can be seen to expand greatly during its oscillation cycle. At t = 9.7 μs, the bubble expanded to a maximum of 2.67 R_0. For the frames showing

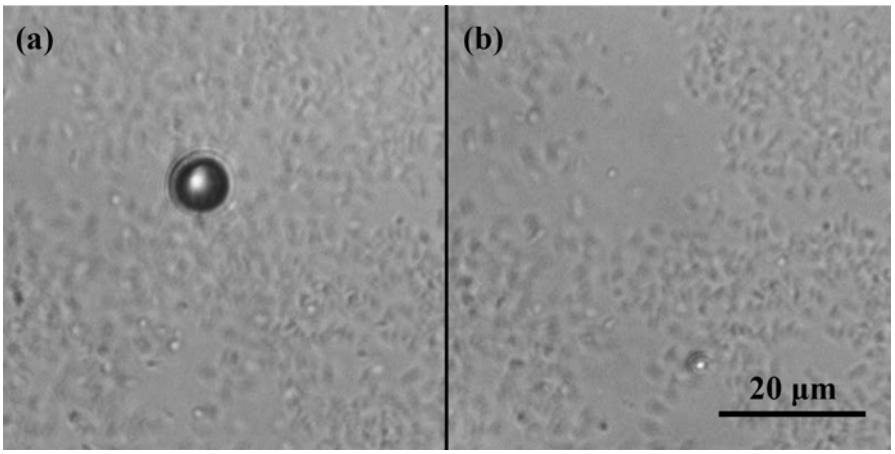

FIGURE 4.19: Screenshot of the microbubble and biofilm in the case of Figure 4.18, (a) before ultrasound exposure; and (b) the same region taken 15 mins after ultrasound exposure. A clearance area of about 19 μm wide and 28 μm long can be observed where the bubble was resting. A 20 μm scale bar is presented at the bottom right corner of the figure.

the bubble collapse, visible jets towards the horizontal coverslip can be observed on the frames at t = 7.1, 11.7, 19.5, 23.3 & 27.2 μs. The extent of the microbubble collapse appears to be correlated to the maximum bubble volume directly before the collapse. For instance, the radial spread of the liquid bubble jet and collapse at t = 11.7 is greater than at t = 27.2 μs. Looking at the adjacent frames just before these collapses, it is evident that the bubble expands to a greater volume at t = 9.7 μs as compared to 25.9 μs. When the microbubble maximum volume during at the end of their expansion phase is smaller, such as the frames at t = 1.3 & 13.6 μs, their corresponding bubble collapse (t = 2.6 & 15.6 μs) are noticed to maintain a spherical profile that does not show any prominent liquid jets. Another interesting observation for this case is that the bubble is observed to traverse up in the frames during its oscillation. It is unclear why the bubble collapses in this direction but a possible explanation is that the horizontal coverslip may not be exactly horizontal in this case and the bubble has the tendency to collapse with a jet towards the rigid surface that it is closest to. Looking at Figure 4.19 which shows the images of the bubble and biofilm before and 15 mins after the ultrasound exposure in this case, an elongated clearance area of around 19 μm wide and 28 μm long can

be seen. This cleared area devoid of bacterial cells also appears to follow the bubble path during its oscillation in Figure 4.18, beginning from the initial bubble position and extends upwards on the image frame.

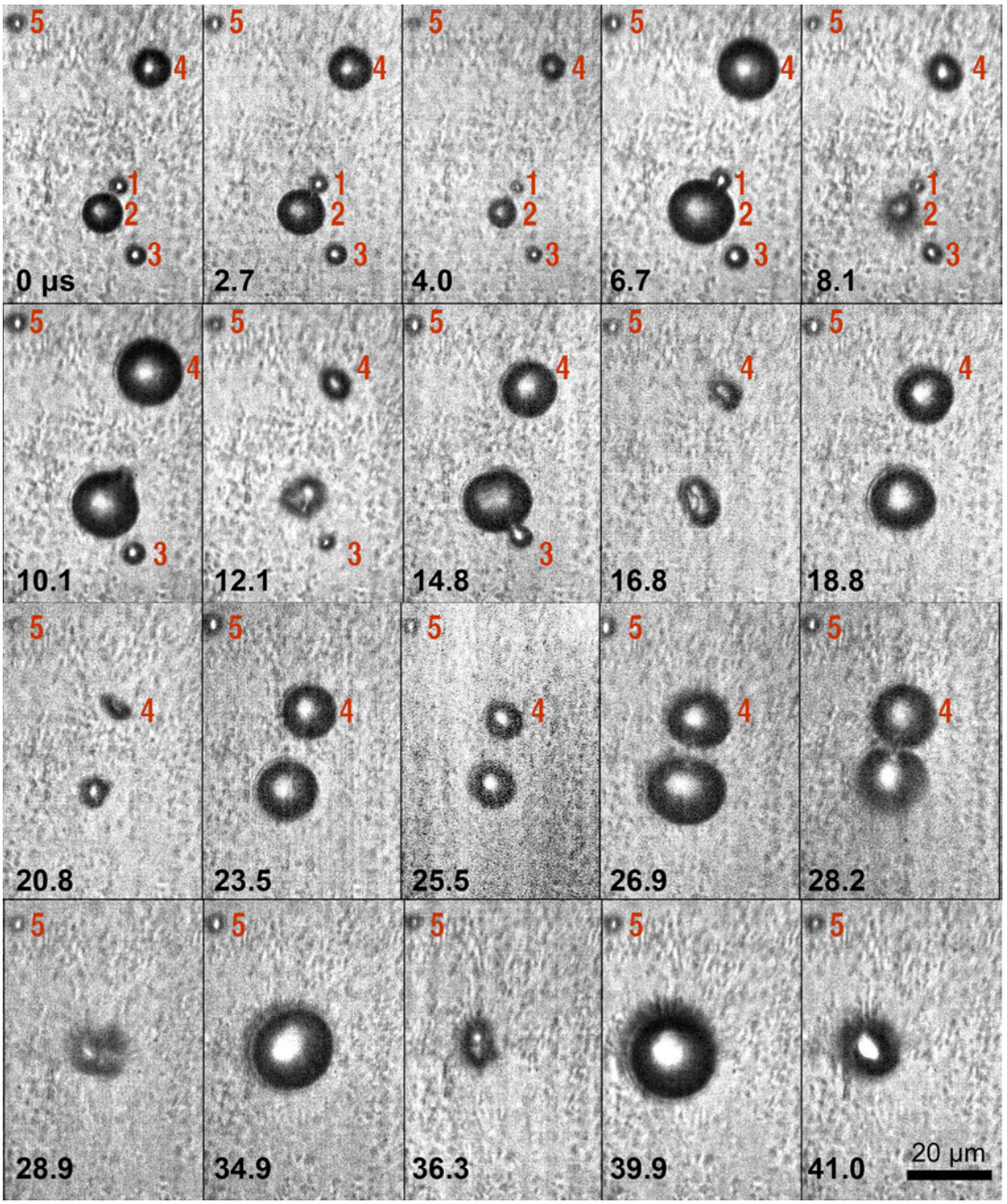

FIGURE 4.20: Multiple UCA microbubbles, of varying dimensions and distances away from one another, are initially resting under a 24 hr. *P. putida* KT2440 biofilm attached to a horizontal coverslip. 250 kHz, 0.7 MPa P^- ultrasound pulse is introduced and some of the microbubbles are noticed to collapse and coalesce while disrupting the bacterial biofilm. The bubbles are labelled '1' to '5' in red. This image set is captured at 1.49 Mfps and the respective timings of each image frame are shown at the bottom left hand corner and a 20 μm scale bar is shown in the last frame.

The previous cases presented are all concerning a single cavitation bubble near a rigid surface with a bacterial biofilm layer. However, such bubbles are likely to be close to other bubbles in practical applications. It is thus important to study the effect of multiple bubble interactions in this setup. Figure 4.20 shows such a case with 5 UCA microbubbles of various sizes under a *P. putida* KT2440 biofilm attached to a horizontal coverslip. The bubbles are labelled '1' to '5' in the image frames, and their respective R_0 are 1.75 μm, 4.20 μm, 2.05 μm, 4.10 μm, and 1.55 μm. A 250 kHz, 0.7 MPa P^- ultrasound pulse is introduced and the bubble dynamics and interactions are captured at 1.49 Mfps. From $t = 0$ μs to 12.1 μs, the bubbles are observed to undergo 3 cycles of oscillations; expanding to their maximum sizes at $t = 2.7$ μs, 6.7 μs & 10.1 μs, and contracting to their minimum volumes at $t = 4.0$ μs, 8.1 μs & 12.1 μs. Bubbles '1' and '2' begin the cycles of oscillation in the closest proximity to each other among the bubbles. At $t = 10.1$ μs and 12.1 μs, they are found to coalesce and merge into a single bubble. At $t = 14.8$ μs, bubble '3' is seen to coalesce with the combined bubble formed by bubble '1' and '2' as the bubbles expand. This merged bubble continues to oscillate until $t = 26.9$ μs while drawing closer with the neighbouring microbubble number '4'. The frames at $t = 28.2$ μs & 28.9 μs show these two bubbles collapsing towards each other, coalescing, and finally emerging as a single bubble as shown at $t =$ 34.9 μs. This collective bubble continues to oscillate around this spot and disrupting the biofilm layer attached to the horizontal coverslip. At $t = 41.0$ μs, a large cleared area in the path of microbubbles '1', '2', '3' & '4' as they oscillate and coalesce with each others can be observed. Throughout this period, bubble '5' is seen to oscillate at the top left hand corner of the frames, expanding and contracting at alternate frames. However, this bubble is furthest away from the rest of the bubbles and does not seem to be influenced by oscillations of other bubbles. This suggests that there appears to be a

minimum distance between the cavitation bubbles, for them to interact with one another during their oscillations. This effect has a relevance to the results of a cavitation bubble with other bubbles in proximity, similar to that presented in Section 3.2 of which the bubble size ratio and stand-off distance between the bubbles are found to be relevant parameters.

4.2.2.2 Biofilm on vertical coverslip with an optically trapped bubble

In this section, several cases of an optically-trapped microbubble near to a biofilm on a vertical coverslip are presented. With this setup configuration, the disruption of bacterial biofilms using microbubbles with ultrasound in an orthogonal view for high-speed imaging to the previous section can be investigated. The use of optical trapping allows us to vary the stand-off distance H, defined as the initial distance between the centre of the bubble and the coverslip surface with biofilm attachment. Typical cases with varying H and also ultrasound parameters are presented.

Figure 4.21 shows the first example in which an optically trapped microbubble of $R_0 = 3.70$ μm is positioned near to a bacterial biofilm attached coverslip, with $H = 24.8$ μm. The *P. putida* KT2440 biofilm has an initial average thickness of 16.7 μm as shown at $t = 0$. 250 kHz, $P^- = 0.7$ MPa ultrasound is introduced in this case, and the image sequence is captured at 1.58 Mfps. At $t = 1.9$ μs, the bubble is seen to expand, before collapsing to its first minimum volume at $t = 3.2$ μs. At $t = 5.7$ μs, the bubble expands drastically to a radius of 14.0 μm. From all the experimental cases captured, it is noticed that the bubble would typically expand and contract slightly in its first cycle, and then grow to a much greater volume at its second (or third) expansion. This expansion is typically accompanied with a violent collapse towards the coverslip in this study. This

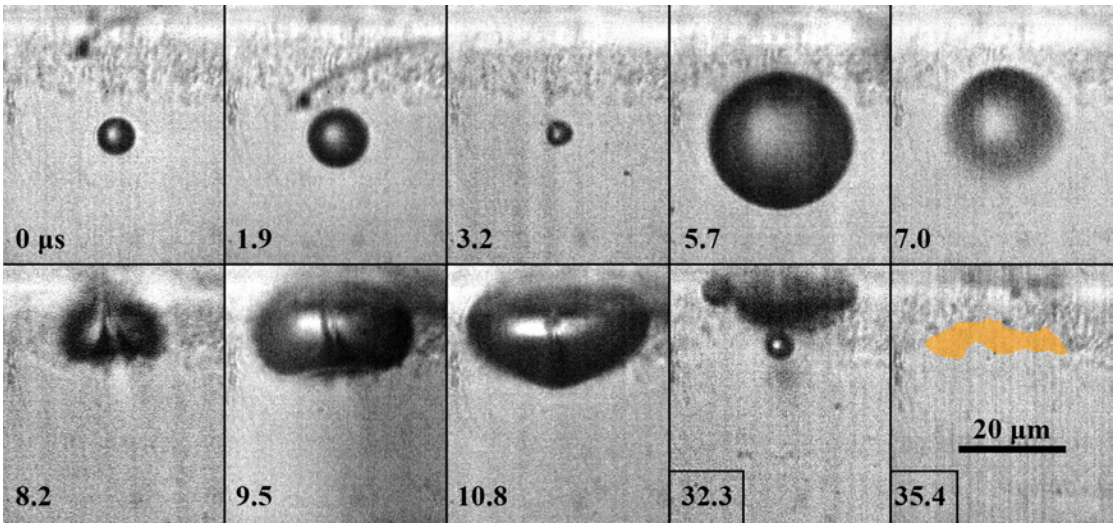

FIGURE 4.21: An UCA microbubble of $R_0 = 3.70$ μm is optically trapped and placed at $H = 24.8$ μm away from a glass coverslip with an attached 24 hr. *P. putida* KT2440 biofilm of initial thickness of 16.7 μm. 250 kHz ultrasound at $P^- = 0.7$ MPa is introduced and the bubbles oscillations are captured at 1.58 Mfps, with respective timings shown in the bottom left hand corner of each frame. R_{max} is 14.0 μm at $t = 5.7$ μs for this case and a distinct liquid jet with the collapse of the bubble can be observed. The bubble jets and oscillations near the coverslip causes a clearance region in the bacterial biofilm. The cross sectional clearance area of the vertical biofilm layer is approximated to be 115 μm^2 in the last frame of the image set, shaded in orange.

observation coincides with other studies that captured the radius-time curve of shelled-microbubbles (Dayton et al., 2001; Santin et al., 2010). As such, R_{max} is defined as the maximum radius of the bubble attained during the first few cycles of its oscillation. In this example, $R_{max} = 14.0$ μm at $t = 5.7$ μs. And with this, the normalized stand-off distance $H' = 1.77$ for this case can be obtained. It is shown at $t = 7.0$ μs & 8.2 μs that the bubble collapses rapidly with a liquid jet through the biofilm layer onto the coverslip surface. The bubble continues to expand with the liquid channel still visible in the bubble core until $t = 10.8$ μs. After several cycles of oscillations, at $t = 32.3$ μs, the bubble has collapsed into a bubbly cloud and migrates out of frame at $t = 35.4$ μs. The biofilm layer is clearly disrupted drastically due to the cavitation bubble. If we compare the last frame ($t = 35.4$ μs) with the initial frame ($t = 0$ μs), this clearance region can be approximated by highlighting the difference in the cross sectional area (top view) of the portion of biofilm in focus. This cleared area (shaded) is estimated to be 115

μm^2. This is by no means an accurate quantitative measure of the clearance zone of the biofilm, since in this case a clearance volume might be more appropriate. However, as due to the inability to obtain an orthogonal view of the coverslip at the same time, this clearance 'area' of the biofilm portion in focus shall act as a rudimentary measure and provide some form of comparison of biofilm disruption among the cases presented here. A 20 μm scale bar is shown in the last frame.

In the following example shown as Figure 4.22, 50 cycles of 1.00 MHz, 0.7 MPa P^- ultrasound is adopted instead. A microbubble of $R_0 = 4.95$ μm is initially placed at $H = 24.9$ μm away from a coverslip with an attached 18.0 μm *E. coli* PHL628 biofilm. Images are captured at 2.00 Mfps for this case and the maximum and minimum volumes of the bubble during its oscillation is shown. In the first few cycles ($t < 4$ μs), the bubble is seen to undergo radial oscillations while translating closer towards the bacterial biofilm layer on the coverslip. R_{max} is found to be 4.40 μm at $t = 4.0$ μs, giving $H' = 2.85$ for this case. At $t = 4.5$ μs, the bubble collapses just next to the biofilm layer and oscillates with an non-spherical bubble shape from this point onwards. At $t = 7.0$, 9.0 & 9.5 μs, the bubble has evidently collapsed into smaller microbubbles that continue to oscillate while close to the biofilm layer. The bubble comes into contact with the vertical coverslip at $t =$ 12.0 μs and continues to expand and collapse towards this surface, through the bacterial biofilm. Though this case does not appear to be as drastic as that of Figure 4.21, biofilm disruption is clearly present. At $t = 25.0$ μs, a clearance region (shaded) of 68 μm^2 can be observed when compared to the frame at $t = 0$ μs.

If the initial stand-off distance H is increased while maintaining other parameters similar, the influence of the rigid surface onto the microbubble oscillations should be lessened. Figure 4.23 shows the case in which an UCA microbubble of $R_0 = 4.00$ μm is placed at $H = 36.3$ μm away from a glass coverslip with a 21.2 μm thick *E. coli* PHL 628 bacterial

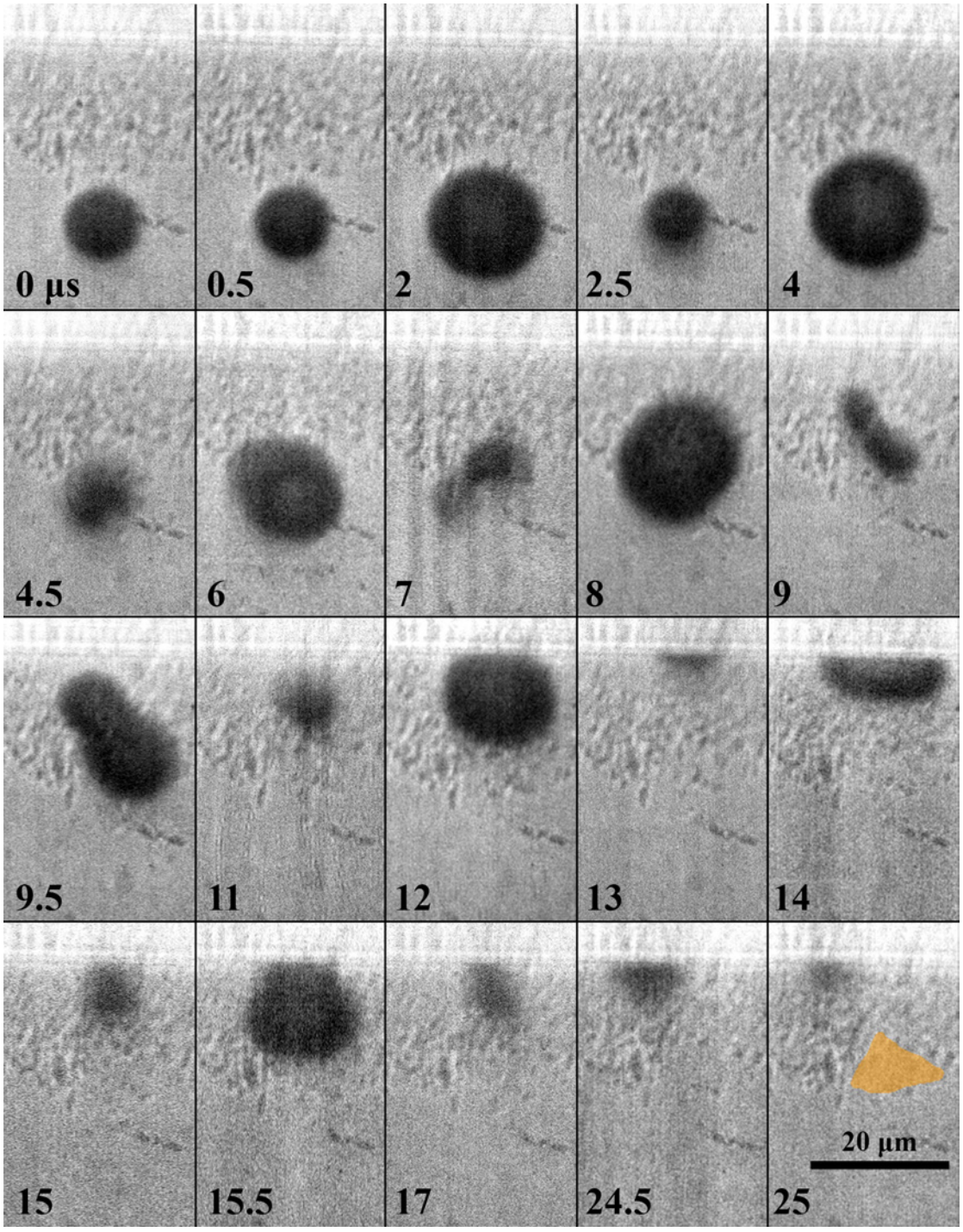

FIGURE 4.22: An UCA microbubble of $R_0 = 4.95$ μm is optically trapped and placed at $H = 24.9$ μm away from a glass coverslip with an attached 24 hr. *E. coli* PHL628 biofilm of initial thickness of 18.0 μm. 1.00 MHz ultrasound at $P^- = 0.7$ MPa is introduced and the bubbles' oscillations are captured at 2.00 Mfps, with respective timings shown in the bottom left hand corner of each frame. R_{max} is found to be 8.80 μm at $t = 4.0$ μs for this case. A clearance region with a cross sectional area (top view) of approximately 68 μm^2 in the bacterial biofilm in the last frame of the image set is shown shaded in orange.

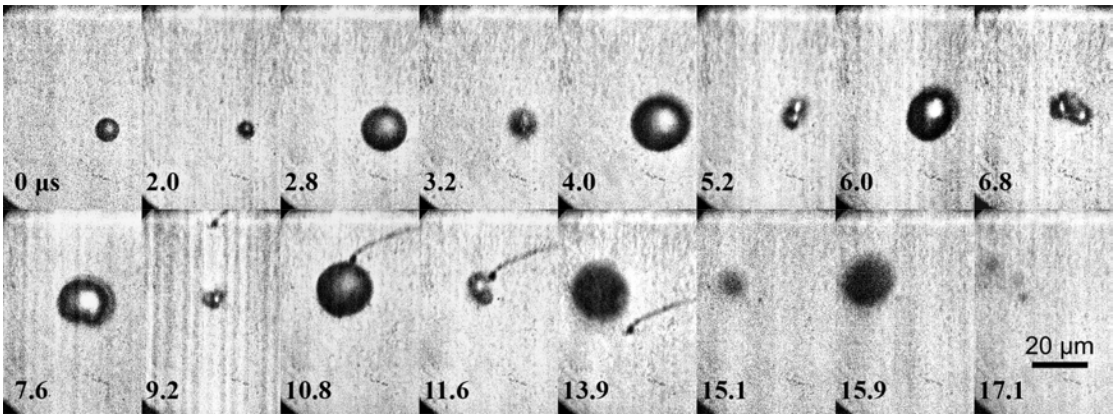

FIGURE 4.23: An UCA microbubble of $R_0 = 4.00$ μm is optically trapped and placed at $H = 36.3$ μm away from a glass coverslip with an attached 24 hr. *E. coli* PHL628 biofilm of initial thickness of 21.1 μm. 1.00 MHz ultrasound at $P^- = 0.7$ MPa is introduced and the bubbles oscillations are captured at 2.06 Mfps, with respective timings shown in the bottom left hand corner of each frame. R_{max} is found to be 8.60 μm at $t = 4.0$ μs for this case. This case shows bubble oscillation towards the biofilm but does not come into close contact with it. Instead, it is seen to oscillate out of focus in the field of view from $t = 13.9$ μs.

biofilm. Images are captured at 2.06 Mfps upon the introduction of 1.00 MHz, $P^- = 0.7$ MPa ultrasound. Similar to the case in Figure 4.22, the first few cycles of the ultrasound are shown to cause the bubble to oscillate radially and traverse towards the coverslip. $R_{max} = 8.60$ μm at $t = 4.0$ μs, giving $H' = 4.24$. The bubble collapses rapidly at $t = 5.2$ μs and re-expands non-spherically at $t = 6.0$ μs. At $t = 6.8$ μs, two small microbubbles can be seen upon the bubble collapse. These bubbles then expand, and coalesce into a collective bubble at $t = 7.6$ μs. From this point onwards, the bubble is near the biofilm surface but it continues to oscillate on the spot, before going out of focus from $t = 13.9$ μs. During these cycles of oscillations, the bubble does not come into contact with the vertical coverslip. Apart from minimal amount of bacterial cells on the outer surface that came in contact with the oscillation microbubble, the bacterial biofilm in this case does not appear to be mechanically disrupted. In other experimental cases conducted with relatively large H', it is noticed that the bubble do not traverse much closer to the biofilm attached coverslip during its oscillation and in some cases does not come into proximity to the biofilm layer. This suggests that there is a limiting H or H' in which

microbubble disruption of bacterial biofilm in this setup can be achieved.

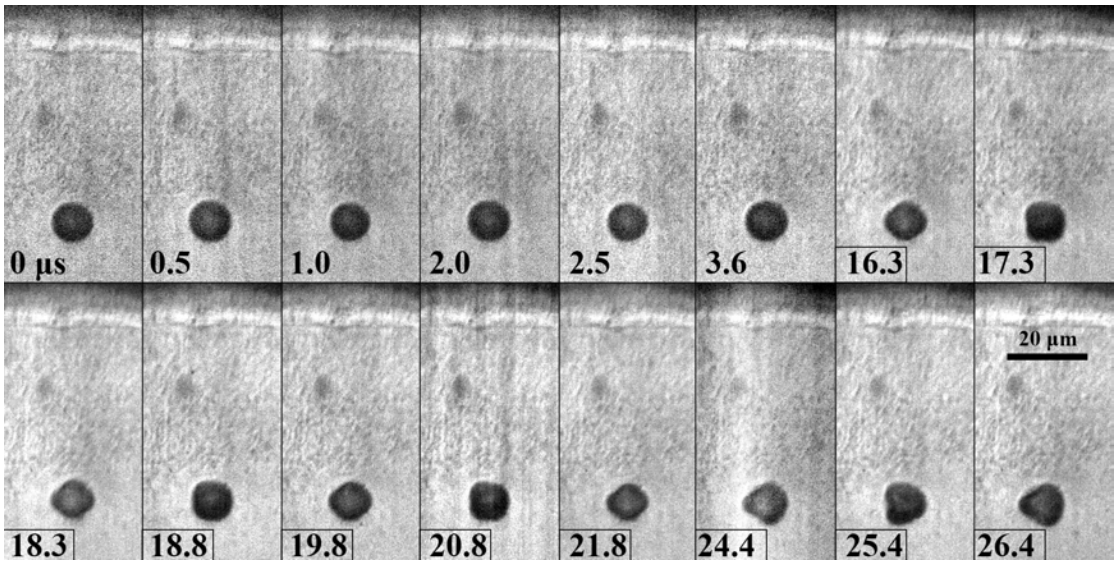

FIGURE 4.24: An UCA microbubble of $R_0 = 5.20$ μm is optically trapped and placed at $H = 43.7$ μm away from a glass coverslip with an attached 24 hr. *P. putida* KT2440 biofilm of initial thickness of 32.5 μm. 1.00 MHz ultrasound at a low P^- of 0.1 MPa is introduced and the bubbles oscillations are captured at 1.97 Mfps, with respective timings shown in the bottom left hand corner of each frame. The bubble is seen to undergo small amplitude oscillations which translates into shape oscillations visible from $t = 16.3$ μs. The bacterial biofilm is not observed to be disrupted in this case.

In the last example (Figure 4.24), the influence of a lower intensity ultrasound that is being applied to the microbubble near a bacterial biofilm layer is investigated. The microbubble has an initial radius $R_0 = 5.20$ μm, and is $H = 43.7$ μm away from a 32.5 μm *P. putida* KT2440 biofilm. A single pulse (50 cycles) of 1 MHz, $P^- = 0.1$ MPa ultrasound is applied and images are recorded at 1.97 Mfps. The bubble is seen to begin small amplitude radial oscillation until $t = 3.6$ μs. Thereafter, the bubble is seen to undergo non-spherical oscillations. This is most prominent as displayed in the frames from $t = 16.3$ μs to $t = 26.4$ μs. Essentially, several modes of cavitation bubble shape oscillations can be observed (Brennen, 1995; Versluis et al., 2010). While this is happening, the bubble does not appear to deviate from its initial position. As a result, there are no observable disruptions on the neighbouring biofilm surface for this case.

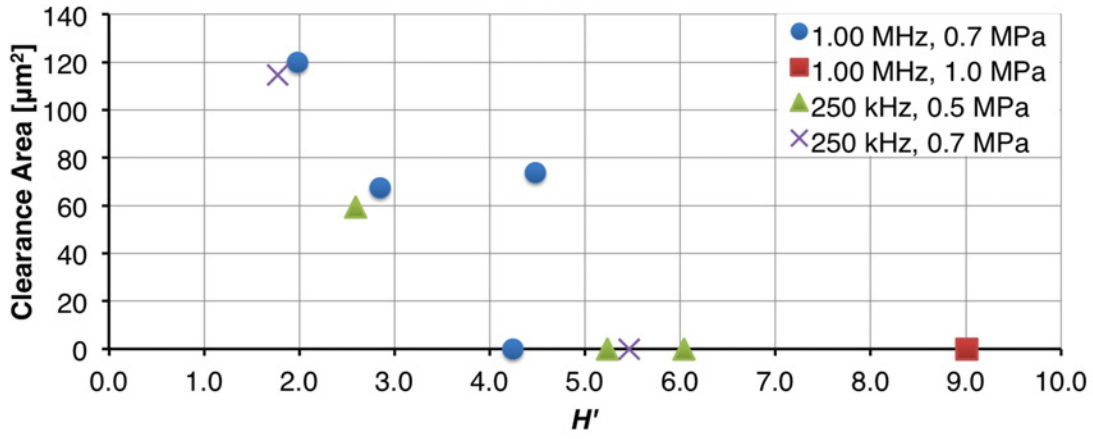

FIGURE 4.25: Graph of bacterial biofilm clearance area [μm^2] against dimensionless stand-off distance H' in the vertical coverslip configuration. The results shown comprise of the experiments conducted with 1.00 MHz (P^- = 0.7 to 1.0 MPa), or 250 kHz (P^- = 0.5 to 0.7 MPa) ultrasound exposure. It appears that H' may be a dominant parameter which would affect the efficacy of bacterial biofilm disruption in this study.

An objective of this experiment is to study the influence of the initial separation distance of a cavitation bubble to a biofilm grown on a rigid surface on the disruption process. Figure 4.25 shows a plot of the dimensionless stand-off distance H' against the approximated clearance area of the attached biofilm on a vertical coverslip obtained by subtracting the cross sectional area of the biofilm in focus from the initial cross sectional area of the biofilm portion in focus. The clearance area approximated from this comparison would only serve as a basic tool to compare the efficacy of biofilm disruption across the experiments conducted, with the assumption that a larger change in the biofilm structure from the top view of the camera corresponds to a greater degree of biofilm disruption. Due to the precise handling required for this setup, the author is only able to obtain some 10 cases that can be discussed in this aspect. Although the sample size is small, we are still able to observe several key aspects of this interaction. Firstly, the clearance area in the cases with smaller H' exceeds that of cases with large H'. Furthermore, when H' is large (> 5), the microbubble oscillations appear to be have little effect on the bacterial biofilm structure. When H' is small, a clearance are of up to 120 μm^2 for a single bubble can be achieved at the low ultrasound intensities

used in this study.

4.2.3 Discussion and Conclusion

The mechanics of ultrasound-targeted microbubble disruption of *E. coli* or *P. putida* bacterial biofilms are investigated by means of high-speed imaging. The first section of the results discusses the dynamics of one or multiple UCA microbubbles that are initially in direct contact with a bacterial biofilm under a horizontal coverslip. In the cases presented, an effective localized clearance of the bacterial biofilm in this configuration is demonstrated. This biofilm disruption effect persists on both *E. coli* and *P. putida* biofilms. The clearance area on *E. coli* biofilms appear to be slightly bigger than that on *P. putida* biofilms. This could be due to *P. putida* being better biofilm formers, possessing better adhesion to solid substrates (Castonguay et al., 2006). Furthermore, biofilm disruption is also present with similarities in bubble behaviour despite the different ultrasound parameters used, i.e. 250 kHz or 1 MHz at $P^- = 0.5$ MPa or 0.7 MPa. There are however noticeable differences in the images obtained, with the 1 MHz cases having bubble images with significant motion blur as compared to the cases with 250 kHz ultrasound due to the much shorter period of oscillation. In several of the cases discussed (Figures 4.14 & 4.18), we see that the microbubble collapses with a liquid jet towards the horizontal coverslip surface. Upon impact, the liquid jet spreads radially and this rapid motion penetrates the biofilm layer and mechanically dislodges cells in the vicinity. Before and after ultrasound snapshots of the biofilm region 'treated' by this procedure is also presented in Figures 4.15, 4.17 & 4.19. This allows us to have a measure of the effective clearance area of bacterial biofilm which is up to 120 μm^2 in the cases presented. They also highlight that this procedure is very localized in the case of a single cavitation bubble, in which the cleared area follows the translation path of

the oscillating bubble. This effect is again realized when we look at multiple cavitation bubbles in contact to a bacterial biofilm in Figure 4.20. When we have multiple cavitation bubbles in close vicinity to each other, it is anticipated that they can collapse with liquid jets or even coalesce. And while this is happening, this will bring about a larger collective clearance area as the bacterial cells are disrupted in the pathways of these oscillating and collapsing microbubbles. This suggests that for practical applications in which multiple bubbles are present, a greater biofilm disruption effect that is localized and targeted can be achieved. Lastly, in the multiple bubble case Figure 4.20, microbubbles of various R_0 are present. It can be noticed that the bubbles with smaller R_0 (1.75 μm, 2.05 μm, & 1.55 μm) respond lesser to the ultrasound waves as compared to the bubbles with initial radius closer to the resonant size (4.20 μm) (Minnaert, 1933; van der Meer et al., 2004). The larger bubbles are observed to have larger amplitude oscillations and collapse more violently. The interactions between the bubbles are alike that observed by Postema et al. (2004), showing bubble oscillation in phase followed by collapse and coalescence. The consolidated bubbles from smaller microbubbles that coalesce also appear to have larger amplitude oscillations with 250 kHz ultrasound. This suggests that the effective radius of the microbubbles may deviate in the ultrasound treatment process due to bubble merging and/or splitting, and should be taken into account for effective applications.

The second configuration shows the biofilm and coverslip in an orthogonal, vertical setting. Holographic optical trapping is also employed to move the bubble away from other surfaces apart from the ones of interest (the biofilm and vertical coverslip). The dimensionless stand-off distance H' is a relative measure of how close the microbubble is to the rigid coverslip surface. For relatively small H', bacterial biofilm disruption is noticed to be present with the bubble oscillating through the biofilm layer and coming into contact

with the coverslip (Figures 4.21 & 4.22). However, at larger H', the bubble moves a shorter distance towards the coverslip and as a result may not contact the coverslip surface at all (Figures 4.23). This suggests that there is an effective dimensionless stand-off distance for a bubble to oscillate violent and/or collapse with a liquid jet towards a rigid surface and disrupt the bacterial biofilm in the process. In the field of bubble dynamics, it is found that a cavitation bubble with H' lesser than approximately 6.0 (Blake et al., 1999; Ohl et al., 1998) is susceptible to a collapse with liquid towards a clean rigid surface. This trend is similar to the results collected in this study, which means that the biofilm layer may not have a strong influence on the bubble dynamics, and the proximity to the neighbouring rigid wall is a dominant influence factor. A case of very low amplitude ultrasound waves (0.1 MPa P^- at 1 MHz) applied to a microbubble near a biofilm layer is also shared. The bubble is shown to undergo low amplitude radial and shape oscillations on the spot, without disrupting the adjacent biofilm layer. This means that there is a P^- threshold in which biofilm disruption is effective. This experimental setup is very complicated and requires precise control in many aspects such as optical trapping and high-speed imaging. One example is the insertion of a visible light mirror (VM1 in Figure 4.11) in order to capture the image with the high-speed camera. The mirror is then aligned by doing relatively low frame rate image captures to ensure correct framing of the region of interest, before the final high-speed image set can be obtained. The 62 frame limitation of the high-speed camera also requires precise synchronization of components such as the flash unit, ultrasound etc. As a result, only a limited number of experimental result sets are obtained. Nonetheless, an experimental plot of biofilm clearance area against H' is drafted (Figure 4.25) for discussion. It seems that the effectiveness of the bacterial biofilm disruption is related to H', with cases conducted with smaller H' clearing more cells. However, for better understanding

of the actual clearance zone in this configuration, the development of a setup which allows orthogonal visualization of the biofilm before and after treatment would be greatly beneficial. Alternatively, fluid dynamics models and simulations should be able to allow for a better understanding of the effects of the key parameters in this study (e.g. H' & P^-) and is another candidate for potential future work.

From the results collected, it appears that this method of using ultrasound and targeted UCA microbubble destruction is a promising method to non-invasively disrupt or treat bacterial biofilm infection on medical implants. The effectiveness of this method can be increased with the use of cell-targeting microbubbles to minimize the stand-off distance between the bubble and the biofilm. Careful selection of microbubble size with resonant frequency that closely matches the ultrasound frequency, as well as the selection of effective ultrasound parameters (frequency, P^-) are also important aspects to maximize the effectiveness of this method. The results show that the cavitation bubble collapse with impinging liquid jet and also micro-streaming shear stresses generated during the bubble oscillations (Marmottant and Hilgenfeldt, 2003) are likely to be the main physical effects that disrupt the biofilm structure. This can be easily complemented with antimicrobial drugs which would now gain better access to the infected site. As the physical mechanisms behind ultrasound-targeted microbubble destruction of biofilms are now identified in this study, different studies of UTMD, such as those by He et al. (2011); Dong et al. (2013); Zhu et al. (2013) can build on this understanding and contribute towards the development of the first clinical biofilm infection treatment procedure using ultrasound.

Chapter 5

Conclusions

5.1 Summary

The studies presented in this thesis are set out to deepen current understanding of cavitation bubble dynamics near to various surfaces, and evaluate the prospective use of cavitation for biomedical applications. The surfaces studied include neighbouring air bubbles, elastic surfaces, and hemispherical air bubble or bacterial biofilm attached to a rigid wall. The bubbles and elastic surfaces are chosen with respect to practical applications, where a cavitation bubble is likely to encounter these surfaces in proximity (multiple bubble setting, biological tissues etc.) and their presence can have a dominant effect on the bubble's dynamics. Some of the surfaces (such as the bubble or biofilm attached to rigid wall) are chosen as they have the potential to solve current problems, and a deeper understanding of the cavitation bubble behaviour near to them acts as a form of feasibility study for future development. An important part of the cavitation bubble behaviour in the current study is the cavitation bubble collapse jet. This liquid jet is widely regarded as one of the key factors responsible for surface damage due to

cavitation. As a result, much of the emphasis of the present work is on the development of these jets, their directions and effect on neighbouring structures.

As the study of cavitation bubbles typically involves many phenomena with complex interactions, it is logical for researchers to combine experimental observations with numerical simulations. The combination of experimental techniques and computational simulations are used to address several key issues and better understand the physics involved in this thesis. Firstly, three experimental studies are presented in Chapter 2. The first study (Section 2.1) deals with a spark-generated cavitation bubble interacting with a finite rubber beam fixed at both ends. It is found from high-speed images that the bubble has a tendency to collapse with a liquid jet towards the rubber beam when the dimensionless stand-off distance H' is relatively low. This corresponds to a downward deflection of the rubber beam as the bubble expands, followed by an upward deflection as the bubble collapses. The magnitude of deflection of the rubber beam acts as a measure of the influence of the cavitation bubble and it is found to decrease with increasing H'. If H' increases to 3.20 and beyond, the bubble is noticed to collapse spherically and there is a lack of upwards deflection of the rubber beam centre. For $H' > 4.8$, the deflections trend suggests that the beam will no longer be deflected due to the bubble. The second study (Section 2.2) involves the prospective prevention of surface damage on a rigid wall by introducing a hemispherical air bubble onto the surface. Several observations can be made by noticing the interaction of a low-voltage spark-discharge cavitation bubble with a rigid plate lined with an initially hemispherical air bubble. Firstly, there appears to be a competing influence between the rigid wall and the air bubble on the dynamics of the cavitation bubble, and an effective H' (< 4.5) range in which jetting from the collapsing cavitation bubble occurs. These jet(s) are also observed to go either towards, away, or both towards and away from the rigid wall. It is found that the dimensionless cavitation

bubble oscillation time T' is the primary parameter that determines the direction of this collapse jet. When $T' > 1.2$, the bubble collapses with a jet directed towards the plate; whereas this jet goes in the direction away from the plate when $T' < 1.0$. For the cases in between these two values, the cavitation bubble collapse appears to have jets directed both towards and away from the stationary bubble. Nevertheless, it is observed that the liquid jet from the collapsing cavitation bubble does not reach the rigid plate surface due to the presence of an attached air bubble. This suggests that it is capable of protecting the rigid boundary from the cavitation bubble collapse jet. The final experimental study (Section 2.3) is an improvement of the low-voltage spark-discharge method used to generate the cavitation bubbles in the above Sections 2.1 & 2.2. A novel circuit involving a MOSFET to trigger the spark-discharge is developed and consistent mm-sized cavitation bubbles can be generated with careful selection of the electrodes. By tweaking some of the setup parameters such as capacitor voltage, electrode dimensions etc., researchers should be able to study cavitation bubbles of various sizes. This should improve future studies involving the low voltage spark-discharge method of generating cavitation bubbles.

Chapter 3 presents two numerical studies of cavitation bubble dynamics, with the use of an axi-symmetrical BEM model discussed in Section 3.1. The first study (Section 3.2) involves the investigation of a liquid jet in a quiescent air bubble due to a neighbouring cavitation bubble. When the bubbles are relatively close to one another initially ($D' < 2.0$), an impending jet develops in the air bubble that subsequently penetrates the bubble in the form of a liquid jet. The velocity of this jet as it penetrates the air bubble is given as u_j. For $D' \geq 2.0$, no such jets where predicted. The bubble size ratio R'_a is another important parameter that determines the outcome of this interaction. u_j is largest for smaller values of ${R_a}'$ and D', and decreases as both parameters increases. A graph of

u_j obtained for different values of D' and ${R_a}'$ is presented as Figure 3.5, which shows influence of the two dominant parameters on the jet velocity. It is found that this liquid jet can reach very high velocities that might cause collateral damage on neighbouring structures. However, it also could be utilized for drug delivery or other applications. The second study (Section 3.3) is an extension of the experimental study conducted in Section 2.2, in which a better understanding of the physics behind the phenomenon of an oscillating bubble near a solid wall with an attached air bubble is attained. The axi-symmetrical BEM model utilizing the 'image' method (Figure 3.9) is developed by me and it achieves very good agreement with the experimental results. It is found that the influence of T' on the cavitation bubble collapse jet direction is a result of the phase difference between the air and cavitation bubble. When two bubbles are in phase, there is a tendency for them to collapse with jets towards each other; whereas if they are out of phase, they tend to collapse with jets away, as reported in Fong et al. (2009); Chew et al. (2011). Pressure contour plots (Figure 3.14) are also generated to allow for visualization of regions of high or low pressure in the fluid domain. This allows for a better understanding of the dominant parameters which influences the direction of the cavitation bubble collapse jet.

Finally Chapter 4 focuses on two studies on prospective biomedical applications of cavitation bubble(s). Section 4.1 presents an experimental study of a cavitation bubble next to a sphere of varying elasticity. This is motivated by the interaction of a cavitation bubble with a neighbouring cell or vesicle, for use in drug delivery or cell identification. Depending on its elasticity, the responses of both the cavitation bubble and the elastic sphere were found to vary. For elastic spheres which are more rigid, there is a tendency for the development of a collapse jet towards the sphere, if the cavitation bubble is relatively close to the elastic sphere initially. Such influence on the cavitation bubble

collapse appears to decrease for a sphere with a smaller elastic modulus, where the bubble tends to oscillate more spherically. These spheres with relatively small elastic moduli are found to undergo much more horizontal elongation and compression (Figure 4.9, up to 50% of its initial span) as compared to stiffer counterparts. The significant disparity in response of both the bubble and 'cell' makes it interesting to develop this study further for potential biomedical applications. The final study in Section 4.2 is a direct observation of ultrasound-targeted microbubble disruption of bacterial biofilms. This is important as the exact mechanisms behind this phenomenon is not fully understood to date. The dynamics of a ultrasound contrast agent microbubble near a rigid surface on which a bacterial biofilm is cultivated for 24 hours, under low-intensity focused ultrasound is captured with a high-speed imaging setup. A holographic optic trapping rig is used to ensure that the cavitation bubble is away from all surfaces apart from the ones of interest. When the bubble cavitates during direct contact to the bacterial biofilm attached to a coverslip, a marked disruption of the biofilm layer is noticed. Distinctive liquid jets that impinge through the biofilm layer onto the rigid wall can also be noticed. This jet is also found to spread radially outwards upon its impact onto the rigid surface. After several cycles of oscillations, a localized clearance zone free of bacterial cells can be observed in the regions of bubble activity. The effectiveness of this disruption seems to be enhanced when multiple microbubbles are introduced with ultrasound. The bubbles are observed to interact with one another, at times coalescing during their oscillation cycles and then oscillate collectively as a larger bubble. This results in a larger clearance zone as compared to the cases of a single oscillating bubble. By placing the rigid wall vertically and create a cavitation bubble horizontally away (by means of applying ultrasound to an UCA microbubble and optical trapping), we am able to investigate the effect of dimensionless stand-off distance H' in this phenomenon. It is found that

the disruption of bacterial biofilm increases with a decrease in H'. Essentially, the use of cavitation bubbles is shown to be effective in mechanically dislodging bacterial cells from the biofilm structure. When coupled with anti-microbial agents, this present a prospective non-invasive treatment method for biofilm infections in medical implants and prostheses.

In conclusion, the studies presented above are consistent in several aspects. For the destructive collapse of a cavitation bubble near to a rigid wall or a inelastic surface, a lower H' suggests the likelihood that a liquid jet towards the surface is present upon the bubble collapse and thus damaging or disrupting the surface to a larger degree. When H' is large (typically more than 5.0), the influence of the surface on the cavitation bubble would diminish and a spherical expansion and collapse of the bubble tends to occur. However, when the cavitation bubble is near to another bubble or a wall-attached bubble, the phase difference between the bubbles becomes important. The direction of collapse jets created are influenced by the oscillation timings of the bubbles. The understanding of these observations and predictions from these studies extends the use of cavitation bubble for a wide range of applications. Furthermore, by careful arrangement of influence surfaces next to a bubble, it should be possible to develop systems in which desired response of the cavitation bubble can be obtained. These responses may include high-speed jet(s), directional jet, surface modification etc. The understanding of the factors presented in this thesis also proves to be vital in the development of biomedical applications which utilize cavitation (of which two prospective areas have been presented in Chapter 4).

5.2 Future Work

The studies of cavitation bubble dynamics in proximity to a variety of surfaces and structures have been presented in this thesis and summarized above. Essentially, the studies conducted have many opportunities for future work and development. Firstly with respect to the experimental and numerical studies conducted, a more comprehensive parametric study can be performed for most of the cases. For instance in Section 2.1, we can investigate the finite rubber beam of various material properties such as elasticity. The rubber beam dimensions, maximum bubble radius, fluid properties etc. could also be varied. However, in terms of a extensive parametric study, it may be more economical for it to be conducted numerically. In that way, a few cases of the experiments can be conducted, which then serve as a validation tool for the numerical solutions. This is akin to Section 3.3 which is conducted to supplement Section 2.2. It would be good if some of the limitations of the numerical model (the influence of the rigid boundary, and shock wave not in the present model) would be addressed. This could shed some insights on the observed wall-attached air bubble's surface perturbations when near a cavitation bubble. Furthermore, a more comprehensive study involving various air bubble shapes, surface properties etc. would be beneficial to gain a deeper understanding of this rather simplified version of a cavitation bubble interaction with a wall-attached air bubble. The consistency of p_v under the new low-voltage spark discharge method introduced in Section 2.3 can also be studied in detail as Section 2.2 & 3.3 have shown the p_v could be an important factor in bubble dynamics problems. As for the interaction of a cavitation bubble with a quiescent air bubble in Section 3.2, future work could include specific utilization of the generated liquid jet. An experimental characterization study of this jet is also of value, if the problem of experimentally 'trapping' a liquid bubble in space can be addressed. One way forward for this is to employ the holographic optical

trapping method (such as the setup in Section 4.2). We can then introduce a cavitation bubble near to an optically trapped air bubble, under the parameters that would induce a high-speed liquid jet away from it. However, please note that this method is limited smaller bubbles (such as microbubbles) which have a lower buoyancy force for the optical trap to counteract.

A second course of action for future work in general would be to incorporate multiple surfaces in different configurations near to a single cavitation bubble. This could include rigid or flexible surfaces, and/or other cavitation or equilibrium bubbles. This may begin with more experimental studies coupled with numerical validations, and then perform a parametric study with better understanding of the physics involved. One of the main observations of a cavitation bubble interaction with multiple surfaces is that the surfaces have competing influences on the bubble, such as a rigid wall and a wall-attached bubble in Sections 2.2 & 3.3. If the surfaces are consistent in their response both in an independent setting or placed with other surfaces, it could be possible to develop a system to predict corresponding response of a neighbouring cavitation bubble with inputs of surface parameters etc. This would greatly reinforce the understanding of cavitation bubbles near to surfaces for practical applications.

Finally, the natural course of action for many of the studies presented would be to translate to actual trials and product conceptualization. As this is the ultimate goal, future work should focus on filling the key gaps in knowledge in order to achieve this. For instance, while it is shown in Section 4.2 the capability of a cavitation bubble to mechanically dislodge bacterial biofilm, there are much opportunities for a more elaborated study and proof of concept before clinical trials can be envisioned. Thankfully, interest in therapeutic ultrasound appears to be the rise in recent years, and should continue to do so. Clinicians can work with scientists and engineers to address key issues that could

hinder the implementation of such technology. Essentially, the road ahead is one that is paved with ideas and opportunities.

Bibliography

Aghdam, A. H., Farhangmehr, V., Ohl, S. W., Khoo, B. C., and Shervani-Tabar, M. T. (2012). Characterization of the interaction of two oscillating bubbles near a thin elastic membrane. *Experiments in Fluids*, 53(6):1723–1735.

Aglyamov, S. R., Karpiouk, A. B., Bourgeois, F., Ben-Yakar, A., and Emelianov, S. Y. (2008). Ultrasound measurements of cavitation bubble radius for femtosecond laser-induced breakdown in water. *Optics Letters*, 33(12):1357–1359.

Alzaraa, A., Gravante, G., Chung, W. Y., Al-Leswas, D., Bruno, M., Dennison, A. R., and Lloyd, D. M. (2012). Targeted microbubbles in the experimental and clinical setting. *The American Journal of Surgery*, 204(3):355–366.

Bartley, J. and Young, D. (2009). Ultrasound as a treatment for chronic rhinosinusitis. *Medical Hypotheses*, 73(1):15–17.

Benjamin, T. B. and Ellis, A. T. (1966). The collapse of cavitation bubbles and the pressures thereby produced against solid boundaries. *Philosophical Transactions of the Royal Society of London. Series A*, 260(1110):221–240.

Biagi, E. and Zanini, A. (1993). Degradation of electromechanical switches submitted to mechanical vibration: Bounce time detection through an automatic measurement system. In *Instrumentation and Measurement Technology Conference, 1993. IMTC/93. Conference Record., IEEE.*

Bigelow, T. A., Northagen, T., Hill, T. M., and C., S. F. (2009). The destruction of Escherichia coli biofilms using high-intensity focused ultrasound. *Ultrasound in Medicine and Biology*, 35(6):1026–1031.

Blake, J. R. and Gibson, D. C. (1981). Growth and collapse of a vapour cavity near a free surface. *Journal of Fluid Mechanics*, 111:123–140.

Blake, J. R. and Gibson, D. C. (1987). Cavitation bubbles near boundaries. *Annual Review of Fluid Mechanics*, 19:99–123.

Blake, J. R., Keen, G. S., Tong, R. P., and Wilson, M. (1999). Acoustic cavitation: the fluid dynamics of non-spherical bubbles. *Philosophical Transactions of the Royal Society of London. Series A*, 357:251–267.

Blake, J. R., Robinson, P. B., Shima, A., and Tomita, Y. (1993). Interaction of two cavitation bubbles with a rigid boundary. *Journal of Fluid Mechanics*, 255:707–721.

Blake, J. R., Taib, B. B., and Doherty, G. (1986). Transient cavities near boundaries. Part 1. Rigid boundary. *Journal of Fluid Mechanics*, 170:479–497.

Blue, J. E. (1967). Resonance of a bubble on an infinite rigid boundary. *The Journal of the Acoustical Society of America*, 41:369–372.

Boudier, T. (1997). Elaboration d'un modéle de deformation pour la detection de contours aux forms complexes. *Innovation and Technology in Biology and Medicine*, 18:1–13.

Bremond, N., Arora, M., Dammer, S. M., and Lohse, D. (2006a). Interaction of cavitation bubbles on a wall. *Physics of Fluids*, 18(12):121505.

Bremond, N., Arora, M., Ohl, C.-D., and Lohse, D. (2006b). Controlled multibubble surface cavitation. *Physical Review Letters*, 96(22):224501.

Brennen, C. E. (1995). *Cavitation and Bubble Dynamics*. Oxford University Press.

Brujan, E.-A., Nahen, K., Schmidt, P., and Vogel, A. (2001a). Dynamics of laser-induced cavitation bubbles near an elastic boundary. *Journal of Fluid Mechanics*, 433:251–282.

Brujan, E.-A., Nahen, K., Schmidt, P., and Vogel, A. (2001b). Dynamics of laser-induced cavitation bubbles near elastic boundaries: influence of the elastic modulus. *Journal of Fluid Mechanics*, 433:283–314.

Buogo, S. and Cannelli, G. B. (2002). Implosion of an underwater spark-generated bubble and acoustic energy evaluation using the Rayleigh model. *The Journal of the Acoustical Society of America*, 111:2594–2600.

Buogo, S., Plocek, J., and Vokurka, K. (2009). Efficiency of energy conversion in underwater spark discharges and associated bubble oscillations: experimental results. *Acta Acustica united with Acustica*, 95:46–59.

Burtsev, V. A. and Shamko, V. V. (1977). Collapse of a spherical cavity, induced by an underwater spark, near a solid wall. *Journal of Applied Mechanics and Technical Physics*, 18:69–76.

Carson, A. R., McTiernan, C. F., Lavery, L., Grata, M., Leng, X., Wang, J., Chen, X., and Villanueva, F. S. (2012). Ultrasound-targeted microbubble destruction to deliver siRNA cancer therapy. *Cancer Research*, 72(23):6191–6199.

Castonguay, M.-H., van der Schaaf, S., Koester, W., Krooneman, J., van der Meer, W., Harmsen, H., and Landini, P. (2006). Biofilm formation by Escherichia coli is stimulated by synergistic interactions and co-adhesion mechanisms with adherence-proficient bacteria. *Research in Microbiology*, 157(5):471–478.

Cerone, P. and Blake, J. R. (1984). A note on the instantaneous streamlines, pathlines and pressure contours for a cavitation bubble near a boundary. *Australian Mathematical Society, Journal, Series B - Applied Mathematics*, 26:31–44.

Chahine, G. L. (1977). Interaction between an oscillating bubble and a free surface. *Journal of Fluids Engineering*, 99:709–716.

Chaussy, C., Brendel, W., and Schmiedt, E. (1980). Extracorporeally induced destruction of kidney stones by shock waves. *Lancet*, 2(8207):1265–1268.

Chaussy, C. G. and Fuchs, G. J. (1989). Current state and future developments of noninvasive treatment of human urinary stones with extracorporeal shock wave lithotripsy. *The Journal of Urology*, 141(3):782–789.

Chen, X. (2004). Optical investigation of cavitation erosion by laser-induced bubble collapse. *Optics and Laser Technology*, 36(3):197–203.

Chew, L. W., Klaseboer, E., Ohl, S.-W., and Khoo, B. C. (2011). Interaction of two differently sized oscillating bubbles in a free field. *Physical Review E*, 84:066307.

Chomas, J. E., Dayton, P., Allen, J., Morgan, K., and Ferrara, K. W. (2001). Mechanisms of contrast agent destruction. *IEEE Transactions on Ultrasonics, Ferroelectrics, and Frequency Control*, 48(1):232–248.

Cole, R. H. (1948). *Underwater Explosions*. Princeton Univ. Press.

Coleman, A. J., Saunders, J. E., Crum, L. A., and Dyson, M. (1987). Acoustic cavitation generated by an extracorporeal shockwave lithotripter. *Ultrasound in Medicine and Biology*, 13(2):69–76.

Costerton, J. W., Ellis, B., Lam, K., Johnson, F., and Khoury, A. E. (1994). Mechanism of electrical enhancement of efficacy of antibiotics in killing biofilm bacteria. *Antimicrobial Agents and Chemotherapy*, 38(12):2803–2809.

Costerton, J. W., Stewart, P. S., and Greenberg, E. P. (1999). Bacterial biofilms: a common cause of persistent infections. *Science*, 284(5418):1318–1322.

Cross, S. E., Jin, Y.-S., Rao, J., and Gimzewski, J. K. (2007). Nanomechanical analysis of cells from cancer patients. *Nature Nanotechnology*, 2(12):780–783.

Crum, L. A. (1988). Cavitation microjets as a contributory mechanism for renal calculi disintegration in ESWL. *The Journal of Urology*, 140(6):1587–1590.

Dayton, P. A., Chomas, J. E., Lum, A. F., Allen, J. S., Lindner, J. R., Simon, S. I., and Ferrara, K. W. (2001). Optical and acoustical dynamics of microbubble contrast agents inside neutrophils. *Biophysical Journal*, 80:1547–1556.

Dijkink, R. and Ohl, C.-D. (2008). Measurement of cavitation induced wall shear stress. *Applied Physics Letters*, 93(25):254107.

Dong, Y., Chen, S., Wang, Z., Peng, N., and Yu, J. (2013). Synergy of ultrasound microbubbles and vancomycin against Staphylococcus epidermidis biofilm. *The Journal of Antimicrobial Chemotherapy*, 68(4):816–826.

Donlan, R. M. (2001). Biofilms and device-associated infections. *Emerging Infectious Diseases*, 7(2):277–281.

Duncan, J. H., Milligan, C. D., and Zhang, S. (1996). On the interaction between a bubble and a submerged compliant structure. *Journal of Sound and Vibration*, 197:17–44.

Duncan, J. H. and Zhang, S. (1991). On the interaction of a collapsing cavity and a compliant wall. *Journal of Fluid Mechanics*, 226:401–423.

Fayzrakhmanova, I. S., Straube, A. V., and Shklyaev, S. (2011). Bubble dynamics atop an oscillating substrate: Interplay of compressibility and contact angle hysteresis. *Physics of Fluids*, 23:102105.

Fong, S. W. (2007). *Cavitation bubble dynamics for biomedical applications*. Ph.D. dissertation, National University of Singapore.

Fong, S. W., Adhikari, D., Klaseboer, E., and Khoo, B. C. (2009). Interactions of multiple spark-generated bubbles with phase differences. *Experiments in Fluids*, 46:705–724.

Fux, C. A., Wilson, S., and Stoodley, P. (2004). Detachment characteristics and oxacillin resistance of Staphyloccocus aureus biofilm emboli in an in vitro catheter infection model. *Journal of Bacteriology*, 186(14):4486–4491.

Garbin, V., Dollet, B., Overvelde, M. L. J., de Jong, N., Lohse, D., Versluis, M., Cojoc, D., Ferrari, E., and Di Fabrizio, E. (2007). Coupled dynamics of an isolated UCA microbubble pair. In *IEEE Ultrasonics Symposium*, pages 757–760.

Gibson, D. C. and Blake, J. R. (1982). The growth and collapse of bubbles near deformable surfaces. *Applied Scientific Research*, 38:215–224.

Goh, B. H. T., Khoo, B. C., McLean, W. H. I., and Campbell, P. A. (2014a). Jitter reduction using native fiducials in rotating mirror ultra-fast microphotography. *Optics Express*, 22(13):16282–16288.

Goh, B. H. T., Oh, Y. D. A., Klaseboer, E., Ohl, S. W., and Khoo, B. C. (2013). A low-voltage spark-discharge method for generation of consistent oscillating bubbles. *Review of Scientific Instruments*, 84(1):014705.

Goh, B. H. T., Ohl, S. W., Klaseboer, E., and Khoo, B. C. (2014b). Jet orientation of a collapsing bubble near a solid wall with an attached air bubble. *Physics of Fluids*, 26:042103.

Gong, S. W., Goh, B. H. T., Ohl, S. W., and Khoo, B. C. (2012). Interaction of a spark-generated bubble with a rubber beam: Numerical and experimental study. *Physical Review E*, 86:026307.

Griffiths, D. J. (1999). *Introduction to Electrodynamics*. Addison Wesley.

Guck, J., Schinkinger, S., Lincoln, B., Wottawah, F., Ebert, S., Romeyke, M., Lenz, D., Erickson, H. M., Ananthakrishnan, R., Mitchell, D., Ks, J., Ulvick, S., and Bilby, C. (2005). Optical deformability as an inherent cell marker for testing malignant transformation and metastatic competence. *Biophysical Journal*, 88(5):36893698.

Guo, S., Khoo, B. C., Teo, S. L. M., and Lee, H. P. (2013). The effect of cavitation bubbles on the removal of juvenile barnacles. *Colloids and Surfaces. B, Biointerfaces*, 109:219–227.

Hall-Stoodley, L., Costerton, J. W., and Stoodley, P. (2004). Bacterial biofilms: from the natural environment to infectious diseases. *Nature Reviews. Microbiology*, 2(2):95–108.

Hall-Stoodley, L. and Stoodley, P. (2009). Evolving concepts in biofilm infections. *Cellular Microbiology*, 11(7):1034–1043.

Harvey, E. N., Barnes, D. K., McElroy, W. D., Whiteley, A. H., Pease, D. C., and Cooper, K. W. (1944). Bubble formation in animals. I, Physical factors. *Journal of Cellular and Comparative Physiology*, 24(1):1–22.

He, N., Hu, J., Liu, H., Zhu, T., Huang, B., Wang, X., Wu, Y., Wang, W., and Qu, D. (2011). Enhancement of vancomycin activity against niofilms by using ultrasound-targeted microbubble destruction. *Antimicrobial Agents and Chemotherapy*, 55(11):5331–5337.

Hebert, C. K., Williams, R. E., Levy, R. S., and Barrack, R. L. (1996). Cost of treating an infected total knee replacement. *Clinical orthopaedics and related research*, 331:140–145.

Hernot, S. and Klibanov, A. L. (2008). Microbubbles in ultrasound-triggered drug and gene delivery. *Advanced Drug Delivery Reviews*, 60(10):1153–1166.

Hochmuth, R. M. (2000). Micropipette aspiration of living cells. *Journal of Biomechanics*, 33(1):15–22.

Hocking, L. M. (1987). The damping of capillary-gravity waves at a rigid boundary. *Journal of Fluid Mechanics*, 179:253–266.

Holt, M. (1977). Underwater explosions. *Annual Review of Fluid Mechanics*, 9:187–214.

Husseini, G. A., Diaz de la Rosa, M. A., Richardson, E. S., Christensen, D. A., and Pitt, W. G. (2005). The role of cavitation in acoustically activated drug delivery. *Journal of Controlled Release*, 107(2):253–261.

Jefferson, K. K., Goldmann, D. A., and Pier, G. B. (2005). Use of confocal microscopy to analyze the rate of vancomycin penetration through Staphylococcus aureus biofilms. *Antimicrobial Agents and Chemotherapy*, 49(6):2467–2473.

Khoo, B. C., Adikhari, D., Fong, S. W., and Klaseboer, E. (2009). Multiple spark-generated bubble interactions. *Modern Physics Letters B*, 23:229–232.

Kiessling, F., Fokong, S., Bzyl, J., Lederle, W., Palmowski, M., and Lammers, T. (2014). Recent advances in molecular, multimodal and theranostic ultrasound imaging. *Advanced Drug Delivery Reviews*, 72:15–27.

Klaseboer, E., Hung, K. C., Wang, C., Wang, C. W., Khoo, B. C., Boyce, P., Debono, S., and Charlier, H. (2005a). Experimental and numerical investigation of the dynamics of an underwater explosion bubble near a resilient/rigid structure. *Journal of Fluid Mechanics*, 537:387–413.

Klaseboer, E. and Khoo, B. C. (2004a). Boundary integral equations as applied to an oscillating bubble near a fluid-fluid interface. *Computational Mechanics*, 33(2):129–138.

Klaseboer, E. and Khoo, B. C. (2004b). An oscillating bubble near an elastic material. *Journal of Applied Physics*, 96(10):5808–5818.

Klaseboer, E. and Khoo, B. C. (2006). A modified Rayleigh-Plesset model for a non-spherically symmetric oscillating bubble with applications to boundary integral methods. *Engineering Analysis with Boundary Elements*, 30:59–71.

Klaseboer, E., Khoo, B. C., and Hung, K. C. (2005b). Dynamics of an oscillating bubble near a floating structure. *Journal of Fluids and Structures*, 21(4):395–412.

Kodama, T. and Tomita, Y. (2000). Cavitation bubble behavior and bubble-shock wave interaction near a gelatin surface as a study of in vivo bubble dynamics. *Applied Physics B: Lasers and Optics*, 70(1):139–149.

Kooiman, K., Foppen-Harteveld, M., van der Steen, A. F. W., and de Jong, N. (2011). Sonoporation of endothelial cells by vibrating targeted microbubbles. *Journal of Controlled Release*, 154:35–41.

Kornfeld, M. and Suvorov, L. (1944). On the destructive action of cavitation. *Journal of Applied Physics*, 15(6):495–506.

Kurihara, E., Hay, T. A., Ilinskii, Y. A., Zabolotskaya, E. A., and Hamilton, M. F. (2011). Model for the dynamics of two interacting axisymmetric spherical bubbles undergoing small shape oscillations. *The Journal of the Acoustical Society of America*, 130(5):3357–3369.

Lauterborn, W. (1982). Cavitation bubble dynamics - new tools for an intricate problem. *Applied Scientific Research*, 38:165–178.

Lauterborn, W. and Bolle, H. (1975). Experimental investigations of cavitation-bubble collapse in the neighbourhood of a solid boundary. *Journal of Fluid Mechanics*, 72:391–399.

Lauterborn, W. and Hentschel, W. (1985). Cavitation bubble dynamics studied by high speed photography and holography: part one. *Ultrasonics*, 23(6):260268.

Lauterborn, W. and Kurz, T. (2010). Physics of bubble oscillations. *Reports on Progress in Physics*, 73:106501.

Le Gac, S., Zwaan, E., van den Berg, A., and Ohl, C.-D. (2007). Sonoporation of suspension cells with a single cavitation bubble in a microfluidic confinement. *Lab on a Chip*, 7(12):1666–1672.

Lenz, A. P., Williamson, K. S., Pitts, B., Stewart, P. S., and Franklin, M. J. (2008). Localized gene expression in Pseudomonas aeruginosa biofilms. *Applied and Environmental Microbiology*, 74(14):4463–4471.

Lew, K. S. F., Klaseboer, E., and Khoo, B. C. (2007). A collapsing bubble-induced micropump: An experimental study. *Sensors and Actuators A: Physical*, 133:161–172.

Liang, H.-D., Tang, J., and Halliwell, M. (2010). Sonoporation, drug delivery, and gene therapy. *Proceedings of the Institution of Mechanical Engineers, Part H: Journal of Engineering in Medicine*, 224(2):343–361.

Lu, X., Pan, Y., Liu, K., Liu, M., and Zhang, H. (2002). Spark model of pulsed discharge in water. *Journal of Applied Physics*, 91:24–31.

Lynch, A. S. and Robertson, G. T. (2008). Bacterial and fungal biofilm infections. *Annual Review of Medicine*, 59(1):415–428.

Mackersie, J. W., Timoshkin, I. V., and MacGregor, S. J. (2005). Generation of high-power ultrasound by spark discharges in water. *IEEE Transactions on Plasma Science*, 33:1715–1724.

Marmottant, P. and Hilgenfeldt, S. (2003). Controlled vesicle deformation and lysis by single oscillating bubbles. *Nature*, 423:153–156.

Martínez-Gil, M., Yousef-Coronado, F., and Espinosa-Urgel, M. (2010). LapF, the second largest Pseudomonas putida protein, contributes to plant root colonization and determines biofilm architecture. *Molecular Microbiology*, 77(3):549–561.

Matthews, P. C., Berendt, A. R., McNally, M. A., and Byren, I. (2009). Diagnosis and management of prosthetic joint infection. *BMJ*, 338:1378–1383.

McLeod, B. R., Fortun, S., Costerton, J. W., and Stewart, P. S. (1999). Enhanced bacterial biofilm control using electromagnetic fields in combination with antibiotics. *Methods in Enzymology*, 310:656–670.

Minnaert, M. (1933). On musical air-bubbles and the sounds of running water. *Philosophical Magazine Series 7*, 16:235–248.

Naude, C. F. and Ellis, A. T. (1961). On the mechanism of cavitation damage by nonhemispherical cavities collapsing in contact with a solid boundary. *Trans. ASME Journal of Basic Engineering*, 83:648–656.

Nishikawa, T., Yoshida, A., Khanal, A., Habu, M., Yoshioka, I., Toyoshima, K., Takehara, T., Nishihara, T., Tachibana, K., and Tominaga, K. (2010). A study of the efficacy of ultrasonic waves in removing biofilms. *Gerodontology*, 27(3):199–206.

Ohl, C.-D. (2010). Aiming with bubbles. *Physics*, 3:65.

Ohl, C.-D., Arora, M., Ikink, R., de Jong, N., Versluis, M., Delius, M., and Lohse, D. (2006). Sonoporation from jetting cavitation bubbles. *Biophysical Journal*, 91:4285–4295.

Ohl, C.-D., Kurz, T., Geisler, R., Lindau, O., and Lauterborn, W. (1999). Bubble dynamics, shock waves and sonoluminescence. *Philosophical Transactions of the Royal Society of London. Series A*, 357:269–294.

Ohl, C.-D., Lindau, O., and Lauterborn, W. (1998). Luminescence from spherically and asphericallly collapsing laser induced bubbles. *Physical Review Letters*, 80:393–396.

Ohl, C.-D., Philipp, A., and Lauterborn, W. (1995). Cavitation bubble collapse studied at 20 million frames per second. *Annalen der Physik*, 507(1):26–34.

Ohl, S.-W., Klaseboer, E., and Khoo, B. C. (2009). The dynamics of a non-equilibrium bubble near bio-materials. *Physics in Medicine and Biology*, 54:6313–6336.

Ohl, S.-W., Klaseboer, E., and Khoo, B. C. (2010). The dynamics of an oscillating bubble near bio-materials. *Modern Physics Letters B*, 24:1365–1368.

Pain, A., Goh, B. H. T., Klaseboer, E., Ohl, S.-W., and Khoo, B. C. (2012). Jets in quiescent bubbles caused by a nearby oscillating bubble. *Journal of Applied Physics*, 111:054912.

Parini, M. R. and Pitt, W. G. (2006). Dynamic removal of oral biofilms by bubbles. *Colloids and Surfaces B: Biointerfaces*, 52(1):39–46.

Parsons, C. A. (1906). The steam turbine on land and at sea. *Lecture to the Royal Institution, London.*

Pearle, M. S., Calhoun, E. A., and Curhan, G. C. (2005). Urologic diseases in America project: urolithiasis. *The Journal of Urology*, 173(3):848–857.

Pearson, A. (2004). Bubble interactions near a free surface. *Engineering Analysis with Boundary Elements*, 28(4):295–313.

Pelekasis, N. A. and Tsamopoulos, J. A. (1993a). Bjerknes forces between two bubbles. Part 1. Response to a step change in pressure. *Journal of Fluid Mechanics*, 254:467–499.

Pelekasis, N. A. and Tsamopoulos, J. A. (1993b). Bjerknes forces between two bubbles. Part 2. Response to an oscillatory pressure field. *Journal of Fluid Mechanics*, 254:501–527.

Pishchalnikov, Y. A., Sapozhnikov, O. A., Bailey, M. R., Williams, J. C. J., Cleveland, R. O., Colonius, T., Crum, L. A., Evan, A. P., and McAteer, J. A. (2003). Cavitation bubble cluster activity in the breakage of kidney stones by lithotripter shock waves. *Journal of Endourology*, 17(7):435–446.

Pitt, W. G., Husseini, G. A., and Staples, B. J. (2004). Ultrasonic drug delivery: a general review. *Expert Opinion on Drug Delivery*, 1(1):37–56.

Pitt, W. G., McBride, M. O., Lunceford, J. K., Roper, R. J., and Sagers, R. D. (1994). Ultrasonic enhancement of antibiotic action on gram-negative bacteria. *Antimicrobial Agents and Chemotherapy*, 38(11):2577–2582.

Plesset, M. S. (1949). The dynamics of cavitation bubbles. *ASME Journal of Applied Mechanics*, 16:228–231.

Plesset, M. S. and Chapman, R. B. (1971). Collapse of an initially spherical vapour cavity in the neighbourhood of a solid boundary. *Journal of Fluid Mechanics*, 47:283–290.

Postema, M., van Wamel, A., Lance, C. T., and de Jong, N. (2004). Ultrasound-induced encapsulated microbubble phenomena. *Ultrasound in Medicine and Biology*, 30(6):827–840.

Prentice, P., Cuschieri, A., Dholakia, K., Prausnitz, M., and Campbell, P. (2005). Membrane disruption by optically controlled microbubble cavitation. *Nature Physics*, 1(2):107–110.

Prosperetti, A. (1982). Bubble dynamics: a review and some recent results. *Applied Scientific Research*, 38(1):145–164.

Qin, S., Caskey, C. F., and Ferrara, K. W. (2009). Ultrasound contrast microbubbles in imaging and therapy: physical principles and engineering. *Physics in Medicine and Biology*, 54(6):27–57.

Rayleigh, L. (1917). On the pressure developed in a liquid during the collapse of a spherical cavity. *Philosophical Magazine Series 6*, 34(200):94–98.

Razavi, A., Clement, D., Fowler, R. A., Birer, A., Chavrier, F., Mestas, J. L., Romano, F., Chapelon, J. Y., Bgl, A., and Lafon, C. (2014). Contribution of inertial cavitation in the enhancement of in vitro transscleral drug delivery. *Ultrasound in Medicine and Biology*, 40(6):1216–1227.

Reisner, A., Haagensen, J. A. J., Schembri, M. A., Zechner, E. L., and Molin, S. (2003). Development and maturation of Escherichia coli K-12 biofilms. *Molecular Microbiology*, 48(4):933–946.

Robinson, P. B., Blake, J. R., Kodama, T., Shima, A., and Tomita, Y. (2001). Interaction of cavitation bubbles with a free surface. *Journal of Applied Physics*, 89:8225–8237.

Rodriguez, F., Patel, S. K., and Cohen, C. (1990). Measuring the modulus of a sphere by squeezing between parallel plates. *Journal of Applied Polymer Science*, 40(12):285–295.

Römling, U. and Balsalobre, C. (2012). Biofilm infections, their resilience to therapy and innovative treatment strategies. *Journal of Internal Medicine*, 272(6):541–561.

Rungsiyaphornrat, S., Klaseboer, E., Khoo, B. C., and Yeo, K. S. (2003). The merging of two gaseous bubbles with an application to underwater explosions. *Computers and Fluids*, 32:1049–1074.

Sankin, G., Yuan, F., and Zhong, P. (2010). Pulsating tandem microbubble for localized and directional single-cell membrane poration. *Physical Review Letters*, 105(7):078101.

Santin, M. D., King, D. A., Foiret, J., Haak, A., O'Brien Jr., W. D., and Bridal, S. L. (2010). Encapsulated contrast microbubble radial oscillation associated with postexcitation pressure peaks. *The Journal of the Acoustical Society of America*, 127(2):1156–1164.

Shaw, S. J., Jin, Y. H., Gentry, T. P., and Emmony, D. C. (1999). Experimental observations of the interaction of a laser generated cavitation bubble with a flexible membrane. *Physics of Fluids*, 11:2437–2439.

Shima, A. and Nakajima, K. (1977). The collapse of a non-hemispherical bubble attached to a solid wall. *Journal of Fluid Mechanics*, 80:369–391.

Shima, A. and Sato, Y. (1979). The collapse of a bubble attached to a solid wall. *Ingenieur-Archiv*, 48:85–95.

Shima, A. and Tomita, Y. (1981). The behavior of a spherical bubble near a solid wall in a compressible liquid. *Archive of Applied Mechanics*, 51:243–255.

Shima, A., Tomita, Y., Gibson, D. C., and Blake, J. R. (1989). The growth and collapse of cavitation bubbles near composite surfaces. *Journal of Fluid Mechanics*, 203:199–214.

Sirsi, S. R. and Borden, M. A. (2012). Advances in ultrasound mediated gene therapy using microbubble contrast agents. *Theranostics*, 2(12):1208–1222.

Sivakumar, M., Tang, S. Y., and Tan, K. W. (2014). Cavitation technology - a greener processing technique for the generation of pharmaceutical nanoemulsions. *Ultrasonics Sonochemistry*, 21(6):2069–2083.

Sleep, J., Wilson, D., Simmons, R., and Gratzer, W. (1999). Elasticity of the red cell membrane and its relation to hemolytic disorders: an optical tweezers study. *Biophysical Journal*, 77:3085–3095.

Smith, R. H. and Mesler, R. B. (1972). A photographic study of the effect of an air bubble on the growth and collapse of a vapor bubble near a surface. *Journal of Fluids Engineering*, 94:933–940.

Soh, W. K. (1990). High-speed photographic study of a cavitation bubble. In Fuller, P. W. W., editor, *SPIE 1358, 19th Intl Congress on High-Speed Photography and Photonics*, pages 1011–1015.

Stride, E. and Saffari, N. (2003a). Microbubble ultrasound contrast agents: a review. *Proceedings of the Institution of Mechanical Engineers. Part H, Journal of Engineering in Medicine.*, 217(6):429–447.

Stride, E. and Saffari, N. (2003b). On the destruction of microbubble ultrasound contrast agents. *Ultrasound in Medicine and Biology*, 29(4):563–573.

Suresh, S. (2007). Biomechanics and biophysics of cancer cells. *Acta Biomaterialia*, 3:413–438.

Sutherland, I. (2001). Biofilm exopolysaccharides: a strong and sticky framework. *Microbiology*, 147(1):3–9.

Tandiono, T., Klaseboer, E., Ohl, S.-W., Ow, D. S.-W., Choo, A. B.-H., Li, F., and Ohl, C.-D. (2013). Resonant stretching of cells and other elastic objects from transient cavitation. *Soft Matter*, 9:8687–8696.

Tao, N. J., Lindsay, S. M., and Lees, S. (2000). Measuring the microelastic properties of biological material. *Biophysical Journal*, 63:1165–1169.

Tho, P., Manasseh, R., and Ooi, A. (2007). Cavitation microstreaming patterns in single and multiple bubble systems. *Journal of Fluid Mechanics*, 576:191–233.

Timm, E. F. and Hammit, F. G. (1971). Bubble collapse adjacent to a rigid wall, a flexible wall, and a second bubble. *ASME Cavitation Forum*, pages 18–20.

Tomita, Y. and Kodama, T. (2003). Interaction of laser-induced cavitation bubbles with composite surfaces. *Journal of Applied Physics*, 94:2809–2816.

Tomita, Y., Kodama, T., and Shima, A. (1991). Secondary cavitation due to interaction of a collapsing bubble with a rising free surface. *Applied Physics Letters*, 59(3):274–276.

Tomita, Y. and Shima, A. (1986). Mechanisms of impulsive pressure generation and damage pit formation by bubble collapse. *Journal of Fluid Mechanics*, 169:535–564.

Tomita, Y., Shima, A., and Sato, K. (1990). Dynamic behavior of two-laser-induced bubbles in water. *Applied Physics Letters*, 57(3):234–236.

Tong, R. P. (1997). A new approach to modelling an unsteady free surface in boundary integral methods with application to bubble-structure interactions. *Mathematics and Computers in Simulation*, 44:415–426.

Tong, R. P., Schiffers, W. P., Shaw, S. J., Blake, J. R., and Emmony, D. C. (1999). The role of 'splashing' in the collapse of a laser-generated cavity near a rigid boundary. *Journal of Fluid Mechanics*, 380:339–361.

Trampuz, A., Osmon, D. R., Hanssen, A. D., Steckelberg, J. M., and Patel, R. (2003). Molecular and antibiofilm approaches to prosthetic joint infection. *Clinical Orthopaedics and Related Research*, 414:69–88.

Trampuz, A. and Zimmerli, W. (2005). Prosthetic joint infections: update in diagnosis and treatment. *Swiss Medical Weekly*, 135:243–251.

Turangan, C. K., Ong, G. P., Klaseboer, E., and Khoo, B. C. (2006). Experimental and numerical study of transient bubble-elastic membrane interaction. *Journal of Applied Physics*, 100(5):054910.

Tzanakis, I., Eskin, D. G., Georgoulas, A., and Fytanidis, D. K. (2014). Incubation pit analysis and calculation of the hydrodynamic impact pressure from the implosion of an acoustic cavitation bubble. *Ultrasonics Sonochemistry*, 21(2):866–878.

Unger, E., Porter, T., Lindner, J., and Grayburn, P. (2014). Cardiovascular drug delivery with ultrasound and microbubbles. *Advanced Drug Delivery Reviews*, 72:110–126.

Unger, E. C., Porter, T., Culp, W., Labell, R., Matsunaga, T., and Zutshi, R. (2004). Therapeutic applications of lipid-coated microbubbles. *Advanced drug delivery reviews*, 56(9):1291–1314.

van der Meer, S. M., Versluis, M., Lohse, D., Chin, C. T., Bouakaz, A., and de Jong, N. (2004). The resonance frequency of SonoVue® as observed by high-speed optical imaging. In *Ultrasonics Symposium, 2004 IEEE*, volume 1, pages 343–345.

Versluis, M., Goertz, D. E., Palanchon, P., Heitman, I. L., van der Meer, S. M., Dollet, B., de Jong, N., and Lohse, D. (2010). Microbubble shape oscillations excited through ultrasonic parametric driving. *Physical Review E*, 82:026321.

Versluis, M., Schmitz, B., von der Heydt, A., and Lohse, D. (2000). How snapping shrimp snap: through cavitating bubbles. *Science*, 289:2114–2117.

Vogel, A., Lauterborn, W., and Timm, R. (1988). Optical and acoustic investigations of the dynamics of laser-produced cavitation bubbles near a solid boundary. *Journal of Fluid Mechanics*, 209:299–338.

Walters III, M. C., Roe, F., Bugnicourt, A., Franklin, M. J., and S., S. P. (2003). Contributions of antibiotic penetration, oxygen limitation, and low metabolic activity to tolerance of Pseudomonas aeruginosa biofilms to ciprofloxacin and tobramycin. *Antimicrobial Agents and Chemotherapy*, 47(1):317–323.

Wang, C., Khoo, B. C., and Yeo, K. S. (2003). Elastic mesh technique for 3D BIM simulation with an application to underwater explosion bubble dynamics. *Journal of Fluid Mechanics*, 32(9):1195–1212.

Wang, N., Butler, J. P., and Ingber, D. E. (1993). Mechanotransduction across the cell surface and through the cytoskeleton. *Science*, 260(5111):1124–1127.

Wang, Q. X., Yeo, K. S., Khoo, B. C., and Lam, K. Y. (1996a). Nonlinear interaction between gas bubble and free surface. *Computers and Fluids*, 25(7):607–628.

Wang, Q. X., Yeo, K. S., Khoo, B. C., and Lam, K. Y. (1996b). Strong interaction between a buoyancy bubble and a free surface. *Theoretical and Computational Fluid Dynamics*, 8(1):73–88.

Wolfrum, B., Kurz, T., Mettin, R., and Lauterborn, W. (2003). Shock wave induced interaction of microbubbles and boundaries. *Physics of Fluids*, 15(10):2916–2922.

Wu, J. and Nyborg, W. L. (2008). Ultrasound, cavitation bubbles and their interaction with cells. *Advanced drug delivery reviews*, 60(10):1103–1116.

Xi, X. and Zhong, P. (2000). Improvement of stone fragmentation during shock-wave lithotripsy using a combined EH/PEAA shock-wave generator in-vitro experiments. *Ultrasound in Medicine and Biology*, 26(3):457–467.

Xu, J., Bigelow, T. A., Halverson, L. J., Middendorf, J. M., and Rusk, B. (2012). Minimization of treatment time for in vitro 1.1 MHz destruction of Pseudomonas aeruginosa biofilms by high-intensity focused ultrasound. *Ultrasonics*, 52(5):668–675.

Xu, W.-L., Bai, L.-X., and Zhang, F.-X. (2010). Interaction of a cavitation bubble and an air bubble with a rigid boundary. *Journal of Hydrodynamics, Ser. B*, 22:503–512.

Yang, Y. X., Wang, Q. X., and Keat, T. S. (2013). Dynamic features of a laser-induced cavitation bubble near a solid boundary. *Ultrasonics Sonochemistry*, 20(4):1098–1103.

Yousef-Coronado, F., Soriano, M. I., Yang, L., Molin, S., and Espinosa-Urgel, M. (2011). Selection of hyperadherent mutants in Pseudomonas putida biofilms. *Microbiology*, 157(8):2257–2265.

Yu, H., Chen, S., and Cao, P. (2012). Synergistic bactericidal effects and mechanisms of low intensity ultrasound and antibiotics against bacteria: A review. *Ultrasonics Sonochemistry*, 19(3):377–382.

Yuan, F., Sankin, G., and Zhong, P. (2011). Dynamics of tandem bubble interaction in a microfluidic channel. *The Journal of the Acoustical Society of America*, 130(5):3339–3346.

Zhang, S., Duncan, J. H., and Chahine, G. L. (1993). The final stage of the collapse of a cavitation bubble near a rigid wall. *Journal of Fluid Mechanics*, 257:147–181.

Zhang, Y. L., Yeo, K. S., Khoo, B. C., and Wang, C. (2001). 3D jet impact and toroidal bubbles. *Journal of Computational Physics*, 166:336–360.

Zhang, Z.-Y. and Zhang, H.-S. (2005). Surface tension effects on the behavior of two cavities near a rigid wall. *Physical Review E*, 71:066302.

Zhong, P., Lin, H., Xi, X., Zhu, S., and Bhogte, E. S. (1999). Shock wave-inertial microbubble interaction: Methodology, physical characterization, and bioeffect study. *The Journal of the Acoustical Society of America*, 105:1997–2009.

Zhu, C., He, N., Cheng, T., Tan, H., Guo, Y., Chen, D., Cheng, M., Yang, Z., and Zhang, X. (2013). Ultrasound-targeted microbubble destruction enhances human β-defensin 3 activity against antibiotic-resistant Staphylococcus biofilms. *Inflammation*, 36(5):983–996.

Zoueshtiagh, F., Caps, H., Legendre, M., Vandewalle, N., Petitjeans, P., and Kurowski, P. (2006). Air bubbles under vertical vibrations. *The European Physical Journal E*, 20:317–325.